Magnetic Nanocomposite Cilia Sensors

Dissertation by

Ahmed Haidar Alfadhel

In Partial Fulfillment of the Requirements for the Degree of
Doctor of Philosophy
In
Electrical Engineering

King Abdullah University of Science and Technology
Thuwal, Kingdom of Saudi Arabia

EXAMINATION COMMITTEE APPROVALS FORM

The dissertation of Ahmed Alfadhel is approved by the examination committee.

Dr. Ali Javey

Committee Member Signature Date

Dr. Hakan Bagci

Committee Member Signature Date

Dr. Enzo Fabrizio

Committee Member Signature Date

Dr. Jürgen Kosel

Committee Chair Signature Date

ABSTRACT

Magnetic Nanocomposite Cilia Sensors

Ahmed Alfadhel

Recent progress in the development of artificial skin concepts is a result of the increased demand for providing environment perception such as touch and flow sensing to robots, prosthetics and surgical tools. Tactile sensors are the essential components of artificial skins and attracted considerable attention that led to the development of different technologies for mimicking the complex sense of touch in humans.

This dissertation work is devoted to the development of a bioinspired tactile sensing technology that imitates the extremely sensitive hair-like cilia receptors found in nature. The artificial cilia are fabricated from permanent magnetic, biocompatible and highly elastic nanocomposite material, and integrated on a giant magneto-impedance magnetic sensor to measure the stray field. A force that bends the cilia changes the stray field and is therefore detected with the magnetic sensor, providing high performance in terms of sensitivity, power consumption and versatility.

The nanocomposite is made of Fe nanowires (NWs) incorporated into polydimethylsiloxane (PDMS). Fe NWs have a high remanent magnetization, due the shape anisotropy; thus, they are acting as permanent nano-magnets. This allows remote device operation and avoids the need for a magnetic field to magnetize the NWs, benefiting miniaturization and the possible range of applications. The magnetic properties of the nanocomposite can be easily tuned by modifying the NWs concentration or by aligning the NWs to define a magnetic anisotropy. Tactile sensors are realized on flexible and rigid substrates that can detect flow, vertical and shear forces statically and dynamically, with a high resolution and wide operating range. The advantage to operate the sensors in liquids and air has been utilized to measure flows in different fluids in a microfluidic channel. Various dynamic studies were conducted with the tactile sensor demonstrating the detection of moving objects or the texture of objects. Overall, the results confirm the possibility to easily control the sensors' performance with the cilia arrangement and dimensions. The cost effective mold-based microfabrication process and magnetic operation enable a high degree of integration, which together with the extremely low power consumption make the artificial cilia sensor reported in this dissertation an attractive solution for many applications.

ACKNOWLEDGEMENTS

First and foremost, I would like to thank my advisor Prof. Jürgen Kosel for his continued support, confidence in me, and providing a perfect balance of freedom and guidance during the course of my study. My sincere appreciation goes also to my thesis committee members: Prof. Hakan Bagci, Prof. Enzo Fabrizio, and Prof. Ali Javey for reviewing my thesis and giving me valuable suggestions. I would like to pass on my special thanks to Prof. Boon Ooi, and Prof. Khaled Nabil Salama for allowing me to use their lab facilities.

My appreciation also goes to my friends, colleagues, the department faculty and staff for making my time at KAUST a great experience. From Core Lab, I offer my gratitude to the core lab staff for their years of support and hard work, especially, Ahad Syed, Marwane Delilo, Basil Chew, and Abdulrazzaq Alharbi. I want to thank the lab manager Ulrich Buttner, and colleagues Mohammed Al-Nassar, Bodong Li, Amir Zaher, Chinthaka Gooneratne, Yurii Ivanov, Enrique Vilanova, Hanan Mohammed, Mincho Kavaldzhiev, Maria Contreras, and Mohammed Asadullah Khan for their continuous help and for providing a friendly and energetic atmosphere.

Lastly, I would like to take this opportunity to express my sincerest love to my parents, my wife, my daughter, extended family and close friends for their love and endless support throughout my undergraduate and postgraduate studies.

TABLE OF CONTENTS

LIST OF ABBREVIATIONS

AAO	Anodic Aluminum Oxide
AC	Alternating Current
AFM	Atomic Force Microscopy
AMR	Anisotropic Magnetoresistance BIS
DC	Direct Current
DRIE	Deep reactive ion etching
FEM	Finite Element Method
FMR	Ferromagnetic Resonance
GMI	Giant magneto-impedance
GMR	Giant Magnetoresistance
MFM	Magnetic Force Microscopy
NWs	Nanowires
PDMS	Polydimethylsiloxane
PMMA	Poly-methyl methacrylate
SAED	Selected area diffraction
SEM	Scanning Electron Microscopy
SQUID	Superconducting Quantum Interference Device
TEM	Transmission Electron Microscopy
VSM	Vibrating sample magnetometer
XRD	X-ray diffraction

LIST OF SYMBOLS

Symbol	Definition
$A(\delta)$	*Effective area upon cilia deflection*
B	*Magnetic Flux*
C_D	*Drag coefficient*
d	*Diameter*
D	*Diameter*
D_h	*Hydraulic diameter*
d_{top}	*Top diameter*
d_{bottom}	*Bottom diameter*
d_{avg}	*Average diameter*
E_{tot}	*Total energy in a magnetic material*
E_{ex}	*Exchange energy*
E_H	*Zeeman energy*
E_{ea}	*Magnetoelastic energy*
E_d	*Demagnetization energy*
E	*Young's modulus*
E_e	*Electric field*
F	*Force*
F_c	*Faraday constant*
H	*Magnetic Field*
Hc	*Coercive Field*

H_s	*Saturation Field*
H_{sw}	*Switching field*
H_D	*Demagnetizing field inside a material*
H_{stray}	*Stray field*
I	*Moment of inertia*
l	*Length*
M	*Magnetization*
M_r	*Remanence Magnetization*
M_s	*Saturation Magnetization*
m	*Mass*
MW	*Molecular weight of the material*
n	*Number of electrons transferred per ion*
N_d	*Demagnetizing factor*
P	*Pressure*
P_L	*Point load*
p	*Power*
Q	*Electric charge*
q	*Uniformly distributed load*
R	*Resolution*
Re	*Reynolds number*
s	*Speed*
S	*Sensitivity of the flow sensor*
S_{GMI}	*Sensitivity of the GMI sensor*

V	*Velocity*
Z_0	*Characteristics impedance*
Z_L	*50 Ω termination load*
Z_f	*Impedance fluctuation (noise)*
μ_0	*Vacuum magnetic permeability*
μ_r	*Relative permeability*
μ	*Magnetic permeability*
μ_d	*Fluid dynamic viscosity*
χ	*Susceptibility*
$v\%$	*Volume ratio*
v_{NWs}	*Volume of nanowires*
v_{PDMS}	*Volume of PDMS*
v_{avg}	*Average flow velocity*
δ	*Beam displacement*
δ_m	*Skin depth*
ρ_r	*Resistivity*
ρ	*Fluid density*
ω	*Angular frequency*
Γ_{MP}	*Reflection coefficients at the measurement plane*
Γ_{SP}	*Reflection coefficients at the sample plane*

LIST OF ILLUSTRATIONS

LIST OF TABLES

1 INTRODUCTION, MOTIVATION AND CONTRIBUTION

1.1 Motivation and Objectives

Evolutions in areas like health monitoring, robotics or prosthetics are demanding an increased perception of the environment including touch, flow, and vibration. Noticeable progress in the field of artificial skins led to the development of different technologies that can mimic the complex sense of touch in humans for better interaction with the surrounding environment. These skins are also important for applications like health monitoring systems and smart surgical tools. Tactile sensors are the essential components in the artificial skin development that attracted considerable attention and resulted in introducing different sensing mechanisms. However, many technical challenges remain in current technologies, including the limited performance and the high power consumption, in addition to the interference with environmental noise.

From another perspective, nature has been a source of inspiration for engineers and a myriad of structures and materials have been mimicked to achieve outstanding sensing performance with extreme reliability and robustness. One structure used more commonly in nature is the “cilia”. Cilia are micro-scale, hair-like structures that exist in nature in many forms and assist in performing a variety of functions as discussed in section 2.1. Hair structures offer many attractive features making them desirable for many applications. For example, the large surface area to volume ratio and the high aspect ratio provide good interaction with the external environment providing efficient sensing. Hair-like structures have been researched extensively to achieve a variety of functions and outstanding applications have been introduced in literature (section 2.3).

The ongoing search for multifunctional wearable devices and sensors with features like flexibility, biocompatibility, and low cost has directed researchers to the field of polymer-based sensing materials. Polymers can provide these features in addition to the advantage of easy processing and patterning. Polymer nanocomposites combine the advantages of polymers such as flexibility, durability, efficient processing, chemical resistance, and biocompatibility, with the different chemical or physical properties of the additives resulting in materials with distinct features and improved functionality compared to the original constituents. Devices and sensors based on polymers with magnetic material additives have been introduced that offered the ability of contactless operation, remote control over large distances and large magnetization under the influence of an external magnetic field as discussed in section 2.1. Recently developed magnetic polymer nanocomposites have great advantages such as the elasticity of the polymers and the magnetic properties of the additives (typically superparamagnetic particles), however, they suffer from the absence of magnetization at remanence unless an external magnetic field is applied which is not feasible for portable, fully-integrated and low-cost sensors. The proposed permanent magnetic nanocomposite offers unique properties that allow the realization of sensors with outstanding performance (section 3.2). Moreover, the developed nanocomposite offers the ability to select the polymeric material and the permanent magnetic filler in addition to the ratio between them which offer design flexibility and hence achieving technological requirements for specific applications. Unlike bulky permanent magnets, polymer-based magnetic nanocomposites provide the advantages of easy fabrication, light weight, flexibility, versatile, low cost, and the typically low-temperature processing.

The main objectives of this dissertation is to:

1. Develop a novel permanent magnetic nanocomposite material made from uniquely engineered Fe NWs incorporated into highly elastic PDMS,
2. Investigate fabrication techniques to realize micro-scale artificial cilia from the nanocomposite,
3. Develop a one of a kind bioinspired, biocompatible, corrosion resistant and power efficient magnetic sensing concept by integrating artificial nanocomposite cilia on a magnetic sensing element.
4. Investigate several potential applications for the developed artificial cilia sensor, mainly, for artificial skin and tactile sensing.

1.2 Thesis Outline and Contributions

The dissertation is structured to follow a progressive sequential study from the fabrication and characterization of the core material (Fe NWs), to the development and testing of the bioinspired nanocomposite tactile sensors. This dissertation is organized in five chapters as follows:

Chapter 1 provides an introduction, motivation and contribution to the dissertation work. An outline is provided and the collaborators are acknowledged.

Chapter 2 covers the background of the work in this dissertation. The chapter begins with discussing the physics of nanocomposites, magnetism, and permanent magnetic materials. Introduction to natural cilia and their outstanding sensing capabilities are then discussed with a focus on tactile sensing applications. A review follows on prior works of artificial cilia sensors and devices, and the different technologies and sensing mechanisms utilized to create these sensors and devices are discussed. This is followed by a review of currently available tactile sensing solutions and the different technologies behind them. Previous work on the utilization of artificial cilia to develop tactile sensors is discussed.

Chapter 3 starts with describing the concept of the nanocomposite cilia sensors. The chapter then describes the methods and experimental techniques used in the fabrication and processing of the artificial cilia sensors. That includes the techniques used to engineer the high aspect ratio Fe NWs to act as nanoscale permanent magnets which were electrodeposited inside nanoporous alumina membranes, the synthesis of the permanent magnetic and highly elastic nanocomposite, and the fabrication of the master molds used to create the artificial nanocomposite cilia. The structural and magnetic properties of the nanocomposite cilia are studied thoroughly and the possible degradation in the properties is discussed. Finally, the design, fabrication and characterization of a thin film giant magneto-impedance (GMI) magnetic field sensor are described. The feasibility of the GMI sensor as a highly sensitive and power efficient solution is discussed.

Chapter 4 shows two applications of the developed magnetic cilia sensing concept. The fabrication and testing of cilia sensors with different designs and dimensions are discussed for the different applications. The sensors results are discussed and the suitability of the cilia sensors for artificial/electronic skin applications is shown.

Chapter 5 provides a summary of all results and conclusions of this dissertation. Moreover, remaining challenges and prospects about future work are discussed.

As this dissertation is focused on the fabrication and characterization of a novel bioinspired tactile sensor that utilizes a magnetic nanocomposite and thin film magnetic field sensor, the contributions of this work are broad from the NWs engineering level to the instrumentation used to characterize the final sensor prototype. To the best of my knowledge, the research work has made the following contributions:

1. Introduced a novel and bioinspired magnetic sensing concept for pressure and tactile sensing.
2. Utilization of the permanent magnetic behavior of uniquely engineered single domain polycrystalline Fe NWs.
3. Development of Fe NWs-based nanocomposite that features:
    a. Pronounced permanent magnetic properties with tunable magnetic anisotropy direction by aligning the NWs in the nanocomposite.
    b. High elasticity with trivial degradation of the polymer elastic properties.
    c. Biocompatibility.
    d. Good corrosion resistance.
4. Development of an easy and cost effective mold fabrication using laser ablation technique to allow the fabrication of polymeric microstructures through casting.
5. Optimization of GMI magnetic sensors: a unique magnetic sensing technology that offers high sensitivity, low power consumption and easy fabrication process.

6. Utilized the GMI sensor and the permanent magnetic and highly elastic nanocomposite for the development of artificial cilia sensors that can detect shear and vertical forces for tactile sensing and artificial skin applications. The realized sensors feature:
    a. High force sensing performance with tunable sensitivity, resolution, and operating range through the modification of the artificial cilia dimensions.
    b. Extremely low power consumption.
    c. Easy and cost effective fabrication process using rigid or flexible substrates.

My Ph.D. research resulted in five papers, four conference proceedings, 12 conference presentations and posters, and one patent. The publications immediately related to this dissertation are given in the following, and permissions to re-use the materials were granted:

1. A. Alfadhel, B. Li, A. Zaher, O. Yassine, and J. Kosel, "Magnetic nanocomposite for biomimetic flow sensing," *Lab Chip*, vol. 14, pp. 4362-4369, 2014. - *Reproduced by permission of The Royal Society of Chemistry (RSC)*
2. A. Alfadhel, and J. Kosel, "Magnetic Micropillar Sensors for Force Sensing," *In Proceedings of Sensors Applications Symposium (SAS),* pp. 1 - 4, 2015. *Reproduced by permission of IEEE.*
3. A. Alfadhel, and J. Kosel, "Magnetic Nanocomposite Cilia Tactile Sensor," *Advanced Materials*, vol. 27, pp. 7888–7892, 2015. - *Reproduced by permission of John Wiley and Sons publishing group, license number: 3860690251341.*
4. Y. P. Ivanov, A. Alfadhel, M. Alnassar, J. Perez, M. Vázquez, A. Chuvilin*, et al.*, "Tunable Magnetic Nanowires for Biomedical and Harsh Environment Applications," *Scientific Reports,* vol. 6, p. 24189, 2016.

5. A. Alfadhel, M. A. Khan, S. Cardoso, D. Leitao, and J. Kosel, "A Magnetoresistive Tactile Sensor for Harsh Environment Applications," *Sensors,* vol. 16, Issue 650, pp. 1-13, 2016.

1.3 Statement of Collaboration

Because of the highly interdisciplinary nature of this dissertation, some of the work was conducted with the help of colleagues or core lab staff. Jose Efrain Perez performed the biocompatibility study of Fe nanowires. High-resolution transmission electron microscope images of the NWs were taken by Dr. Yurii Ivanov from the Sensing, Magnetism and Microsystems Group. Dr. Rachid Sougrat from the Advance Nanofabrication, Imaging, and Characterization Core Lab prepared the samples (dehydration, staining and slicing), and conducted the transmission electron microscope imaging of the nanocomposite material. Magnetic Force Microscopy images of Fe NWs were taken by Dr. Yurii Ivanov. Magnetic sensor design and optimization was a continuation and progression of the work of Dr. Bodong Li. All the other experimental procedures involving the fabrication of Fe NWs and their characterization were done by Ahmed Alfadhel.

2 BACKGROUND

2.1 Introduction to Magnetism & Magnetic Nanocomposites

Magnetism is a unique property of materials that respond at an atomic or subatomic level to an applied magnetic field. Materials behave differently when applying a magnetic field due to many factors such as the atomic structure of the material and the net magnetic field associated with the atoms. Magnetic induction B quantifies how the magnetic field changes from one material to another or, in other words, what is the total magnetic field inside a given material. B also changes depending on the medium it passes through. According to Lorentz force law, the total force F on a particle of electric charge Q with instantaneous velocity v is affected by an electric field E_e and a magnetic flux density B generated by an electric current:

$$F = Q\left[E_e + \left(v \times B\right)\right]. \tag{2-1}$$

The magnetic field H describes the magnetic field intensity, which is proportional to B in vacuum. Inside a material with internal magnetization M (a vector that quantifies the density of magnetic dipole moments in a material), B, H, and M are related as:

$$B = \mu_0\left(H + M\right), \tag{2-2}$$

where μ_0 is the vacuum magnetic permeability. Hence, the B field inside a material is a result of the magnetization of the material M and the external magnetic field H. Magnetic flux density can also be defined using the relative permeability of the material μ_r which is a measure of the ability to form a magnetic field inside the material in the presence of an external magnetic field:

$$B = \mu_r \mu_0 \cdot H\ . \tag{2-3}$$

The magnetization M induced in a material is directly proportional to the magnetic field H and the magnetic susceptibility χ, a dimensionless material parameter that specifies how a material responds to an applied field as:

$$M = \chi H \, . \qquad \text{2-4}$$

The units (SI - CGS) of the relevant magnetic quantities are listed in Table 2-1.

Magnetic Quantity	**SI Unit**	**CGS Unit**
B	Tesla (T)	Gauss (G)
H	Ampere/meter (A/m)	Oersted (Oe)
M	Ampere/meter (A/m)	(emu/cm^3) or (emu/g)

Table 2-1: The units of the relevant magnetic quantities.

The exchange coupling between magnetic moments is a consequence of Pauli Exclusion Principle such that two electrons are allowed to share an orbital if they only have antiparallel spins. Different types of magnetic materials exist depending on the nature of magnetic moments interaction. Ferromagnetism is the relevant phenomena in this dissertation, and it happens when there is a strong exchange coupling between magnetic moments that makes them align with each other in a microscopic system. Macroscopically, domains are created in ferromagnets to minimize the energy in which the moments align with each other in each domain. In small ferromagnetic materials, it can be energetically unfavorable to form domains and a single domain material is obtained. Ferromagnetic materials have a magnetic moment even in the absence of a magnetic field, due to a nonzero spontaneous magnetization. Superparamagnetism is observed in sufficiently small single domain ferromagnetic particles where an external magnetic field is needed to magnetize them. When there is no magnetic field applied, the magnetization of the material appears to be zero on average.

The magnetization behavior of a magnetic material under the influence of an external magnetic field can be studied by obtaining the hysteresis loops (discussed in detail in section 3.6). Hysteresis loops allow the investigation of different magnetic properties such as the type of the material (ferromagnetic, superparamagnetic, ... , etc.), permanent magnetism, magnetocrystalline, or shape anisotropy [1]. In a typical hysteresis loop (Figure 2-1), the x-axis corresponds to the applied magnetic field H and the y-axis corresponds to the material magnetization M. The magnetization in the y-axis can be represented as M/Ms: the ratio between the magnetization value M and the saturation magnetization Ms. For a material to reach magnetic saturation Ms, a saturation field Hs must be applied in order to overcome the anisotropy energy (discussed in section 3.2.2). Ferromagnetic materials can hold a magnetization moment in the absence of external magnetic field which is called remanence magnetization Mr. The coercive field Hc is the magnetic field value required to demagnetize the material and bring M to zero. Permanent magnetism refers to ferromagnetic materials that exhibit high saturation magnetization Ms, high remanence magnetization Mr (ideally $Mr/Ms = 1$), and hold high coercivity field Hc making them hard to demagnetize. Figure 2-1 shows a comparison between a typical hysteresis loop of a ferromagnetic material with permanent magnetic behavior ($Mr/Ms \approx 1$ and high Hc), and a hysteresis loop of superparamagnetic nanoparticles ($Mr/Ms \approx 0$ and very small coercivity Hc).

Magnetic anisotropy is responsible for the hysteresis behavior. The direction that requires less energy to magnetize a sample is called the easy axis, and it depends on the material, strain, the crystalline structure and, most importantly, the geometry. The energy associated with the magnetic anisotropy is called the magnetic anisotropy energy. This research work is focused on the utilization of ferromagnetic NWs that act as elongated single domain particles and have very high shape anisotropy. This led to a material that has pronounced hysteresis and can be engineered to have significant permanent magnetic properties as discussed in details in section 3.2.2.

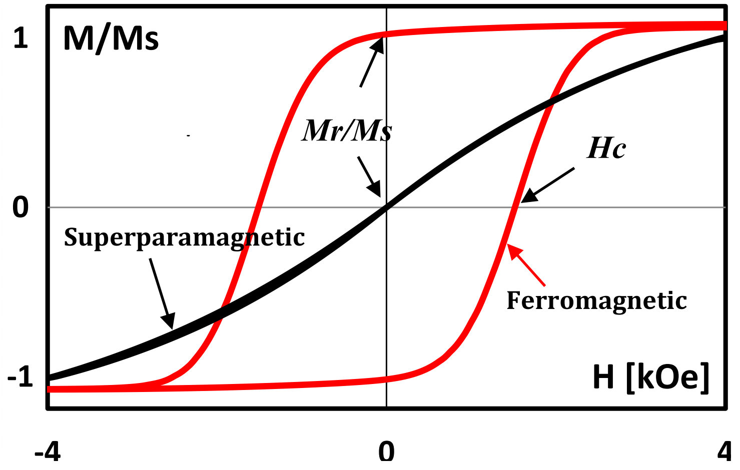

Figure 2-1: Hysteresis loops of a ferromagnetic material compared to superparamagnetic particles.

Utilizing ferromagnetic materials (permanent magnetic materials in particular) in sensors and microsystems can provide a wide range of advantages such as low power consumption, remote and contactless operation. However, the rigidity, bulkiness and machining complexity of these magnetic materials prevent the realization of microstructures, responsive sensors or elastic actuators. Magnetic and highly elastic nanocomposite materials have great potential to overcome these drawbacks.

Polymer nanocomposites have been widely investigated for their potential applications in sensors and microsystems. They have attracted considerable attention as they combine the advantages of polymers such as flexibility, durability, efficient processing, chemical resistance and biocompatibility, with the different chemical or physical properties of the additives. This mixture results in materials with distinct features and improved functionality compared to the original constituents. It was realized as early as 1856 that additives to polymers change the characteristics of the polymers [2]. In recent years, polymer nanocomposites were developed for the use in sensing applications to achieve tailored material properties [3]. Microsystems based on magnetic polymers have been introduced that offered the ability of contactless operation, remote control over large distances and large magnetization under the influence of an external magnetic field [4-9]. The theoretical prediction has shown a possibility of fabricating organic polymers that have magnetic characteristics [10]. However, most organic compounds have shown weak opposing magnetic behavior [11], making these polymers not ideal for microsystems that depend on magnetic forces or utilize magnetic actuation.

Magnetic nanocomposites have been introduced for utilization in microsystem applications using different materials and fabrication methodologies. The incorporation of magnetic materials such as Ni, Fe or Fe_3O_4 into polymers results in forming nanocomposites that benefit from the magnetic properties of the additives (typically particles) and the elasticity of the polymers. Magnetic nanocomposites have been realized for different applications especially for microfluidics such as micro-pumps, micro-valves, and cell sorting for contamination free and contactless operation [4-7]. Superparamagnetic particles have the advantage of easy dispersion in the nanocomposites due to the absence of magnetization at remanence unless an external magnetic field is applied, and they have been utilized for numerous applications [12-19]. However, applying a strong magnetic field to benefit from the high magnetic moment is not feasible for portable, fully-integrated and low-cost sensors.

Ferromagnetic materials have attracted considerable attention for many applications due to many unique properties including their remanent magnetization which determines the amplitude of the permanent magnetization of a material, and the coercive field, which is a measure of the material's resistance to demagnetization. Different techniques can be used to integrate ferromagnetic materials into sensing elements such as thin film sputtering or electroplating, and incorporating ferromagnetic particles in polymer nanocomposites. Ferromagnetic thin films have disadvantages in sensing applications such as rigidity and restrictions in controlling the magnetic anisotropy. Ferromagnetic powders consist of microscale particles with non-uniform dimensions, and they are typically prepared from commercially available permanent magnets. These particles do not have high remanence magnetization compared to the original permanent magnet due to the high demagnetizing field in different directions. The remanence magnetization of spherical ferromagnetic particles reduces as the diameter of the particles decrease [20, 21]. On the other hand, incorporating large spherical particles in the polymer can affect the mechanical properties of the polymeric nanocomposite.

In this dissertation, a novel permanent magnetic nanocomposite is introduced that utilize ferromagnetic nanowires (NWs) and benefits from the well-defined shape anisotropy with relatively high remanent magnetization, eliminating the need to apply an external magnetic field to magnetize the NWs. Incorporating NWs in polymers results in achieving a permanent magnetic nanocomposite with distinct features and reinforced mechanical behavior [22]. Also, aligning the NWs in the nanocomposite during the fabrication process defines the anisotropy in the nanocomposite and determines the direction of the permanent magnetism in the fabricated structures, as discussed in section 3.6. Moreover, the high coercive field of the ferromagnetic NWs enhances the permanent magnetic behavior making them hard to demagnetize.

2.2 Introduction to Natural Cilia

For many years, nature has been a source of inspiration for engineers and a myriad of structures and materials have been mimicked to achieve outstanding sensing performance with extreme reliability and robustness. One structure used more commonly in nature are "cilia" which have been studied since the 19th century. The earliest investigation was done by Valentin and Purkinje and reviewed by Teich *et al.* [23]. Cilia are micro-scale, hair-like receptors that exist in nature in many forms. Two types of cilia can be found in nature: motile and non-motile.

Motile cilia are typically distributed on the surface of the cell with large numbers and move in coordinated wavy motion [24]. An example in human is the cilia projecting from respiratory epithelium in the lungs that sweep mucus and dirt out of the lungs (Figure 2-2) [25].

Non-motile cilia are found in almost every cell in the body. These cilia were first discovered in 1898, but only around the 1990s, scientists had sufficient understanding of the cilia's important role in nature. The findings show the cilia capabilities for sensing, signal transduction as well as other functions like cell growth [26]. In the sensory organs, for example, we can find specialized cilia human eyes connecting the outer part of the rod photoreceptor cell to the cell body [27]. Also, non-motile cilia can be found in other creatures as the sensing receptors on insect legs (Figure 2-3) to detect touch and vibration [28], mechanosensorial cerci of crickets [29, 30], hair receptors in fish [31], the cilia in the gut of marine worms [32], or the cochlea in the inner ear [33]. Taking fish as an example, the hair cells assist in performing a variety of functions such as preying or avoiding danger. When the cilia are exposed to a change in the fluid flow, they bend and transmit a signal to the organism. This signal is then translated into a specific function.

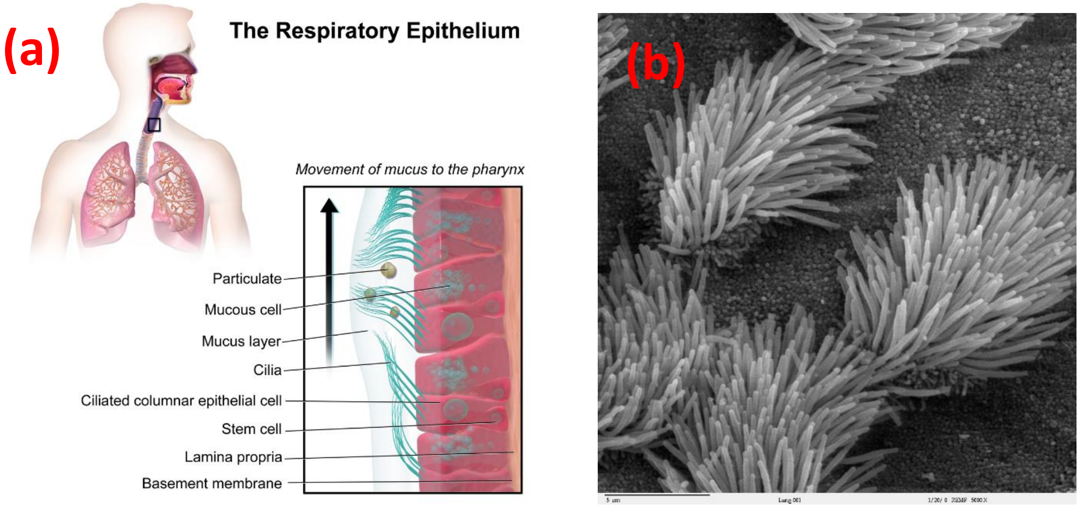

Figure 2-2: a) Illustration of the function, and (b) SEM micrograph of the cilia projecting from respiratory epithelium in the lungs.

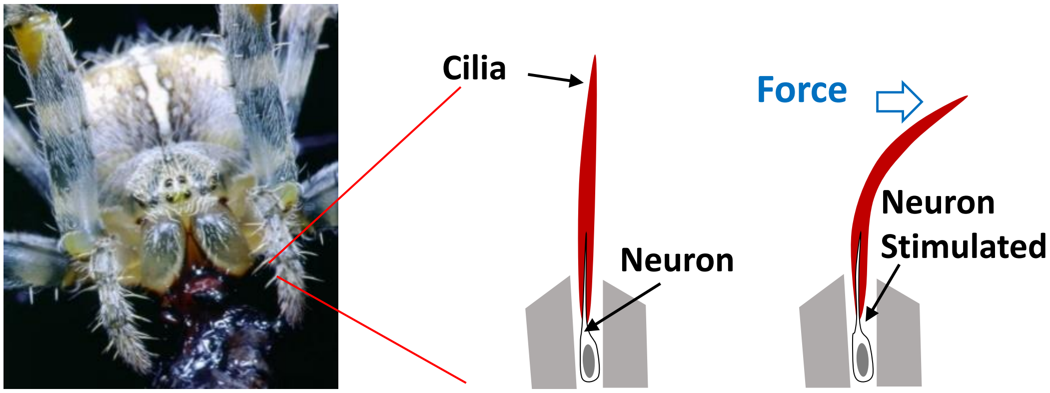

Figure 2-3: Illustration of the mechanosensorial non-motile cilia found in spiders.

2.3 Artificial Cilia Devices and Sensors

Artificial cilia devices have been developed to mimic the extremely sensitive mechanosensorial cilia receptors found in nature. They enable transferring of various mechanical forces and provide exquisite sensing performance, mainly due to the high aspect ratio and high surface area to volume ratio, which ensures strong interaction with the environment. Hair-like structures have been researched extensively to achieve a variety of functions and many attractive features including: cell mechanics study [34, 35], liquid motion and microfluidic propulsion [8, 36], flow sensing [37], pressure and gas sensing [38]. In this section, few unique examples of artificial cilia devices and sensors are visited and discussed.

Polymeric artificial cilia on a magnetic sensor have been presented previously [39]. Polypyrole cilia have been fabricated on top of GMR sensors and were tagged with a 300 nm $Co_{50}Fe_{50}$ by sputter deposition (Figure 2-4). The sensor was tested by agitating at different frequencies and measuring the response due to cilia bending. The proposed design suffers from several issues such as the easy corrosion of the magnetic tagging, the toxicity of Co, the low stray field expected from the magnetic tagging, and the non-uniform tagging that lead to having cilia with different magnetic and mechanical properties.

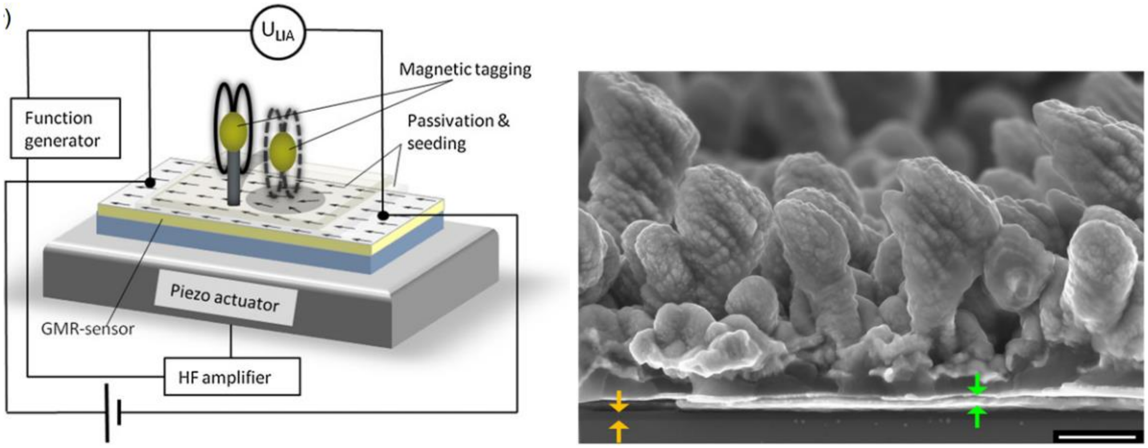

Figure 2-4: (a) Sensing concept and testing setup. (b) Cross-sectional image of the cilia array coated with a 300 nm CoFe tagging. The scale bar corresponds to 500 nm. (Reproduced by permission [39]).

Drotlef *et al.,* [40] reported arrays of PDMS pillars containing NdFeB particles as a bioinspired reversible adhesion surface. The magnetic pillars are designed to have an adhesive surface, and experience bending in response to an external attraction magnetic force. The change in surface topography by bending the pillars through magnetic actuation, allowed modifying the surface properties between adhesive and non-adhesive. Despite the disadvantage of requiring a strong magnetic field to actuate the surface which is not attractive for portable and power efficient systems, the concept operates in dry and wet conditions and shows the potential to develop large areas of smart surfaces with modifiable properties.

The bioinspired cilia concept has been utilized to realize an acoustic flow sensor, fabricated using micro-electro-mechanical systems (MEMS) technology [29]. The micro-sensors array shown in Figure 2-5 is fabricated using SU-8 polymer cilia up to 1 mm long mounted on suspended membranes. The acoustic flow was measured by capacitance change read-out through electrodes on the membrane and the substrate. A drawback of the reported system is the complex and costly fabrication process in addition to the fragility of the membrane.

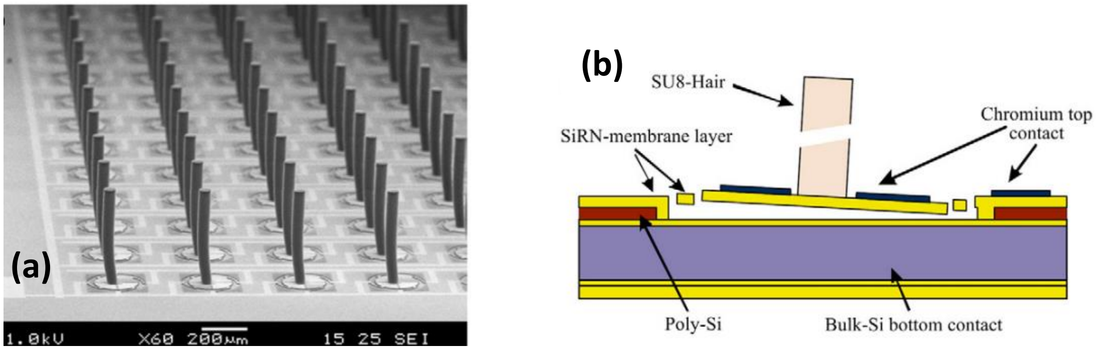

Figure 2-5: (a) Scanning electron microscopy image of array of sensory hairs. (b) SU-8 hair structure. (Adapted from reference [29]).

PDMS cilia structures (microposts) were developed by Sniadecki *et al.,* [41] to apply force to living cells. The concept utilizes the fact that cells respond to mechanical forces. The cellular response to forces applied via magnetic cilia array was studied where each cilium acts as an independent sensor to cellular traction forces (Figure 2-6). The study of the designed system about dynamic and biological forces on attached cells demonstrated the potential of cilia based systems to explore this interaction.

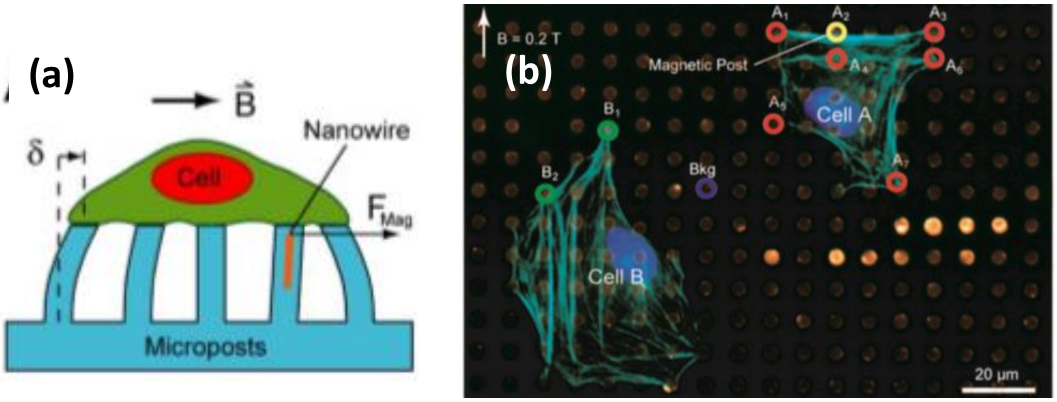

Figure 2-6: (a) External force is applied to the cell through PDMS cilia (microposts) with Co NWs. Cilia bend under the influence of an external magnetic field. (a) Immunofluorescent micrograph showing changes in traction forces in cells after force application. (Adapted from reference [41]).

2.4 Tactile Sensors and Artificial Skins

Evolutions in areas like robotics, prosthetics, and biomedical sensing are demanding the development of sensors with increased perception of the environment such as touch, vibration, and air flow [42-55]. Noticeable progress in the field of artificial skins led to the development of different technologies that can mimic the complex sense of touch in humans for better interaction with the surrounding environment. These skins are also important for applications like real-time health monitoring systems and smart surgical tools. Tactile sensors are the essential components in the artificial skin development that attracted considerable attention. Sensors with multisensory capabilities have been researched extensively and many physical principles have been exploited for the development of sensing elements such as tactile or flow sensors to achieve devices that are portable, have a high sensitivity and low power consumption. Tactile sensors with different sensing mechanisms have been introduced such as resistive, piezoelectric and capacitive sensing [42-53]. However, several major technical challenges remain in current tactile sensing research including low sensitivity and high power consumption in addition to the susceptibility to environmental noise. Magnetic sensing has the potential to lead another trend in the development of artificial skins for its outstanding advantages including the possibility of contactless and low power operation.

A tactile sensing mechanism introduced by Gong *et al.* [56] (Figure 2-7), is based on the resistivity of a gold NWs nanocomposite that has shown a high resolution of 13 Pa with a sensing range up to 50 kPa. It has the ability to detect bending, torsion and pressing with a power consumption of 30 μW. Other resistive tactile sensors developed by Zhu *et al.* were made from a microstructured graphene/PDMS nanocomposite showing an ultra-high sensitivity of 1.5 Pa with a sensing range up to 1.5 kPa [57]. The sensors can detect vertical pressure and provide a very fast dynamic response of 0.2 ms. A piezoresistive tactile sensor was proposed by Yilmazoglu *et al.* [58]. It uses carbon nanotubes, has a resolution of 32 mN and operates with power consumption of 1.9 µW. Different capacitive tactile sensors have been presented in literature such as the capacitive sensor with microstructures rubber dielectric proposed by Mannsfeld *et al.* that can detect a low pressure of 3 Pa and operates up to 7 kPa [44].

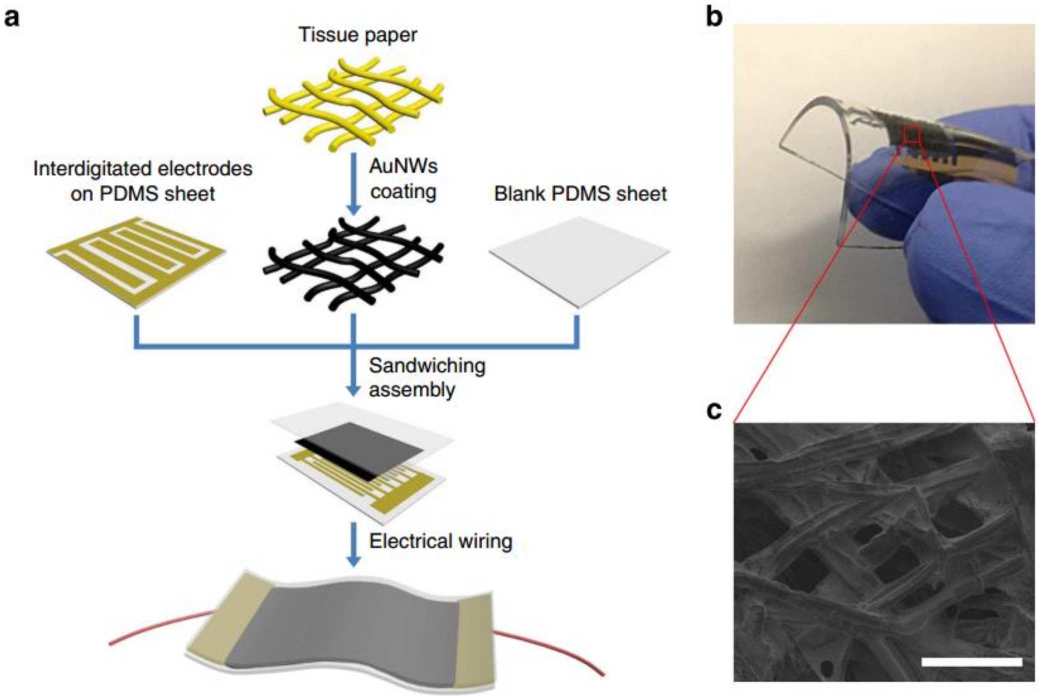

Figure 2-7: (a) Illustrations of resistive tactile sensor based on gold NWs proposed by Gong *et al*. (b) The sensor bendability of the sensor. (c) SEM image of the gold NWs morphology with coated tissue fibers showing scale bar of 100 µm. (Figure adapted from reference [56]).

Tactile sensors that utilize artificial cilia design with various sensing concepts have been previously investigated [39, 43, 53]. A highly skin-conformal strain-gauge artificial cilia sensor has been developed by Pang *et al.* that can detect pressures, shear and torsion (Figure 2-8) [43]. The sensor is based on two interlocked arrays of platinum coated polymeric artificial cilia (nanofibers) mounted on thin PDMS layers. The sensing mechanism is based on the change of the degree of interconnection and in electrical resistance upon the application of different stimuli. It has been shown that the sensor can be used to monitor heartbeats or even a bouncing water droplet on a hydrophobic surface. A cilia capacitive sensor (Figure 2-9) by Pang *et al.* has shown outstanding performance for pulse signal amplification and a high potential for wearable health monitoring systems [53].

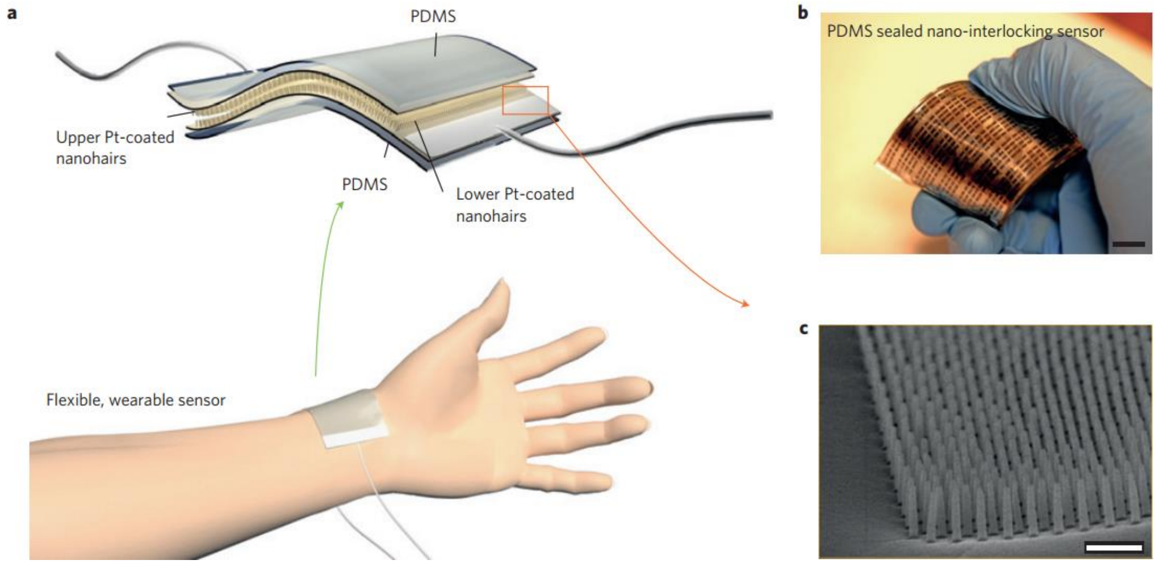

Figure 2-8: (a) Illustration of the flexible artificial cilia (nanohairs) strain-gauge tactile sensor. (b) Image showing the flexibility of the sensor (scale bar: 1 cm). (c) SEM image of an array of 100 nm in diameter cilia (scale bar: 1 µm) (Adapted from [43]).

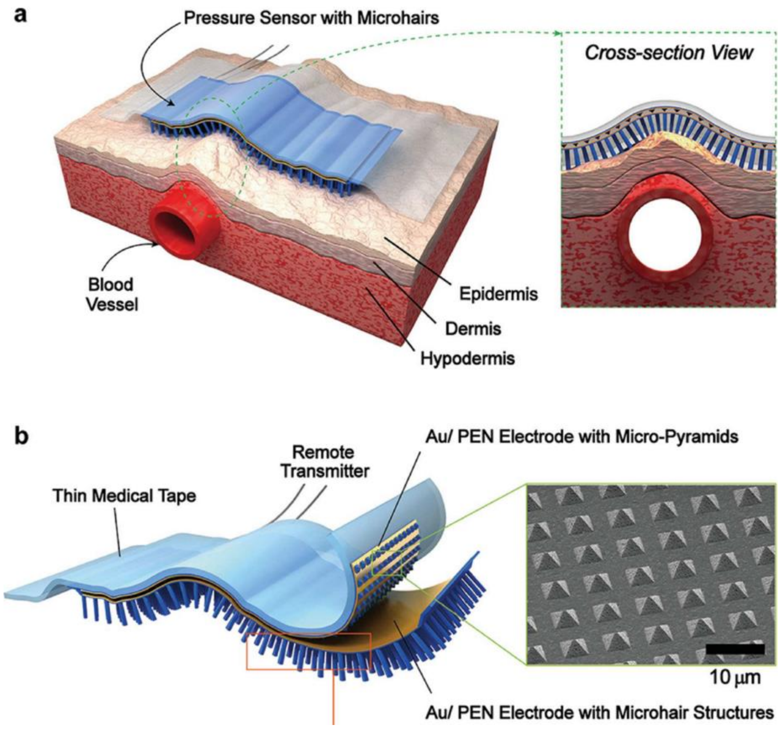

Figure 2-9: (a) Illustration of highly skin conformal pressure sensor using artificial cilia (microhair structures) mounted a human's neck. b) Illustration of the several layers of the sensor, showing an SEM image of the pyramid-shaped PDMS dielectric layer. The microhair-structured layer improves conformal contacts with skin (Adapted from [53]).

Despite this rapid development in tactile sensing technology, there are still many challenges that need to be addressed. It is especially challenging to combine a high resolution with a low power consumption while maintaining multi-functionality (sensing of flow, vibration, touch, ….). The ability to operate in different media such as water and air has not been shown at all yet, but will be required for practical reasons.

The sensing principle and metrological properties of different tactile sensors from literature are summarized in Table 2-2 and compared to the work conducted in this dissertation.

Table 2-2. Sensing principle, microfabrication process, design, applications and metrological properties of different tactile sensors

SENSING PRINCIPLE	REFERENCE	DESIGN & FABRICATION PROCESS	APPLICATION	RESOLUTION	MEAS. RANGE	POWER CONS.	FLEXIBLE	OTHER METROLOGICAL PROPERTIES
RESISTIVE & STRAIN GUAGE SENSORS	Gong, *et al.*, 2014 [56]	Resistive sensing using Gold NWs and paper fiber in PDMS with top electrodes	Pressure sensing	13 Pa	0 - 50 kPa	30 μW	YES	-Area: 5×5 mm/pixel -Sensitivity: 1.14 kPa^{-1} -Can detect bending/ torsion/ pressing -50,000 cycle stability
	Pang, *et al.*, 2012 [43]	Strain-gauge sensing using Pt-coated polymer bioinspired nanocilia sandwiched by PDMS layers	Pressure sensing	5 Pa	0 -1 kPa	--	YES	-Sensitivity: 0.004 Ω /Pa -Can detect shear/ torsion/ pressing -10,000 cycle stability
	Yilmazoglu, *et al.*, 2012 [58]	Piezoresistive sensing using Carbon nanotubes	Pressure, Tactile, and Vibration sensing	32mN	--	1.9 μW	YES	-Sensitivity: 22 Ω/mN -1 mm spatial resolution
	Zhu, *et al.*, 2014 [57]	Resistive sensing using micro-structured graphene Oxide/PDMS affixed to a flat (ITO)-(PET) film	Pressure/Tactile sensing	1.5 Pa	0 – 100 Pa	--	YES	-Sensitivity: -5.53 kPa^{-1} -5,000 cycle stability response (signal change) -External pressure deforms the pyramids resulting in an increase of contact area and a decrease in resistance.
	Liu, *et al.*, 2007 [59]	Bioinspired strain gauge flow sensors based on silicon or polymer cilia	Flow Sensing	0.5 mm/s	0 - 1 m/s (Water) 0 – 30 m/s (Air)	--	NO	-Silicon-based flow sensors showed higher sensitivity, whereas polymer-based sensors were more robust
PIEZO-ELECTRIC SENSORS	Sharma , *et al.*, 2012 [60]	PVDF-TrFE copolymer piezo-electric tactile sensor patterned using mold-transfer method	Minimally invasive surgery	25 mN	0 – 1 N	--	NO	- Sensitivity 10 $\text{mV}\cdot\text{N}^{-1}$ - Bandwidth 0–100 Hz
	Dargahi *et al.*, 2000 [61]	Tooth-like patterned PVDF film	Endoscopic grasper	--	0 – 2 N	--	NO	- 2 × 2 array - Sensitivity 100 $\text{mV}\cdot\text{N}^{-1}$

Table 2-2. *Cont.*

CAPACITIVE SENSORS	Muhammad , *et al.*, 2011 [62]	PDMS-coated capacitive sensor	Robotic finger	25 mN	0 – 1.7 N	--	NO	- 1 × 4 array -Sens.: 0.068 $\text{fF}\cdot\text{mN}^{-1}$ - Roughness encoding
	Mannsfeld, *et al.*, 2010 [44]	ITO/PET layer on PDMS pyramids, integrated on organic field-effect transistor.	Pressure/Tactile sensing	3 Pa	0 – 7 kPa	100 μW	NO	-Sensitivity: -0.55 kPa^{-1} (range 0-2 kPa) and -0.15 kPa^{-1} (range 2-7 kPa). -The size of the pressure sensitive pad is 64mm^2.
	Lipomi, *et al.*, 2011 [49]	Capacitive sensing using spray-deposited single-walled carbon nanotubes between Ecoflex.	Pressure and strain sensing	50 kPa	0 – 1 MPa (Pressure) 50% (Strain)	--	YES	-Transparent and stretchable. - Sensitivity: 0.23 MPa^{-1} and 0.004 $(\text{strain}\%)^{-1}$ - 8 × 8 array of nanotube lines.
	Krijnen, *et al.*, 2006 [29]	Bioinspired SU-8 cilia on capacitive moveable plate.	Acoustic flow sensing	0.1 m/s	0 – 1 m/s		NO	-Sensor arrays based on the mechano-hair sensors found on crickets. -Sensitivity: 10 fF/(m/s)
OPTICAL-BASED SENSORS	Cowie *et al.*, 2007 [63]	Optical tactile sensing using fiber Bragg gratings	General biomedical purposes	--	--	--	NO	-Nine sensors array -Ability to distinguish the position and shape of a contacting load.
	De Rossi *et al.*, 2011 [64]	Light intensity modulation	Biomechanical analysis	--	0 – 500 kPa	370 mW (Including electronics)	NO	- Sensitivity: -0.02 $\text{V}\cdot\text{N}^{-1}$ -64 sensing elements. - 1 cm^2 spatial resolution.
MAGNETIC SENSORS	Schroeder, *et al.*, 2011 [39]	Bioinspired polypyrrole cilia array coated with CoFe tagging on a GMR sensor	Vibration sensing	--	--	64 mW	NO	- The stray field of the actuated cilia changes the response of the GMR sensor. 190 kHz characteristic freq.
	Hein, et al., 2013 [65]	Biomimetic Co nano-cilia arrays detected using a magnetic sensor	Flow sensing	0.9 m/s	3.3 - 40 m/s (Water)	140 μW	NO	- Co cilia stray field detected using GMR sensor and tested in a microfluidic channel. -Ability to detect low frequency range of 1–5 Hz
	Alfadhel, *et al.*, 2014 [66]	Permanent magnetic and highly elastic nanocomposite cilia integrated on a magnetic sensor	Flow sensing	(Air) 0.5 mm/s (Water) 0.013 mm/s	(Air) 0-190 mm/s (Water) 0-7.8 mm/s	80 nW	YES (Rigid or flexible)	-Sensitivity up to 0.9 Ω/kPa -1 mm^2 spatial resolution -Tunable performance -Static/dynamic vertical and shear forces detection -Underwater and harsh environment operation
	Alfadhel, *et al.*, 2015 [67]		Pressure/Tactile sensing	0.88 kPa 16 Pa	0- 200 kPa 0-0.85 kPa			

3 MAGNETIC NANOCOMPOSITE CILIA SENSORS

3.1 Concept

Highly elastic and permanent magnetic nanocomposite artificial cilia are implemented on a high sensitivity thin-film magnetic field sensor. Artificial cilia are ideal for tactile sensing to mimic the extremely sensitive mechanosensorial hair-like cilia receptors found in insects for touch and vibration sensing. They enable transferring of various mechanical forces and provide exquisite sensing performance, mainly due to the high aspect ratio and high surface area to volume ratio, which ensures strong interaction with the environment. A stray field is created by the permanent magnetic Fe NWs in the nanocomposite cilia. This stray field can be detected using the integrated magnetic sensor, providing a magnetic field bias and changing its initial impedance. The operating principle of the cilia sensor is based on detecting the change of the stray field underneath the cilia when deflected by an external force such as vibration, fluid flow or hand touch (Figure 3-1). The robustness, high elasticity, and corrosion resistance of the proposed system allow the realization of different applications with great performance and sensitivity to small exerted forces. The operating range and sensitivity of the proposed system can be easily optimized by changing the cilia arrangement (e.g. single cilia or array), dimensions of the cilia, or the NWs concentration in the nanocomposite.

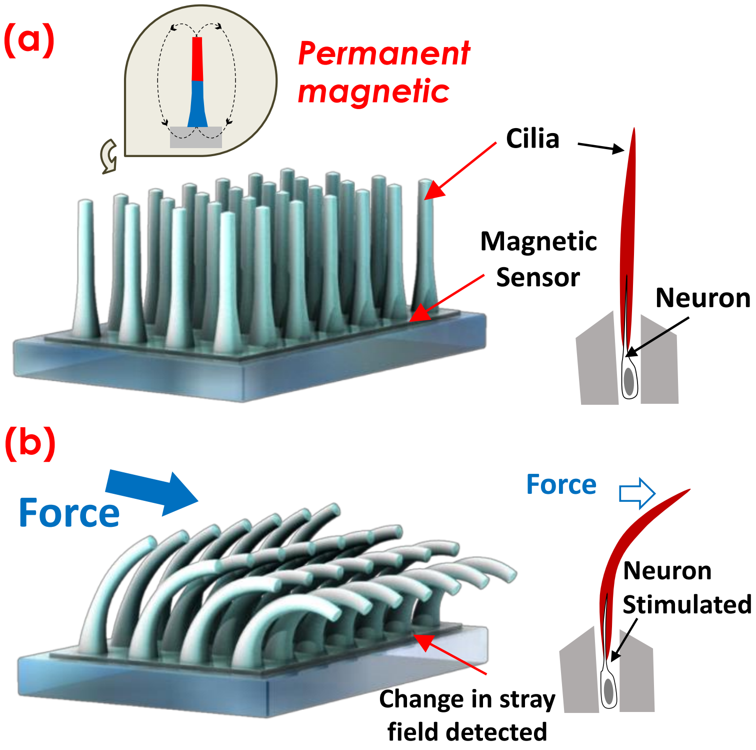

Figure 3-1: (a) Illustration of the nanocomposite cilia tactile sensor. The sensor is made of permanent magnetic nanocomposite cilia integrated on a magnetic sensor that mimics the neuron in natural cilia. (b) When the cilia get deflected by external forces such as fluid flow or hand touch, the stray field at the magnetic sensor changes, which also changes its impedance.

3.2 Permanent Magnetic Nanocomposite Design and Synthesis

3.2.1 Polymer Selection

Polydimethylsiloxane (PDMS) was selected as the polymeric material of the nanocomposite. PDMS is a commercially available silicone rubber with a wide range of applications. It is a mineral-organic polymer that contains carbon and silicon, and it is from the siloxane family that has silicon, oxygen and alkane. Apart from it applications in microsystems and microfluidics, PDMS is biocompatible and used as a food additive (E900), in shampoos, and as an anti-foaming agent in beverages or in lubricating oils.

The PDMS chemical formula is CH3[Si(CH3)2O]nSi(CH3)3, where "n" is the number of repeated monomers (Figure 3-2). Depending on the monomers chain, at low "n" values the non-cross-linked PDMS is almost liquid, while at high "n" PDMS becomes semi-solid. This viscoelasticity behavior that allows obtaining a flexible polymer is due to the siloxane bonds. Solid PDMS is prepared from a base solution and a curing agent with typically a 10:1 ratio. By changing the base solution to curing agent ratio, a significant change in the properties of the cured PDMS is expected. By increasing the amount of curing solution, the mixture becomes less viscous because it is the average of the base solution viscosity (0.0050 m^2/s) and the curing solution viscosity (0.0011 m^2/s) [68]. Moreover, increasing the amount of curing solution results in more cross-linked elastomer that is harder and less elastic [69]. PDMS can cure completely at room temperature in 24-48 hours. Heating is typically used to accelerate the cross-linking reaction and greatly reduce the curing time without affecting the quality of the resulting PDMS [70]. After cross-linking, PDMS becomes a hydrophobic elastomer.

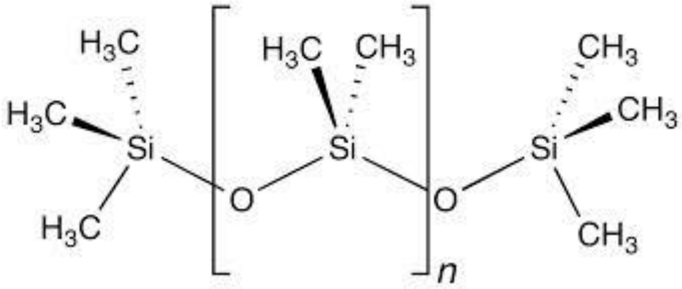

Figure 3-2: PDMS chemical composition.

PDMS has a non-toxic nature and is known as a material with a good chemical resistance that can withstand most chemicals with low chemical reactivity (except at extremes pH values). PDMS does not get deformed or affected by water, glycerol, methanol or ethanol. Hence, it is possible to use these fluids with PDMS microstructures without worrying of deformation. However, PDMS swells at different degrees when interacting with chloroform, ether, acetone or propanol.

Some physical and chemical advantages of PDMS compared to other polymers are: low glass transition temperature (≈−125 ◦C), unique flexibility where it is the most flexible polymer with a shear modulus, high dielectric strength, high ability to compress and stretch, and wide operating temperature range (from −100 ◦C and up to +100 ◦C) [71-73].

3.2.2 Permanent Magnetic Material Selection

Toward the effort of providing permanent magnetics materials for miniaturized systems, magnets made of elongated single domain particles have been introduced in the 1960s [74-76]. Ferromagnetic NWs, acting as elongated single domain particles, have been investigated recently through micro-magnetic simulations and experimental studies [77]. The permanent magnetic behavior of a ferromagnetic material can be governed by several types of anisotropy energies that can behave differently in different magnetic materials. The total energy E_{tot} in a magnetic material can be expressed as:

$$E_{tot} = E_{ex} + E_H + E_{ea} + E_{ca} + E_d, \qquad 3\text{-}1$$

where E_{ex} is the exchange energy related to the spin interaction of atoms. E_H is called Zeeman energy which is a magnetic potential energy from a magnetization induced externally. E_{ea} is the magnetoelastic energy. Magnetoelastic anisotropy occurs when there is elastic strain on the lattice structure of the material, and the easy-axis is typically the direction of magnetization that minimizes the strain energy. E_{ca} is the energy associated with the crystalline anisotropy where the material's crystal lattice structure induces energetically and magnetically preferred directions in which the energy required to magnetize the material are unequal. E_d is the magnetostatic or demagnetization energy which is related to the material's shape [78]. Shape anisotropy occurs in magnetic materials with a dimension much larger than the other dimensions (i.e. high aspect ratio NWs with easy-axis in the direction of the NWs length). This dimension inequality causes the magnetic moment to align with the direction of the large dimension, minimizes the demagnetizing field inside the material, H_D, and obtain high remanence magnetization Mr. The demagnetization field reflects the tendency to reduce the total magnetic moment and demagnetize the material, given by [78]

$$H_D = -N_d \cdot M \qquad 3\text{-}2$$

where N_d is a shape-dependent demagnetizing factor. The field outside the materials is called stray field (H_{stray}) and it is generated by the magnetization in the NWs. H_D has the same amplitude as H_{stray} but directs opposite to M [79, 80]. Ellipsoidal shape magnetic materials with uniform magnetization in the entire sample have demagnetization energy E_d of:

$$E_d = \frac{1}{2}\mu_0 N_d \cdot Ms^2 \qquad 3\text{-}3$$

The general magnetic response of a material is determined by the combination of these energy terms E_{tot} with the unit J/m^3, and typically one or few terms dominate the rest of the energy terms. In the case of high aspect ratio NWs, the magnetic properties can be exploited by discussing magnetocrystalline anisotropy and shape anisotropy, where the latter is the dominant term.

The magnetic behavior of the NWs can be approximated using the Stoner-Wohlfarth model. The Stoner-Wohlfarth model allows investigating the magnetization reversal and properties of the hysteresis loop of single domain particles. For a single isolated NW, as illustrated in Figure 3-3b, the hysteresis loop is rectangular in shape with applied field along the easy axis (length of NW). The loop has a remanence to saturation magnetization ratio Mr/Ms of one with an infinite slope at the coercive field Hc [81]. This is due to the high shape anisotropy in NWs [82]. The sharp transitions between magnetization states indicate the single domain nature of the NWs [81]. When NWs are close to each other in a configuration similar to NWs in AAO membrane or in the nanocomposite, magnetostatic interactions occur between the neighboring NWs. This interaction changes the shape of the easy access hysteresis loop to be less squared due to the demagnetization field H_d (Figure 3-3c) [83]. The magnetization of NWs switches by first nucleating a vortex domain wall at the ends of the NWs followed by domain wall motion along the NW. The switching field H_{sw} varies with the angle between the field and the NWs, with maximum H_{sw} at the hard axis (perpendicular to the NWs) [78, 81]. Applying field along the easy axis of a single NW, leads to a H_{sw} value equal to Hc [78]. In the case of NWs array, these two values are different due to the demagnetization field H_d. When the applied field is at an angle with the NWs parallel direction and close to the hard axis, the shape of the loop becomes tilted and H_{sw} become larger than Hc.

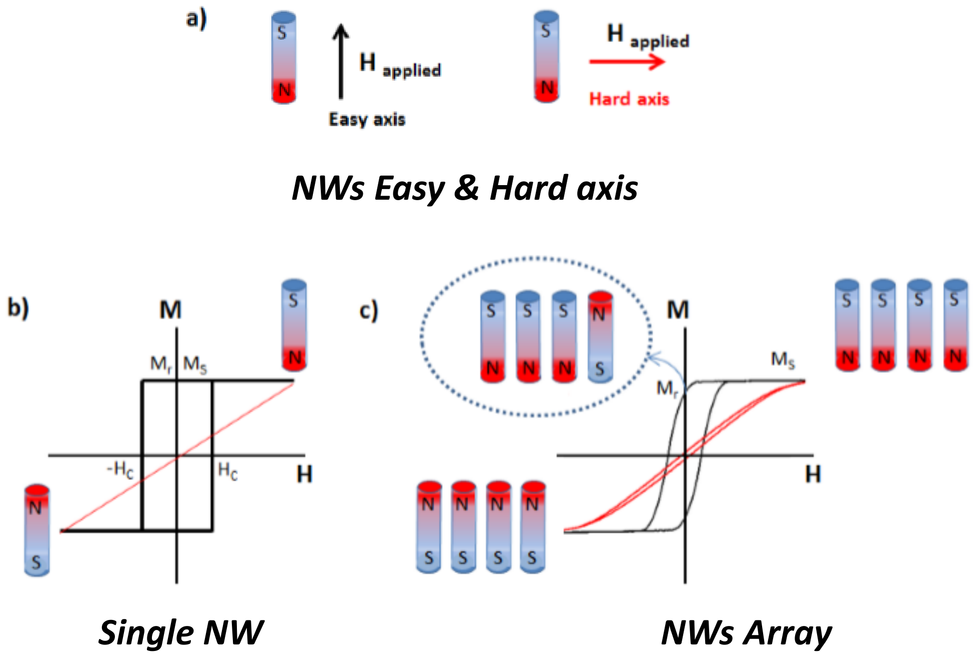

Figure 3-3: (a) Illustration of the applied magnetic field direction and the corresponding easy and hard axis of the NWs due to the shape anisotropy. b) A hysteresis loop of a single ferromagnetic NW. c) The demagnetization effect on the hysteresis loop of a ferromagnetic NWs array.

In this dissertation, Fe NWs were selected as the candidate nanocomposite filler, and engineered to act as nanoscale permanent magnets by ensuring a single magnetic domain through the reduction of the diameter and increase of the aspect ratio. Due to the high shape anisotropy, NWs favor a single domain state with magnetization *M* pointing in the direction of the NWs' length. Reducing the aspect ratio by increasing the diameter and/or reducing the length, will make the material energetically favorable to generate multiple magnetic domains [78]. The key advantages of single domain Fe NWs as permanent magnets, besides their biocompatibility [84], are the relatively high magnetization, the stray field, and the high shape anisotropy. This high shape anisotropy with up to thousands of length to diameter ratio provides a high coercivity to the material making it difficult to demagnetize. Even though NWs are not competitive with the high performances of NdFeB alloys permanent magnets, they have the potential to be used in microsystems with good temperature stability of up to 250 °C unlike many rare earth permanent magnets that soften upon warming and lose the remanence magnetization when broken into small particles [85]. NWs are also interesting for their easy, cost-effective, large scale and low-temperature fabrication that makes it easy to be produced in any laboratory without needing sophisticated equipment. Fe is selected among other commonly used ferromagnetic NWs materials reported in literature for its relatively high saturation magnetization (*Ms*) as reported in Table 3-1. High coercivity of Fe NWs is an important feature that allows achieving the desired permanent magnetic properties. It has been proven that Fe NWs in general exhibits higher coercivity than Ni or Co NWs [83, 86-88]. Magnetic properties of Fe NWs ranging from 10-100 nm in diameter have been studied by a number of groups [83, 86-88], confirming the validity of the material selection in this dissertation and the potential of Fe NWs to act as nanoscale permanent magnets. Another reason for choosing Fe NWs is their high degree of biocompatibility as will be shown in this dissertation (section 3.3.5).

NWs Material	***Ms* (emu/cm^3)**
Fe	1080 - 1707
Co	1400
Ni	480 - 485

Table 3-1: Saturation magnetization comparison for common ferromagnetic nanowires materials [83, 89-91].

3.2.3 Nanocomposite Synthesis

The permanent magnetic and highly elastic nanocomposite was synthesized by mixing Fe NWs with certain concentration into a PDMS solution. The NWs were dispersed in ethanol, and then washed in Sodium dodecyl sulfate (SDS) surfactant to reduce the agglomeration from surface tension. PDMS (Sylgard 184 Silicone Elastomer, Dow Corning Corporation) was used as the polymeric matrix. After mixing the NWs with minimized amount of SDS with PDMS solution to form the nanocomposite, desiccation for 30 minutes was carried out to remove trapped bubbles and assist the evaporation for any remaining SDS debris. Vortexing was then conducted using mini vortex mixer (Fisher Scientific, model 02-215-360) for 20 minutes to improve dispersion and reduce aggregates and agglomeration of the NWs with the help of the SDS surfactant. The NWs can be aligned in the nanocomposite to the required direction using a C-shaped permanent magnet that can provide a uniform magnetic field of 2 kOe. The nanocomposite can be cast into the shape required and then placed along with the magnet in a desiccator for 30 minutes to remove trapped bubbles. The nanocomposite was cured at 90 ^{0}C for 1 hour. The concentration of NWs in the nanocomposite cilia was calculated in terms of *NWs:PDMS* volume ratio (v%):

$$NWs : PDMS(v\%) = 100 \times \frac{v_{NWs}}{v_{PDMS}} \qquad 3\text{-}4$$

The NWs to PDMS volume ratio was quantified experimentally by measuring the saturation magnetization of a nanocomposite sample and comparing it to the saturation magnetization of a reference sample that contains NWs with a known volume. The volume of the NWs in the nanocomposite sample can then be calculated by comparing the nanocomposite saturation magnetization *Ms* (measured in emu), to the reference sample saturation magnetization *Ms* (in emu/cm^3). This comparison provides the volume of the NWs used in the comparison to the volume of the tested nanocomposite sample to obtain the *NWs:PDMS* volume ratio. To obtain the reference sample's saturation magnetization *Ms*, an AAO membrane sample was studied with electrodeposited Fe NWs. An SEM image is obtained for the top side of the membrane which shows that each pore has an average diameter of 40 nm (Figure 3-4a). By selecting an AAO membrane area of 0.25 µm^2, 27 pores were found with total pores area of 0.034 µm^2 (pore area/membrane area = 14%). A cross section SEM image was obtained for the AAO membrane with deposited Fe NWs. The image shows a variation in the NWs deposition length with average length of 6 µm (Figure 3-4b). The hysteresis loop of Fe NWs-filled AAO membrane with an area of 0.01 cm^2 was obtained along the length direction of the NWs as shown in Figure 3-4c. The saturation magnetization was found to be 0.682 memu. The average volume of the NWs in the reference sample was 84×10^{-8} cm^3 ($0.14_{\text{(pores ratio)}}\times0.01\ \text{cm}^2{}_{\text{(AAO area)}}\times(6\times10^{-4})\ \text{cm}_{\text{(NWs length)}}$). The saturation magnetization of the reference sample was found to be 812 emu/cm^3. This value is less than the magnetization range found in literature for bulk Fe materials (section 3.2.2). This is attributed to having a thin magnetite shell around the NWs that reduces the magnetization, in addition to the fact that average lengths and diameters were used in the calculation of the magnetization.

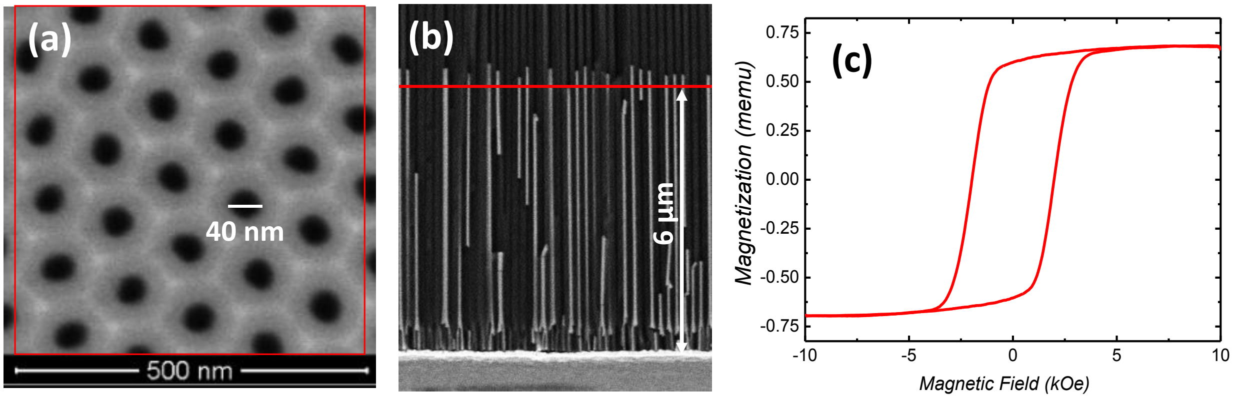

Figure 3-4: (a) SEM image of AAO membrane top view showing the studied area and the average pore diameter. (b) Cross-section image of AAO membrane showing the NWs length variation and the average length used in the calculation. (c) Hysteresis loop of Fe NWs used in the reference sample study.

A high concentration of NWs in the nanocomposite is desired to increase its magnetization. Practically, the concentration can be maximized to a level where mechanical or magnetic degradation occurs to the nanocomposite. High NWs concentrations can lead to a stiff nanocomposite, and can significantly affect the cross-linking of PDMS. Experiments have been carried out in Section 3.7.2 to investigate the effect of NWs loading on material stiffness. Increasing the NWs concentration in the nanocomposite is desired to increase the remanent magnetization of the nanocomposite for better sensing performance. Ideally, a single nanowire will have a remanent magnetization equivalent to the saturation magnetization, and the magnetization density in the nanocomposite increases linearly as the amount of NWs increases. However, when the NWs density increases in the nanocomposite, magnetostatic dipole interactions occurs between the NWs. This interaction between the neighboring NWs causes a high demagnetization field that reduces the nanocomposite remanent magnetization as discussed in sections 3.2.2 and 3.6. Due to these factors, it is essential to optimize the

NWs concentration in the nanocomposite to meet the requirements and avoid the side effects.

3.3 Electrochemical Deposition of Fe NWs

A traditional method to produce arrays of magnetic nanoparticles and NWs is nanolithography [92, 93]. However, this method is expensive and does not allow providing a large yield. Recently, self-assembled and naturally occurring porous media have been investigated as templates for NWs fabrication [94, 95]. This technique provides a large-area of nanopatterns with a high aspect ratio which is a difficult task for conventional lithography techniques.

In this dissertation, Fe NWs were fabricated utilizing an efficient, out-of-cleanroom and cost-effective method utilizing an attractive self-ordered nanoporous template method. The NWs were electrodeposited inside a porous Anodic Aluminum Oxide membrane (AAO) that was prepared in-house using an anodization process. Anodization of aluminum is an electrochemical oxidation process used for synthesizing ordered porous structures, consisting of a hexagonal array of uniform cylindrical nanopores perpendicular to the substrate surface [96-99]. The self-assembled and highly ordered hexagonal nanoporous AAO membranes are ideal templates for homogenous nanomaterials fabrication, with controllable pore size and spacing.

3.3.1 Anodic Aluminum Oxide (AAO) Membranes Fabrication

AAO membranes were prepared using a 99.999% high purity Al substrates that are 500 μm thick and 2.5 cm in diameter. The substrates were cleaned and polished before starting the anodization process. The cleaning was carried out to remove organic contamination by dipping the Al substrates in acetone bath and performing ultra-sonication for 5 minutes. The substrates were then washed with Isopropyl alcohol (IPA) and deionized (DI) water. An electro-polishing step was then conducted to remove the aluminum oxide layer and reduce surface roughness on the substrate prior to starting the electrochemical anodization processes. The step was conducted by dipping the Al vertically in a bath of a mixture of perchloric acid and ethanol (HClO4:C2H5OH = 1:4). An electrode made of a platinum mesh was used and placed perpendicular to the Al substrate. The process was conducted for a single Al substrate, and a constant current of 2 A was applied between the disk and the electrode for 3 minutes resulting in a shiny and smooth Al surface. The electro-polishing set up is illustrated in Figure 3-5.

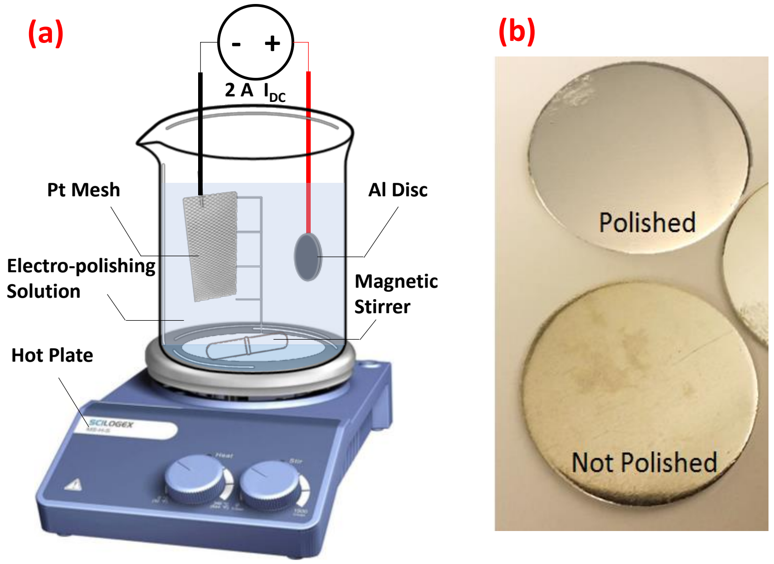

Figure 3-5: a) Illustration for the electro-polishing set-up. b) Example of polished and not polished Al disc.

After cleaning and polishing the Al substrate, two anodization steps were performed to oxidize one side of the aluminum substrate and form a porous alumina membrane. The properties of AAO membranes varies depending on the anodization potential, operating temperature, and selection of the oxidizing agent. The pore diameter and spacing between the pores can be adjusted by modifying the anodization voltage and the oxidizing agent. For instance, oxalic acid ($C_2H_2O_4$) was used for diameters between 30 nm and 70 nm, while phosphoric acid (H_3PO_4) was used for diameters larger than 100 nm. Diameters smaller than 30 nm can be achieved by using sulfuric acid (H_2SO_4). AAO membranes have high pores density. Typically, the pore diameters are 33% to 50% of the interpore spacing [97]. By using 0.3 Mol/L oxalic acid as the oxidizing agent, a temperature of -1.6 °C and a constant anodization voltage of 40 V, the AAO membranes were optimized to have 20 μm thick porous alumina with pores diameter of 35-40 nm.

To perform the anodization process, up to four Al substrates are mounted between a Teflon cell and a copper electrode where Teflon has holes to expose one surface of Al to oxalic acid. The other side of Al was directly in contact with copper as a counter electrode. The copper electrode was placed on a chiller plate to bring down the operating temperature of oxalic acid ($C_2H_2O_4$) to -1. 6 °C by cooling it through the copper and the Al substrate. After waiting for about 1 hour to stabilize the temperature, the first anodization process was carried out for 24 hours by applying 40 V between the backside of Al and a platinum mesh spaced by 1 cm. The oxidizing agent covers the surface of Al and the platinum mesh, and it was mechanically stirred using a DC motor to ensure a uniform anodization process and to eliminate the formation of air bubbles near the substrates. By monitoring the anodization current throughout the process, the current was typically constant at a value between 2-3 mA/substrate. This step resulted in alumina membrane but with having randomly oriented pores. Figure 3-6 shows the used anodization cell before and after the assembling procedures. The fabrication cell is made of Teflon due to its great chemical resistance. The experimental set up for the anodization process is shown in Figure 3-7.

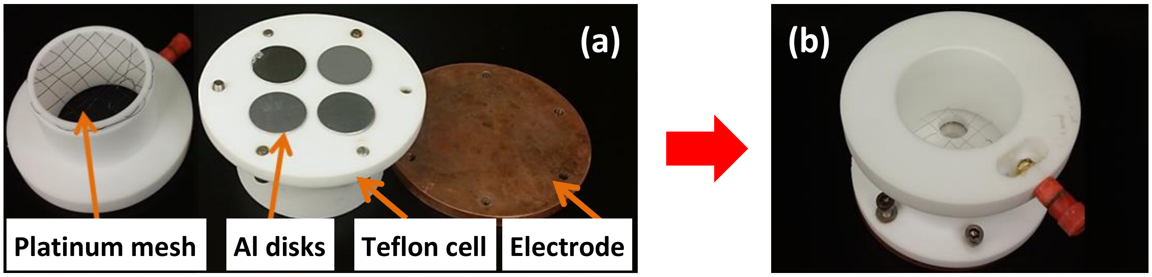

Figure 3-6: Image of the 4-disc anodization cell (a) before, and (b) after assembling.

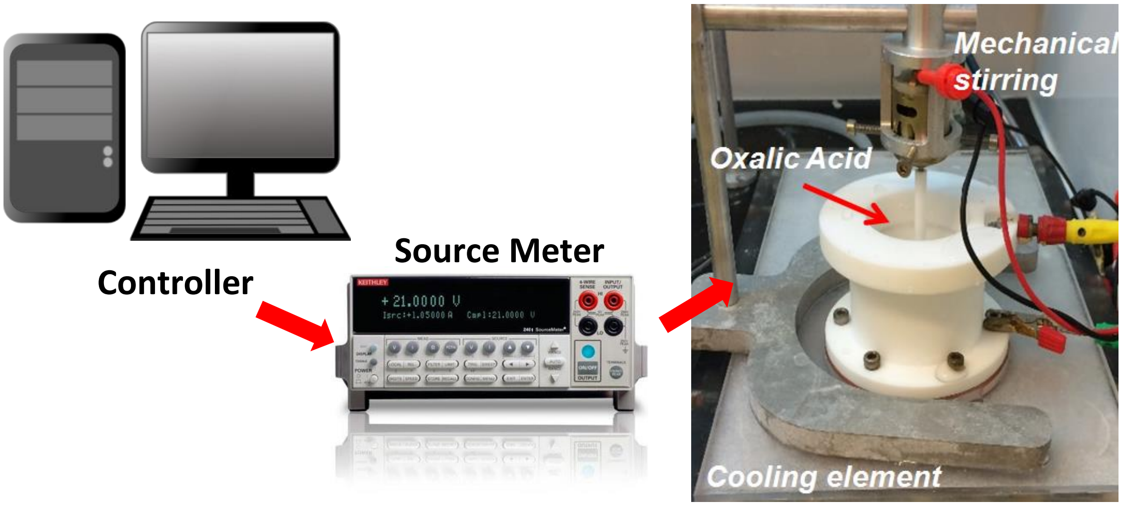

Figure 3-7: Experimental set up for the anodization process

After the first anodization, oxalic acid was removed, and the samples were washed without disassembling the Teflon cell. The random porous alumina membrane was then etched away using an alumina etchant (chrome solution (mixture of CrO_3 and H_3PO_4)) as described in Table 3-2. Etching usually takes 24 hours at room temperature but can be reduced to 12 hours by heating the chrome solution to 40 °C using a hotplate to help enhancing the reaction. After etching the alumina, ordered indentations were present on the Al surface that were utilized to grow a more uniform highly ordered hexagonal nanopores through the second anodization step.

The Al substrates were then washed with DI water, and oxalic acid was placed again in the cell along with the platinum mesh and the stirrer to perform the second anodization process. Utilizing the uniform indentations resulted from the first anodization process, highly oriented hexagonal pores were obtained. This second anodization process was carried out for 10 hours using the same parameters used in the first anodization step. AAO membranes of 35-40 nm pore diameter and 20 μm thick were obtained. The resulted cylindrical pores have an alumina barrier layer at the bottom. To open an interface between the electrodeposition solution and the bottom electrode, cracks formation and barrier reduction step was performed that takes one hour. This process is referred to as the dendrites formation step: an anodization-like process with few modifications. In this process, an anodization step with fixed current (instead of constant voltage) is carried out that increases the ratio of the barrier reduction to the oxide formation rate. The anodization voltage reduces from 40 V until it reaches a low value of about 6 V. As the anodization voltage keeps decreasing, the barrier gets thinner and forms cracks that allow charge transfer [98]. Illustrations of the AAO fabrication process is shown in Figure 3-8. Figure 3-9 shows a top-view and cross-section of scanning electron microscopy (SEM) image of the AAO membrane after the second anodization. SEM is the most electron microscopy imaging technique that can provide microstructural and surface morphology analyses with nanoscale resolution. In this dissertation, SEM analysis is carried out using FEI Quanta 200 and Quanta 3D SEM.

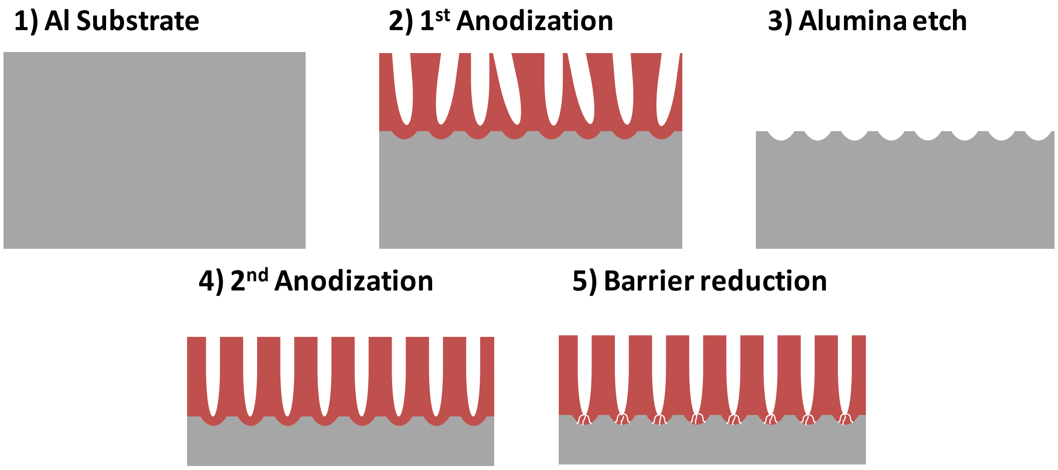

Figure 3-8: Schematic drawings of AAO fabrication process.

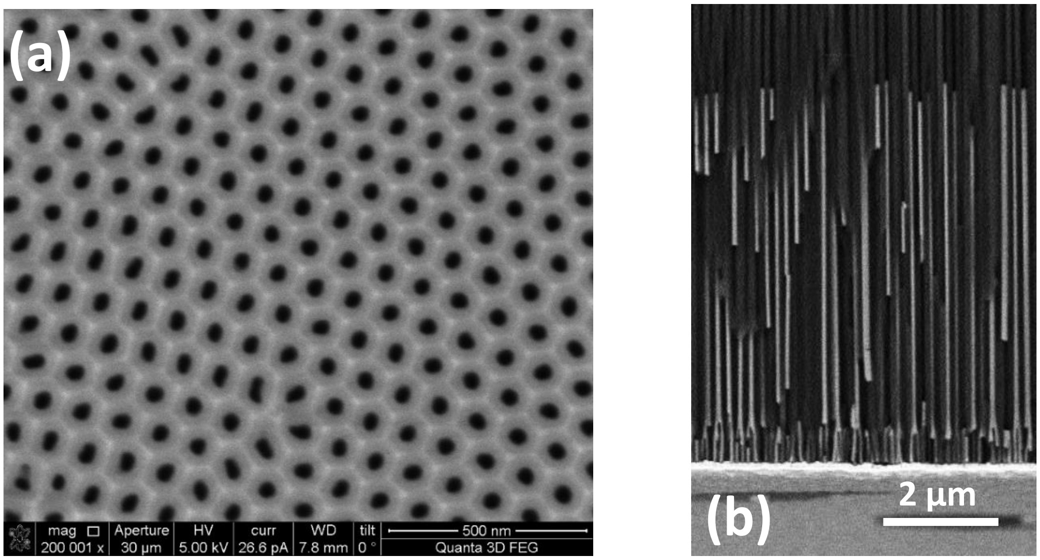

Figure 3-9: (a) SEM image of AAO membrane after the second anodization. (b) SEM cross-section image of the AAO membrane showing the formed dendrites.

3.3.2 Electrodeposition Technique

Electrodeposition is an electrochemical process for metallic materials deposition through the chemical reduction of metal ions from an aqueous electrolyte. A chemical reaction occurs between metal ions dissolved in aqueous solution and electrons provided by an external power source through a metallic electrode contacted directly to the solution. Deposition typically occurs at the interface of charged particles and the metallic electrode (i.e. Al substrate) [100]. The basic components for the electrodeposition setup include electrodes (cathode and anode), and electrodeposition solution as shown in Figure 3-10.

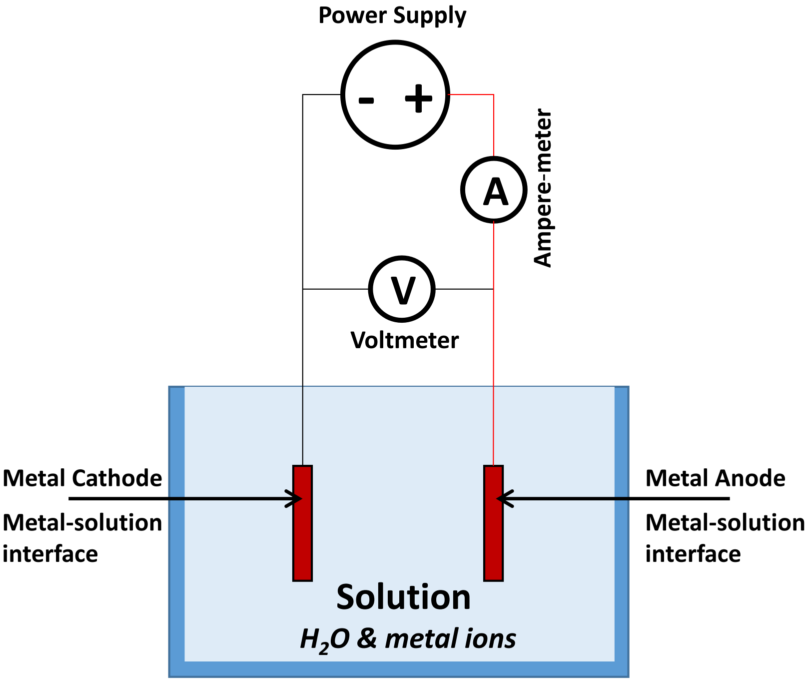

Figure 3-10: Illustration of the basic electrodeposition process of metals from an aqueous solution.

Two common techniques can be used to electrodeposit Fe NWs: DC deposition [101], and pulsed deposition [94, 97]. In this dissertation, electrodeposition of NWs into AAO membranes was conducted using pulsed deposition method that requires a deposition electrolyte solution containing metal ions of Fe, as discussed earlier. Pulsed electrodeposition takes place at the barrier between the alumina membrane and Al substrate, and pulses are applied directly to the aluminum side of the AAO membrane. A better deposition process and improved NWs quality and homogeneity are obtained by the barrier reduction and dendrites formation process described in section 3.3.1, which lead to a lower potential required for electrons tunneling through the barrier. A specific pattern is used for the pulsed deposition to ensure a successful deposition process and uniform filling of the pores [94, 97]. A negative pulse is first applied to force the metal ions to settle to the bottom of the pores. A short positive pulse is followed to discharge the barrier layer. A delay time between successive deposition pulses is considered to give metal ions sufficient recovery time. The pulses are then repeated for the required duration, and deposition rate of Fe NWs can be calculated with respect to time and with respect to the pattern of the pulse.

NWs grow according to Faraday's law of electrolysis [98, 102, 103]. The law can be summarized by the following equation:

$$m=(Q/F_c)\ (MW/n) \qquad 3\text{-}5$$

where m is the mass of the electrodeposited material, Q is the total electric charge passed through the material, F_c is Faraday constant which is equal to 96485 C mol^{-1}, MW is the molecular weight of the material and n is the number electrons transferred per ion.

The setup for Fe NWs electrodeposition inside the AAO membrane is similar to the setup of anodization process where a Teflon cell with bottom copper electrode, and a platinum mesh are used. In the electrodeposition process, one AAO membrane only was used in each cell. Pulsed electrodeposition was used at room temperature, and nitrogen purging was continuously applied to the electrodeposition solution to prevent solution oxidization. The Fe electrodeposition bath was composed of 45 g/L iron sulfate Fe_2SO_4, 30 g/L boric acid H_3BO_3 and 1 g/L ascorbic acid $C_6H_8O_6$. The pulse pattern of Fe NWs uses negative pulses with a current density limit of -60 mA/cm^2, deposition pulses of -40

V in amplitude, and 8 ms pulse duration. In order to obtain a homogenous deposition, the pulse patterns are separated by 2 ms and 3 V short positive polarization pulses with a current density limit of -60 mA/cm^2, followed by 0.7 s resting pulses of to refresh the ion concentrations. This process resulted in a deposition rate of 1.5 µm/hour. Fe NWs in this dissertation were selected to be 6 µm long and 35 nm in diameter. Figure 3-11 shows schematics for the experimental set up for pulsed electrodeposition inside AAO membrane, with showing the pulse pattern.

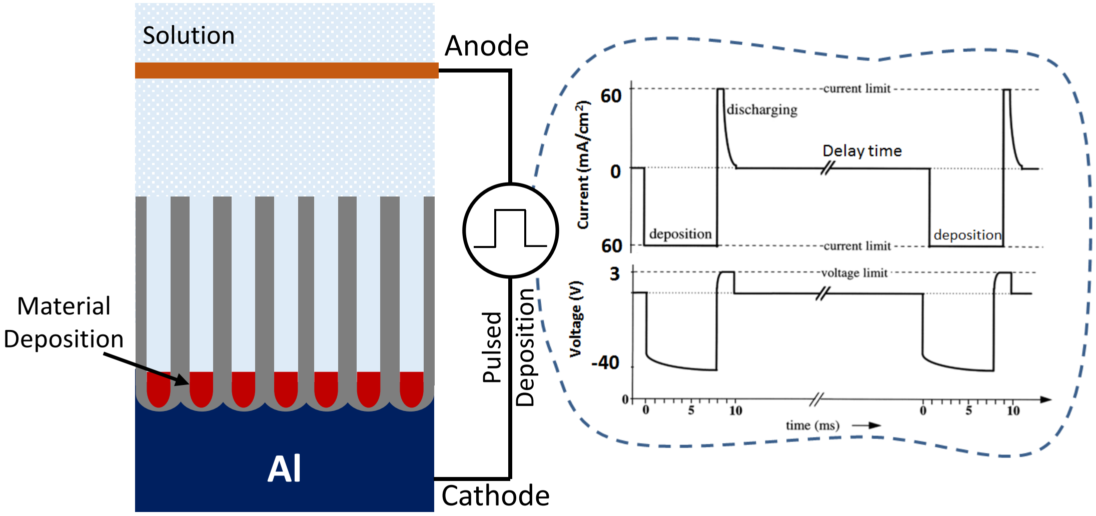

Figure 3-11: Illustration of the pulsed electrodeposition, showing the pattern of the pulses (adapted from [98]).

3.3.3 Nanowires Releasing Process

After fabricating the NWs inside the AAO membrane with the desired length, they can be released by dissolving the AAO membrane with a selective chemical etchant. After placing the sample in an Eppendorf tube, a tube holder with a permanent magnet in the side was used to attract the NWs after the release. NaOH is used for 1 hour at room temperature that dissolves part of the alumina membrane and peels it off the Al substrate.

The de-attached Al was removed from the tube, the remaining AAO membrane with the NWs was washed from NaOH using DI water and replaced with chrome solution to conduct a second etching step that allows dissolving alumina completely. The Eppendorf tube with the NWs and chrome solution was placed in a water path placed on a hot plate with a thermocouple to ensure the operation at 40 °C. Etching was performed for 24 hours in chrome solution with constant agitation. After the NWs release process, they were washed with several ethanol cleaning steps to remove contaminations and chemical debris from the released NWs. The NWs were then washed and kept in Ethanol. The complete NWs fabrication process is shown in Figure 3-12. The fabricated NWs in the AAO membrane and after the release process are shown in Figure 3-13. The chemical solutions used during the fabrication of AAO membranes and Fe NWs are listed in Table 3-2.

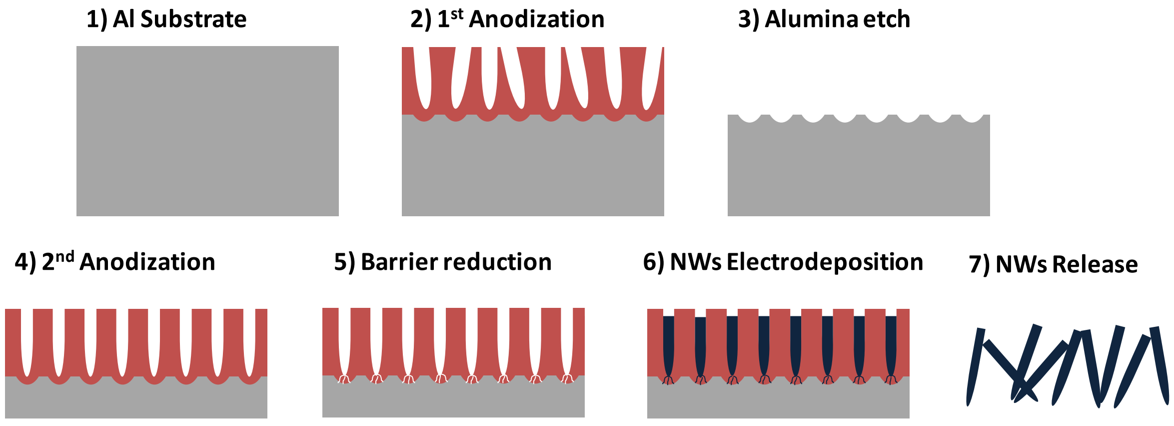

Figure 3-12: Illustrations of the NWs fabrication process.

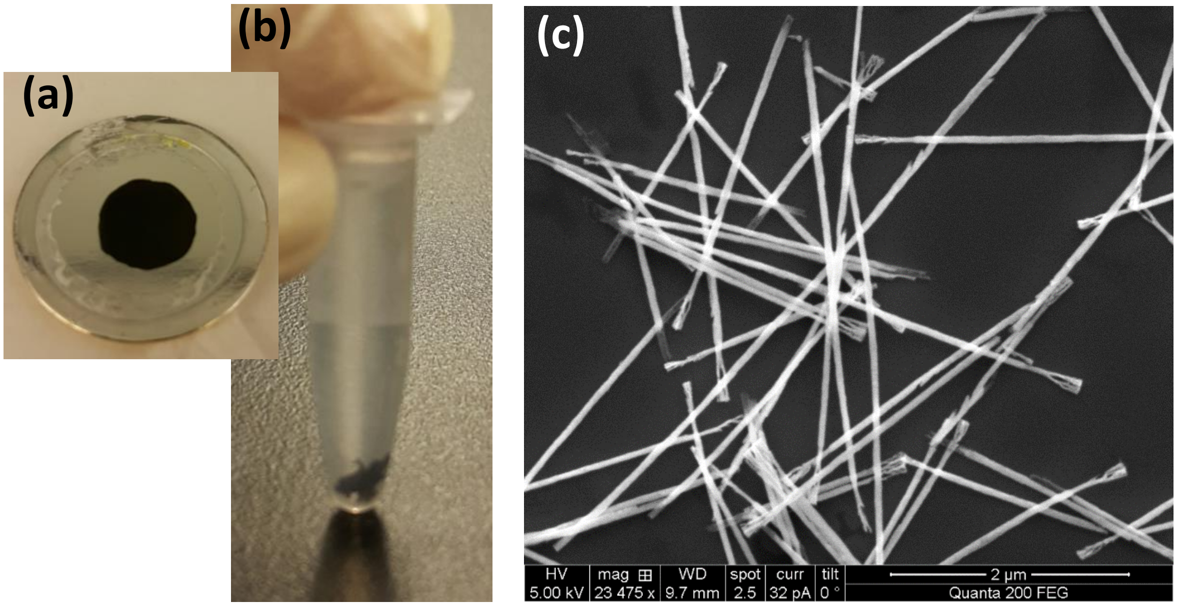

Figure 3-13: (a) Optical image of AAO membrane with deposited Fe NWs. (b) Released Fe NWs and dispersed in ethanol. (c) Scanning electron microscopy image of 6 µm long and 35 nm in diameter Fe NWs.

Function	Solution	Formula	Preparation
Electro-polishing	Perchloric acid Ethanol	HClO4 C2H5OH	25 ml of 70% $HClO_4$ into 75 ml of C_2H_5OH
Anodization	Oxalic acid	C2H2O4	3.78 g of 99.5% $C_2H_2O_4$ into 100 ml of DI water
Alumina Etching (Chrome Solution)	Chromium(VI) oxide Phosphoric acid	CrO3 H3PO4	1.8 g of CrO_3 and 5.76 g of 85% H_3PO_4 in 100 ml DI water
Fe NWs Electrodeposition	Iron Sulfate Boric Acid Ascorbic Acid	Fe_2SO_4 H_3BO_3 $C_6H_8O_6$	Mixture of 45 g/L Fe_2SO_4, 30 g/L H_3BO_3 and 1 g/L $C_6H_8O_6$ in 100 ml DI water

Table 3-2: Chemical solutions used for the fabrication of AAO membranes and Fe NWs electrodeposition.

Figure 3-14 shows the transmission electron microscopy (TEM) image of several polycrystalline Fe NWs with grain size in the range of tens of nanometers. TEM is a famous electron microscopy technique that has several modes of operation. The selected area diffraction (SAED) pattern, shown in the inset, identifies the *bcc* phase of Fe.

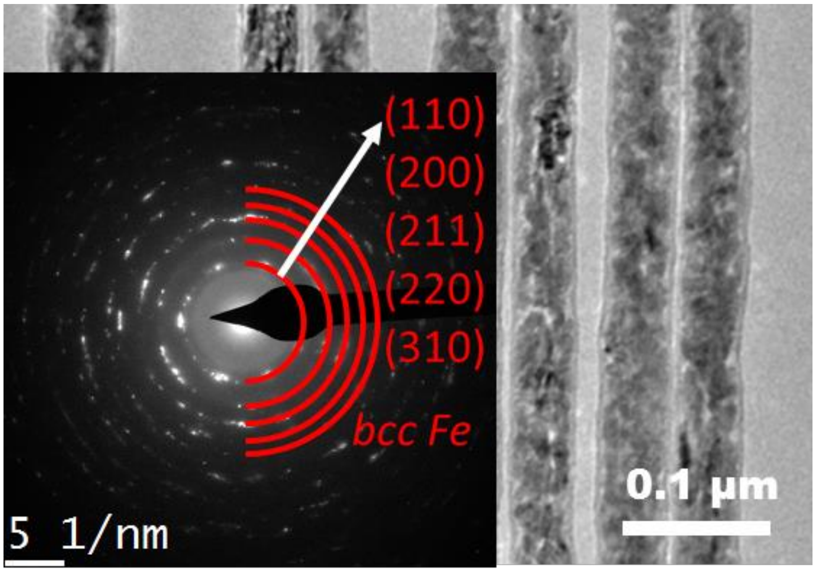

Figure 3-14: Bright field transmission electron microscopy image and selected area diffraction pattern of as-fabricated polycrystalline Fe NWs.

3.3.4 Nanowires Topography and Magnetic Characterization

The fabricated Fe NWs were studied with atomic force microscopy (AFM) to observe their topography. AFM is a physical microscopy technique that uses a sharp probe to determine the sample topography. In this dissertation, AFM is utilized for high-resolution topography imaging for individual NWs as shown in Figure 3-15a.

Magnetic force microscopy (MFM) was used to study the magnetic properties of individual NWs and confirm the single domain state. The MFM system is similar to AFM with using a magnetic-tip probe instead of the regular probe. MFM measures magnetostatic forces between the tip and the magnetic sample upon scanning at a constant height. The tip exhibits repulsive or attractive forces, changing the resonance properties of the cantilever that holds the tip. The MFM image is then constructed by mapping these forces [104]. MFM images were recorded in lift-off mode (100-nm distance) with an MFP-3D-Bio from Asylum Research scanning probe microscope using standard atomic force microscopy nano-sensor probes with a Co-Cr magnetic coating on a Si tip. A single NW was selected using a scanning electron microscopy and its position was marked with a focused ion beam. MFM measurements were done in the remanent state after applying magnetic fields parallel to the NW's axis using a variable magnetic field module (±5kOe).

A NW was first saturated under a field applied parallel to its axis and then scanned at remanence. Afterward, the applied field was reversed in steps of 20 Oe. After each step, the field was removed to avoid any effect~~s~~ caused by the stray field from the magnetic tip, and a scan was conducted. The coercivity is defined as the field at which the MFM contrast of the NW is reversed. At remanence, the black and white points at the ends of the NW are caused by strong magnetic stray fields and confirm the single domain magnetic state with the magnetization along the NW's axis for both polycrystalline NWs (Figure 3-15b,c). The MFM contrasts found along the polycrystalline NW are due to stray fields originating from local defects of the NW shape. After saturating the NWs in the opposite direction, the MFM contrast at remanence appears reversed, indicating a change of the magnetization direction. Magnetization reversal from one saturation state to the opposite one occurs at around the coercive fields (Figure 3-27). This magnetization reversal mechanism is in agreement with previously reported micro-magnetic simulations, showing a reversal process by switching of the magnetization direction at the coercive field via vortex domain wall propagation [105].

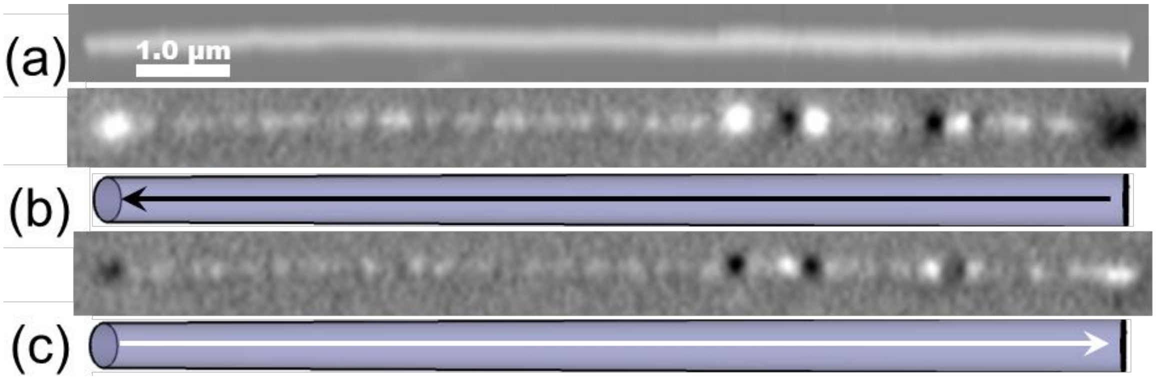

Figure 3-15: (a) AFM image of polycrystalline Fe NW topography; (b) and (c), are MFM images at remanence after saturation in opposite directions. The drawings schematically show the direction of the NW magnetization.

3.3.5 Nanowires Biocompatibility Study

Fe and Fe_3O_4 are most suitable NW materials for biomedical applications, because of their low-toxicity and biocompatibility [106-109]. The biocompatibility of Fe NWs along with oxidized NWs (Fe_3O_4) discussed in section 3.9.1 are assessed using the MTT (3-(4, 5-dimethylthiazol-2yl)-2, 5-diphenyl tetrazolium bromide) assay. This assay measures the cell metabolic activity, hence, it is a good indicator of cell health and viability. The assay is used to assess the cytotoxicity of the Fe and Fe_3O_4 NWs. HCT 116 colon carcinoma epithelial cells (ATCC® CCL247TM) are cultured in McCoy's 5A modified medium (Gibco®), supplemented with 10% fetal bovine serum (Gibco®) and L-glutamine, and grown in a 37 ^{0}C humidified incubator with 5% CO_2. Upon reaching 80% confluence, cells are detached from the culture flasks with 0.25% trypsin-EDTA and counted using trypan blue staining. The cells are cultured in 96-well plates and after 24 hours of stabilization, they are treated with the NWs at different NW-to-cell ratios (number of NWs per cell in the culture at the time of treatment). After the desired incubation times, the cell medium is discarded and replaced with 10% MTT solution —5 mg/mL in phosphate buffered saline — in McCoy's medium. The cells are incubated for two hours; then the medium is discarded and replaced with 90% dimethyl sulfoxide – 10% sodium dodecyl sulfate lysis buffer to dissolve the MTT reduction products. The cell viability is evaluated through optical density with a microplate reader (XMarkTM, Bio-Rad) using a wavelength of 570 nm and a background wavelength of 630 nm.

Figure 3-16 shows the cell viability of HCT 116 cells incubated with three concentrations of Fe and Fe_3O_4 NWs for 24, 48 and 72 hours. Fe_3O_4 NWs appear to be slightly more biocompatible than pure Fe NWs. There was no statistically significant decrease in cell viability for most of the conditions tested for the two NW materials. Only at the highest concentrations and incubation times a significant drop in cell viability was observed for Fe NWs. In general, these results show that both Fe and Fe_3O_4 NWs possess a good biocompatibility and are not cytotoxic to the model cell line used.

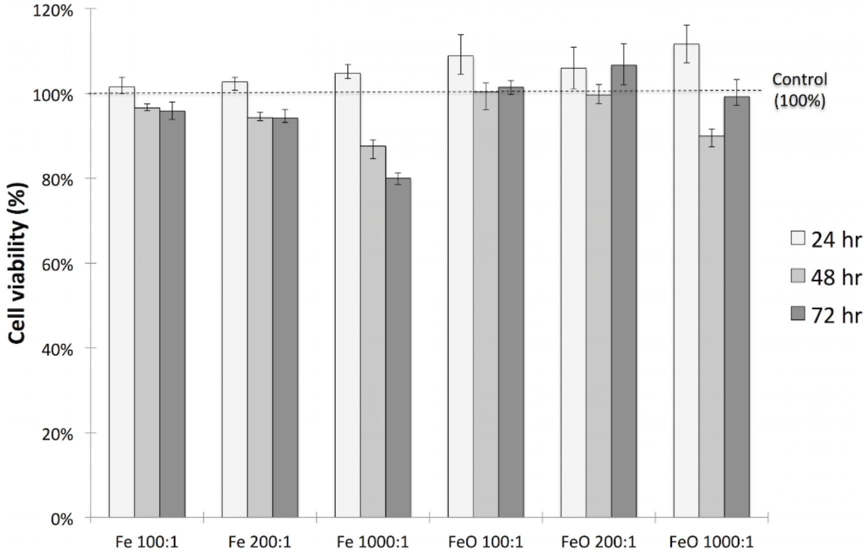

Figure 3-16: MTT assay for the assessment of the viability of HCT 116 cells incubated with Fe and Fe_3O_4 NWs for 24, 48 and 72 hours. The concentrations on the x-axis denote the NW-to-cell ratio. The data represent mean ± range, the number of replicas was n=3.

3.4 Mathematical Model of Cilia Force Deflection

The bending motion of artificial cilia can be described by the Euler–Bernoulli beam theory (classical beam theory), in which bending is quantified with neglecting the shear deformation of the beam [110]. Using the displacement-force relationship of an elastic cylindrical beam as illustrated in Figure 3-17a, the value of beam displacement δ can be expressed for a point load P_L applied at the free end of a beam with length l, Young's modulus E, and centroidal area moment of inertia I as shown in Eq. 3-6 (Figure 3-17b). In the case of a uniformly distributed load along the length of the beam q, the deflection can be as represented as in Eq. 3-7 (Figure 3-17c) [111, 112].

$$\delta = \frac{P_L l^3}{3EI} \tag{3-6}$$

$$\delta = \frac{q l^4}{8EI} \tag{3-7}$$

Moment of inertia I is calculated with respect to the axis which passes through the centroid of the cross-section and which is perpendicular to the applied loading. Explicitly, for a beam whose axis is oriented along z-axis with a loading along x-axis and y-axis [111]. The centroidal area moment of inertia is calculated as:

$$I = \int_A x^2 dA = \int_A y^2 dA \ . \tag{3-8}$$

In the case of a cantilever beam with circular cross section and diameter D, we find:

$$I = \frac{\pi D^4}{64} \ . \tag{3-9}$$

A point load is more relevant to the mechanism of the cilia sensor reported in this dissertation, hence, by combining Eq. 3-6 and Eq. 3-9 the deflection of a cilium with an applied force *F* that has x and y components can be computed:

$$\delta = \vec{F}\frac{64l^3}{3\pi ED^4} = \left(\vec{F}_x + \vec{F}_y\right)\frac{64l^3}{3\pi ED^4} \quad . \tag{3-10}$$

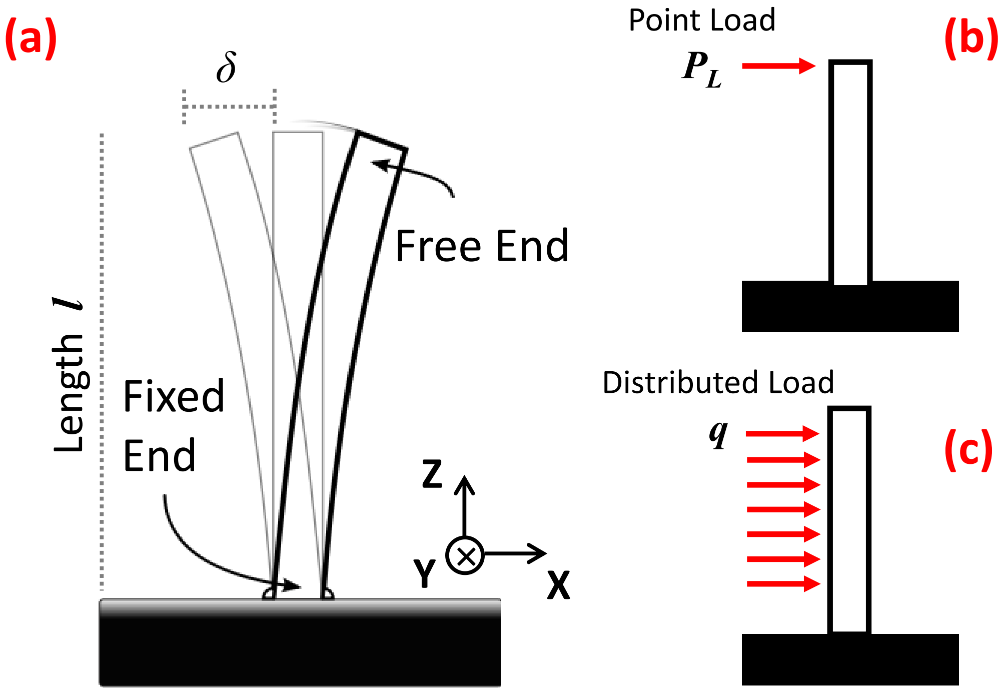

Figure 3-17: (a) Illustration for the deflection of a cantilever beam subjected to (b) a point load, or (c) a uniformly distributed load.

3.5 Cilia Fabrication Using Master Mold Techniques

3.5.1 General Fabrication Process

The nanocomposite cilia were fabricated using a master mold technique where the mold has an array of holes with a diameter corresponding to the cilia diameter, and mold thickness corresponding to the cilia length. Two types of molds were utilized: (i) cost effective and simple-to-fabricate polymer molds for cilia with diameters larger than 100 µm, and (ii) silicon molds for smaller diameters with a maximum cilia length of 500 µm. The NWs-PDMS nanocomposite was used with different NWs to PDMS volume ratios to meet the needs of specific applications and at the same time to avoid adversely affecting the polymerization process of the PDMS or the elasticity of the cilia.

A thin PDMS layer of 10 µm thickness was first spun on the surface of the magnetic sensor fabricated on glass, silicon, or flexible Kapton substrates (details in section 3.10.2) to provide proper electrical insulation and ensure the adhesion of the nanocomposite cilia to the substrate. To increase the adhesion of the cured PDMS based nanocomposite to the substrates in general, a surface treatment procedure was conducted by a 10-minute oxygen cleaning using reactive ion etch (RIE) (Oxford Instruments). The following recipe was used: O_2= 60 sccm, Pressure= 200 mTorr, RF= 100 W, time= 30 seconds. The nanocomposite (synthesis described in section 3.2.3) was cast on the substrate, and the master mold was mounted on top of it such that the cilia are aligned on top of the GMI sensor. The NWs in the nanocomposite can be aligned to the required direction using a directional and uniform magnetic field. A C-shaped permanent magnet that can provide a uniform magnetic field of 2 kOe was used in this work. The nanocomposite in the mold along with the magnet, if relevant, were placed in a desiccator for 30 minutes to remove any trapped air bubbles and assist in filling the pores. Next, the nanocomposite was cured at 90 degrees Celsius for 1 hour using an oven (Thermo Scientific PR305220M), forming the cilia on top of the magnetic sensor's surface. After releasing the cured cilia, they were fully magnetized by applying a magnetic field of 10 kOe using the VSM system mentioned in section 3.6. The fabrication process is illustrated in Figure 3-18.

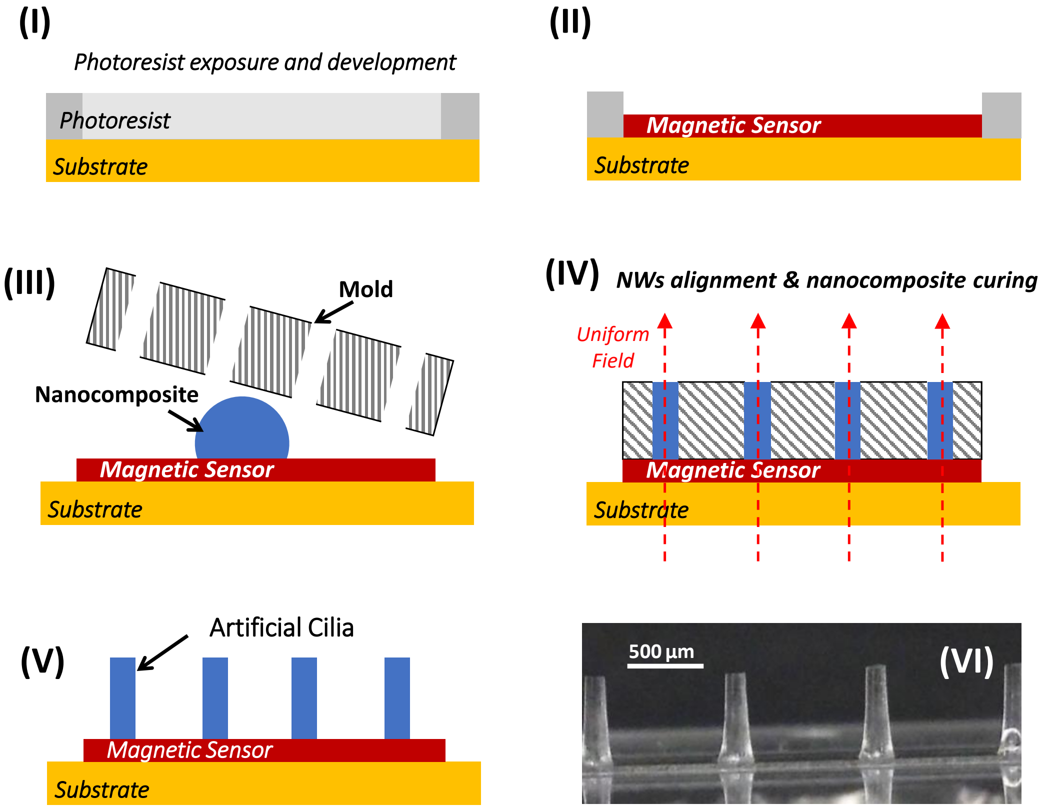

Figure 3-18: Illustration of the fabrication process of the magnetic nanocomposite cilia tactile sensor. (I,II) Magnetic sensors are fabricated using standard lithography process, and e-beam evaporation. (II-V) Cilia are fabricated using a PMMA mold technique, and applying a homogeneous magnetic field aligns the NWs. (VI) Scanning Electron Microscopy image of a 500 µm in length and 100 µm in diameter cilia.

3.5.2 Poly-methyl methacrylate (PMMA) Mold

3.5.2.1 Introduction

Conventionally, 3D microstructures are fabricated using standard lithography processes, which is generally regarded as an expensive and time-consuming method, because it demands cleanroom environment and expensive instrumentation [113]. Moreover, realizing high aspect ratio microstructures is difficult and limited in thickness. Motivated by the growing demand for inexpensive fabrication technologies, recent research efforts have been focusing on seeking alternatives to conventional cleanroom processes. Attention has been drawn to laser ablation techniques, which produce patterns with a reasonably good resolution [114-116].

A master mold technique is an attractive approach for the fabrication of the PDMS-based cilia. A fast and simple method to fabricate polymer-based molds is the direct laser ablation technique. The laser ablation method offers a mask-free and out-of-cleanroom processing which reduces the fabrication time and complexity. CO_2 lasers are commonly used for patterning and engraving due to their lower cost and higher commercial availability [117]. The working mechanism of CO_2 laser machining is known as photo-thermal ablation, where bonds are broken by the elevated temperature produced by emitted radiation. The focused CO_2 laser output directed on the material surface rapidly rises its temperature [118]. Patterning is executed by the continuous linear movement of the high-intensity laser beam on the sample.

Polymers are a good candidate for preparing molds to fabricate microstructures, in comparison to silicon or glass substrates, because they are cheap, easy to machine, annealable, transparent, and have a modifiable surface. Silicon and glass based molds require expensive facilities, highly trained personnel, and handling of toxic substances. In this work, poly-methyl methacrylate (PMMA) is selected as the mold material. It is a thermoplastic, which means it can be molded without losing structural integrity and can reversibly change from a hard to a soft material when reaching the glass transition temperature. The glass transition temperature for PMMA is around 120 ˚C making the materials suitable for molding and replication techniques [119]. The excellent optical transparency of PMMA [120] allows easy handling and alignment of the mold to patterns on a substrate (e.g. aligning cilia mold to the magnetic sensor on a substrate). It has been reported that PMMA, in comparison to materials like PEEK or PDMS, offers the best laser machining characteristics [117] due to the low heat capacity and heat conductance ensuring a localized rapid rise in temperature [121].

3.5.2.2 CO_2 Laser Ablation

The CO_2 laser ablation system has four parameters that can be adjusted to optimize microstructural patterns and resolution: laser power, head moving speed, pulse per inch, and the distance between the laser head and the stage. Computer-Aided-Design (CAD) software was used to draw the pattern, a CO_2 laser cutter (Universal PLS6.75) was then used to construct the mold by making micro-holes and patterns through a polymer sheet. The influence of the patterning parameters mentioned above on the fabrication of the mold is studied, and the plotted microstructures are examined with an optical microscope.

The main effect observed when varying the laser power to fabricate PMMA molds was changing the feature size of the plotted pores. Varying the laser head moving speed defines the localized heating time at the PMMA sheet, as it is ablated by the laser beam, which in turn affects the cutting profile and smoothness. The pores' depth and width have shown experimentally a direct correlation between the laser power and reciprocal relation to the laser's speed. It was found that the lowest laser speed produces straighter walls. In general, channels fabricated with high speeds tended to have jagged edges and protrusions on its walls, whereas lower speeds produced grooves with higher uniformity and better surface roughness. Both surface roughness and wall structural homogeneity were factors that affect the mold and hence produce cilia with a rough surface. An approach to reduce surface roughness, Cheng *et al.* [122] fabricated a groove using a CO_2 laser and proposed annealing the substrate at high temperatures.

In order to find the parameters most appropriate to fabricate a PMMA mold, it is necessary to characterize the pores generated by different laser powers and speeds. Throughout the experiments, the number of pulses per inch is set to be 1000 (the permitted maximum) to ensure the pulses overlapping each other reducing the number and size of dents creating a straight wall. Also, the distance between the laser head and the stage is set to the value that focuses the laser beam on the surface of the PMMA sheet, which is typically the thickness of the sheet. If the laser is out of focus, the energy acting on the material is lower which results in a lower resolution and different cutting characterization. The pulsed CO_2 laser has a wavelength of 10.6 μm and a laser beam spot with a diameter of 127 μm with Gaussian intensity distribution. On the outer edge of the Gaussian profile, temperatures will not be elevated to the level of the center.

PMMA sheets purchased from Good fellow Cambridge Limited, Cambridge, UK with a thickness of 1 mm were used to optimize the laser patterning parameters and fabricate PMMA molds with 1:5 aspect ratio (0.2 mm diameter and 1 mm long). PLS6.75 CO_2 laser cutter is used from Universal Laser Systems, Arizona USA. The workspace is a honeycomb stage with a rectangular area of 813 mm by 457 mm. PMMA sheets are fixed on the stage using tape before the cutting to prevent moving the sample. The distance between the laser head and the stage was set to be 1 mm to focus the beam on the PMMA sheet surface. A single PMMA sheet was first used, and an experiment was carried out to study the effect of varying the power (p) and speed (s) while keeping the p:s ratio. The aim was to see the relationship between the p:s ratio and the resulting pores formation. The speed was chosen to be low for better uniformity and less sidewall roughness. By using p=10% (100%=75 Watts) and s=2% (100%=0.41 m/s (x-direction) or 100%=0.25 m/s (y-direction)), we obtain pores that have diameters of d_{top}=350 µm and d_{bottom}=90 µm (220 µm average diameter d_{avg} and 1:4.5 aspect ratio) as shown in Figure 3-19a. By increasing the power to 30% and speed to 6%, almost the same dimensions were obtained as shown in Figure 3-19b. This result indicates that by keeping the power-to-speed ratio, the same patterning characteristics can be obtained. The patterned mold can then be used such that the top patterned PMMA surface is used as the bottom side of the mold to easily peel off the fabricated nanocomposite cilia. By increasing the p:s ratio from 5 to 20 using p=40% *and* s=2%, the pores' diameters increase to d_{top}=600 µm and d_{bottom}=240 µm (d_{avg}=420 µm, and 1:2.4 aspect ratio) (Figure 3-19c). These results indicate that lower power-to-speed ratio can minimize the average pores' diameters. By increasing the power-to-speed ratio, the average diameter increases, and hence, the aspect ratio reduces which is not preferred for the cilia fabrication process. A noticeable difference between the top and bottom diameters and less straight side walls were obtained. The main reason for having the difference between the top and bottom diameters is the laser reflection and the Gaussian distribution of the laser intensity, which has been confirmed in previous studies (Figure 3-20) [117].

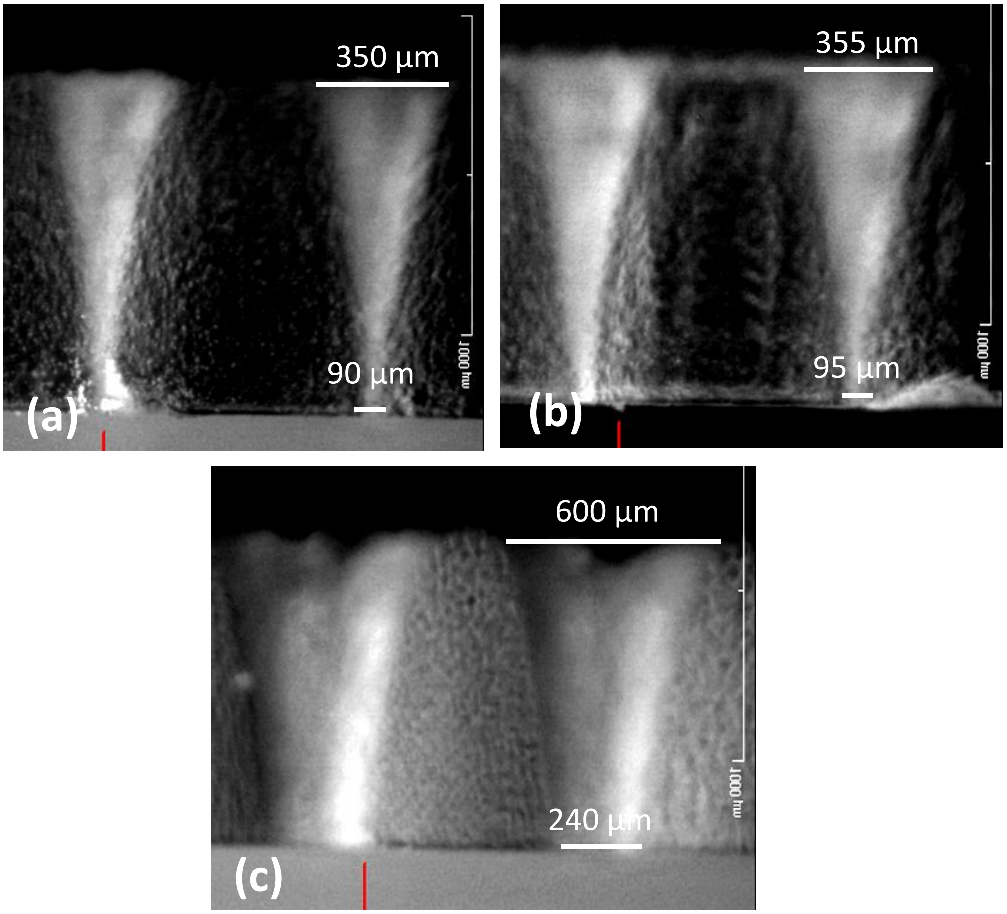

Figure 3-19: Microscope images of single laser patterned PMMA sheets with: (a) p=10%/s=2%, (b) p=30%/s=6%, (c) p=40%/s=2%.

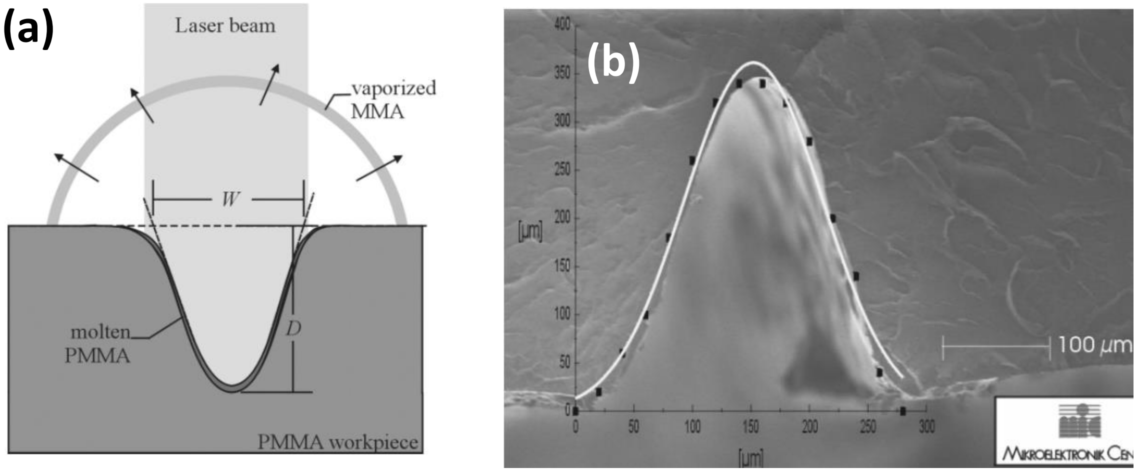

Figure 3-20: (a) Schematic of the CO_2 laser beam micromachining a PMMA groove, showing the molten and vaporized PMMA. (b) SEM image of a patterned cross-section in PMMA, showing the Gaussian fit. (Adapted from reference [117])

To obtain cilia with 1:5 aspect ratio and reduce the top and bottom variation in the pores diameters due to laser Gaussian distribution, mold fabrication using multi-stack PMMA sheets was investigated. A triple stack technique was used such that the low-intensity tails of the laser's Gaussian distribution are affecting the top sheet and minimized in the bottom sheets. Four samples were fabricated using different *p*:*s* ratios as shown in Figure 3-21, where each sheet is 1 mm thick. The distance between the laser head and the stage was set to be 1 mm to focus the beam on the surface of the bottom (third) PMMA sheet. The different fabrication parameters and the resulting diameters are summarized in Table 3-3. A *p*:*s* ratio of 12.5 is used and resulted in patterning the first and second sheet only with a maximum aspect ratio of 1:6 but with a significant difference between the top and bottom diameter. The laser power was not enough to pattern the third sheet. Using higher *p*:*s* ratios results in patterning all three sheets. A *p*:*s* ratio of 25 results in obtaining an aspect ratio of up to 1:6.8 in the third sheet with improved top and bottom diameters variations, but with curvy sidewalls. The second sheet though that has an aspect ratio of 1:3.9 has good characteristics and can be used to fabricate nanocomposite cilia with such dimensions. Using a *p*:*s* ratio of 37.5 improved the pattern in the third sheet and resulted in an aspect ratio of 1:5.7 with straighter sidewall and reduced top and bottom diameters variation compared to the other tested *p:s* ratios. The fourth *p*:*s* ratio was set to be 50 which resulted in widening the pores, and the aspect ratio can be up to 1:4.5. In general, the PMMA sheets that are not directly exposed to the laser beam are less affected by the low-intensity tails of the Gaussian distributed laser, and hence, preferred to fabricate artificial cilia with straight sidewalls.

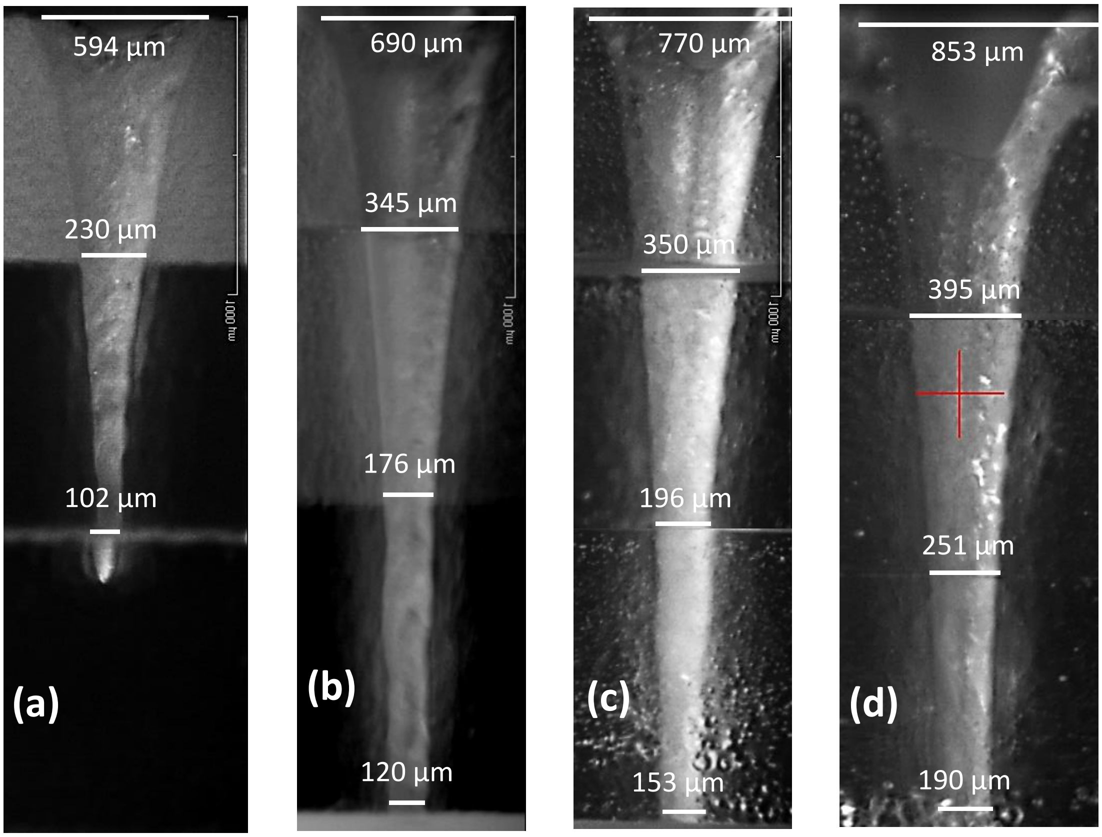

Figure 3-21: Microscope images of triple laser patterned PMMA sheets with: (a) $p=25\%$ / $s=2\%$, (b) $p=50\%$ / $s=2\%$, (c) $p=75\%$ / $s=2\%$, (d) $p=100\%$ / $s=2\%$.

***p*:*s* , (*p*%, *s*%)**	**Top *(Exposed to laser)* d_{avg}, d_{top}, d_{bottom}**	**Middle d_{avg}, d_{top}, d_{bottom}**	**Bottom d_{avg}, d_{top}, d_{bottom}**
12.5, 25, 2	412 µm, 594 µm, 230 µm	166 µm, 230 µm, 102 µm	NA
25, 50, 2	517 µm, 690 µm, 345 µm	260 µm, 345 µm, 176 µm	148 µm, 176 µm, 120 µm
37.5, 75, 2	560 µm, 770 µm, 350 µm	273 µm, 350 µm, 196 µm	174 µm, 196 µm, 153 µm
50, 100, 2	624 µm, 853 µm, 395 µm	323 µm, 395 µm, 251 µm	220 µm, 251 µm, 190 µm

Table 3-3: Parameters used to fabricate different triple stack PMMA molds and the resulting pores diameters.

In the multi-stack technique, using the middle patterned sheet of the triple stack was optimum for straight sidewalls with relatively high aspect ratio, and low top-to-bottom diameters variation. The bottom sheet in the multi-stack, if processed carefully, can lead to high aspect ratio and reduced top-to-bottom diameters variation. Depending on the required dimension, the laser patterning parameters can be modified, and the thickness of the mold can be selected. An example of the prepared PMMA mold and the resulting nanocomposite cilia are shown Figure 3-22.

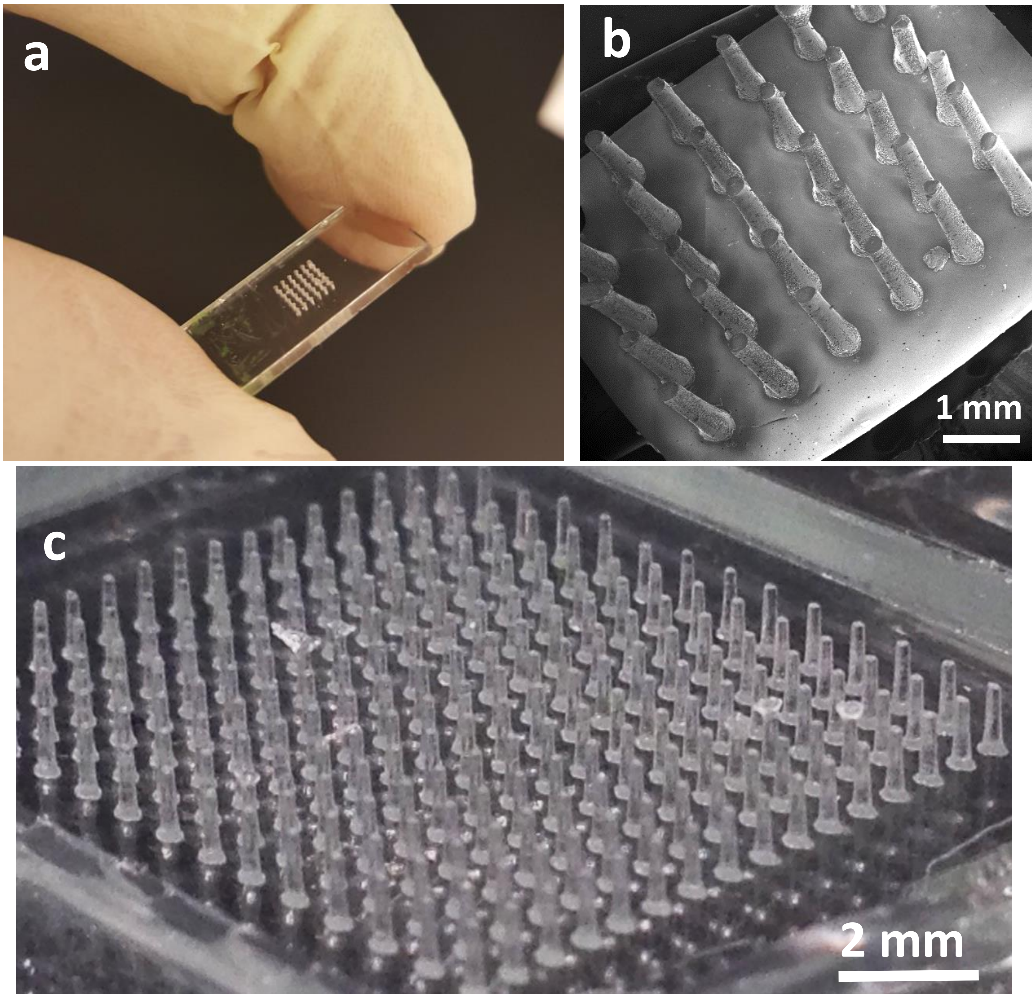

Figure 3-22: (a) Optical image for the fabricated PMMA mold, and (b) SEM image for the resulting cilia. (c) Optical image of large cilia array: 1 cm^2 area with 224 cilia, each is 200 µm in diameter and 1 mm long.

3.5.3 Silicon Mold

Despite the high cost of preparing a silicon mold, it was required to fabricate ultra-sensitive miniaturized cilia with patterns smaller than the laser beam utilized in the PMMA mold process. Smaller cilia diameters were fabricated using a silicon mold prepared by a conventional lithography process to pattern a 400 nm Cr layer used as a hard mask, followed by deep reactive ion etching (DRIE) to etch through the silicon wafer and form micro pores with the desired diameters, and heights up to 500 µm. Different DRIE processes are available to obtain anisotropic fluorine-based silicon etching. The utilized DRIE process is called “Bosch process” that is considered as the most popular method. It consists of alternating steps of etching and sidewall passivation (Figure 3-23) and was developed by Robert Bosch GmbH [123]. DRIE was performed in an Oxford Instruments (PlasmaLab 100) at a temperature of -20 ºC and sequential SF_6 etching steps of 7 seconds and C_4F_8 passivation steps of 5 seconds. The passivation step deposits a hydrophobic fluoropolymer coating that protects against sidewall erosion as etching goes deeper into the silicon wafer. The conditions for the deposition cycle are: C_4F_8 (100 sccm) and SF_6 (5 sccm) gas flow at 30 mTorr. Plasma is generated by a table power of 5 W and coil power of 1300 W. The etch cycle plasma is generated by a table power of 30 W and C_4F_8 (5 sccm) and SF_6 (100 sccm) gas flow with the other process conditions similar to the deposition cycle. A total of 1400 cycles is performed in order to etch through the silicon wafer and form a mold for 500 µm long and 100 µm in diameter cilia. The etched through Si mold is shown in Figure 3-24. This etching process also allows preparing molds for high aspect ratio cilia with lengths shorter than 500 µm by partially etching the silicon to the required depth. Cilia array of 10 µm in diameter and 50 µm in length were fabricated as shown in Figure 3-25.

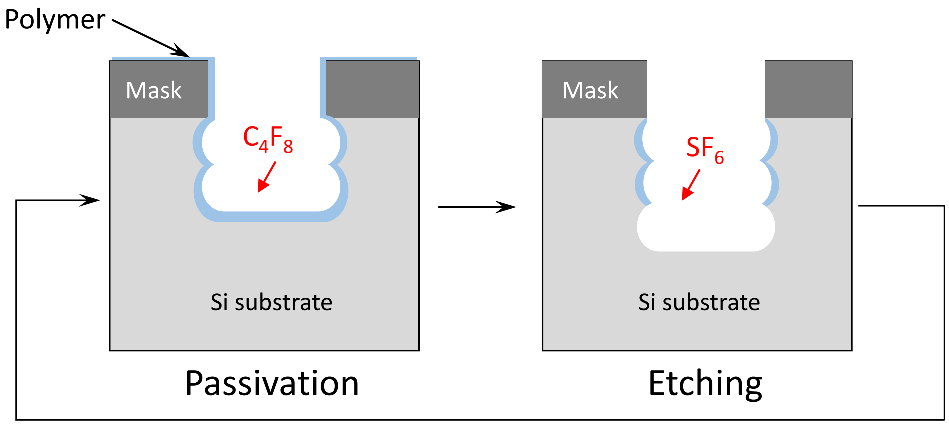

Figure 3-23: Schematic illustration of the Bosch process. The deposition of a passivation layer protects the sidewalls during the subsequent etching cycle.

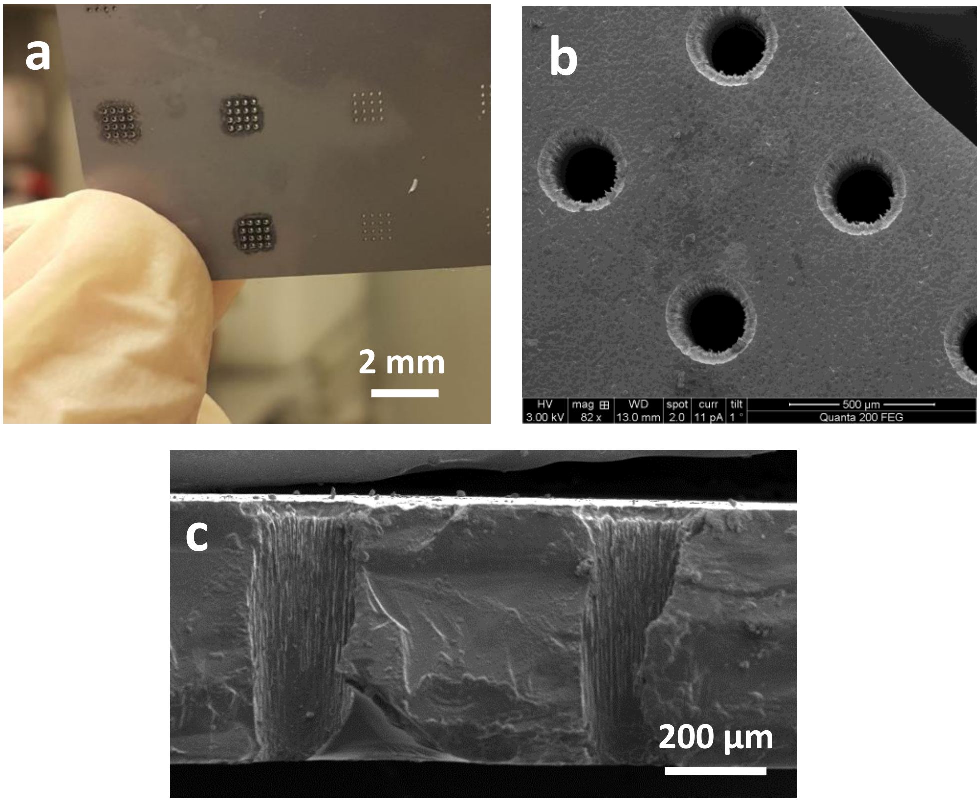

Figure 3-24: (a) Fabricated Si mold with pores diameter of 150 µm and 500 µm long. (b) SEM image of the holes in the Si mold, and (c) a cross section image showing the pores' inside morphology.

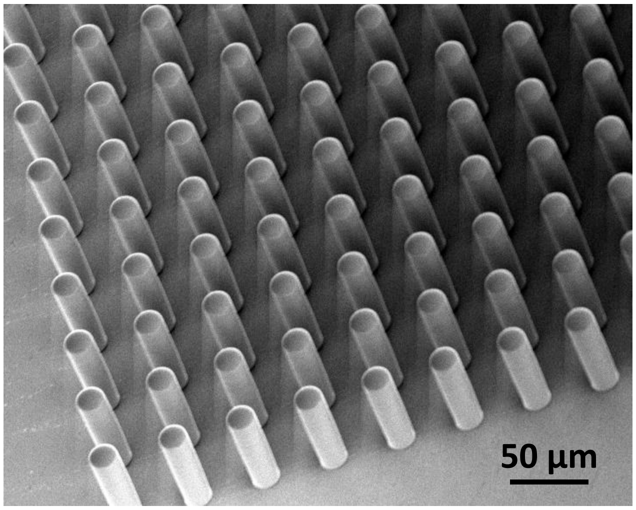

Figure 3-25: 10 μm in diameter and 50 μm in length cilia fabricated using silicon mold.

After preparing the silicon mold, a silanization step was conducted where the surface of the mold was passivated in order to reduce the adhesion between PDMS and silicon by forming covalent bonds (Si–O–Si) with PDMS [124]. The silicon mold was treated under vacuum with vapors from a fluorinated Silane agent to deposit a non-sticking layer on the mold [124, 125]. The mold was then ready to be used for nanocomposite cilia fabrication.

3.6 Magnetic Hysteresis of Nanocomposite Cilia

The permanent magnetic properties of the nanocomposite and the anisotropy directions due to NWs alignment were studied by obtaining the hysteresis loops of the samples. A tool for magnetic characterization and hysteresis measurement is the vibrating sample magnetometer (VSM). The VSM, invented in 1956 by Simon Foner, is an induction magnetometry measurement approach [126]. It utilizes Faraday's induction law to measure the magnetic moment of a physically vibrating specimen inside a uniform magnetic field. The technique is described by Maxwell equation:

$$\nabla \times \vec{E}_e = \frac{\partial}{\partial t}\vec{B} \qquad \text{3-11}$$

where $\vec{E}_e$ is the electric field and $\vec{B}$ is the magnetic flux. When the magnetic sample vibrates and causes a change of the magnetic flux, a voltage is induced in a detection coil in close proximity to the sample that is proportional to the rate of change in magnetic induction. The induced voltage is sinusoidal when the vibration is sinusoidal, and it is proportional to the magnetic moment of the sample and the vibration frequency. The magnetic properties of a sample can be studied by measuring the induced voltage, which is proportional to the magnetization and orientation of the sample.

In a typical VSM system (Figure 3-26), a lock-in amplifier is used to measure the induced AC voltage taking the sample's vibration source as its reference signal. Detection coils are used to measure the difference in magnetic inductions and minimize the influence of other magnetic sources. Simultaneous measurements are taken for both the sample magnetization and the applied uniform magnetic field in order to obtain the hysteresis loops.

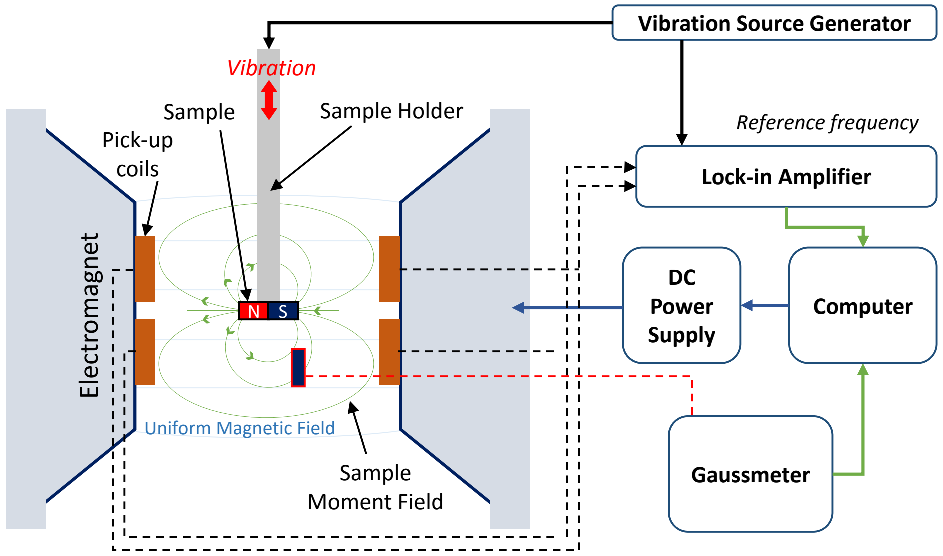

Figure 3-26: Schematic of the working principle of a vibrating sample magnetometer.

VSM measurements of NWs and nanocomposite cilia were carried out using MicroMag 3900 system. The system can produce up to a maximum DC magnetic field of 2 T with a sensitivity of 100×10^{-9} emu. In order to measure the magnetic properties of nanocomposite cilia with and without NWs alignment, the hysteresis loops along the cilia and perpendicular to the cilia direction were obtained using the VSM. Depending on the alignment of the Fe NWs in the nanocomposite, the cilia can have different remanence to saturation magnetization (*Mr/Ms*), and anisotropic properties can be obtained. Nanocomposite cilia with randomly aligned NWs have similar magnetization curves in the vertical and horizontal directions as shown in the normalized loops in Figure 3-27(a). The cilia have a remanence to saturation magnetization ratio of 0.7 with a coercivity of 1.5 kOe. The similarity of the magnetization curves in the vertical and horizontal directions indicates that the NWs are not aligned in a specific direction in the composite, with the vertical direction being slightly preferred. As shown in Figure 3-27(b), normalized magnetization loops for nanocomposite cilia with NWs aligned along the length of the cilia show a magnetic anisotropy. A remanence to saturation magnetization ratio *Mr/Ms* of 0.95 along the vertical direction with a coercivity of 1.8 kOe, and 0.37 along the horizontal direction with a coercivity of 1.4 kOe. Ideally, *Mr/Ms* would be equal to 1 along the vertical direction for aligned NWs, however, the magnetostatic dipole interaction between the NWs cause a high demagnetization field that slightly reduces the nanocomposite remanent magnetization as discussed in section 3.2.2.

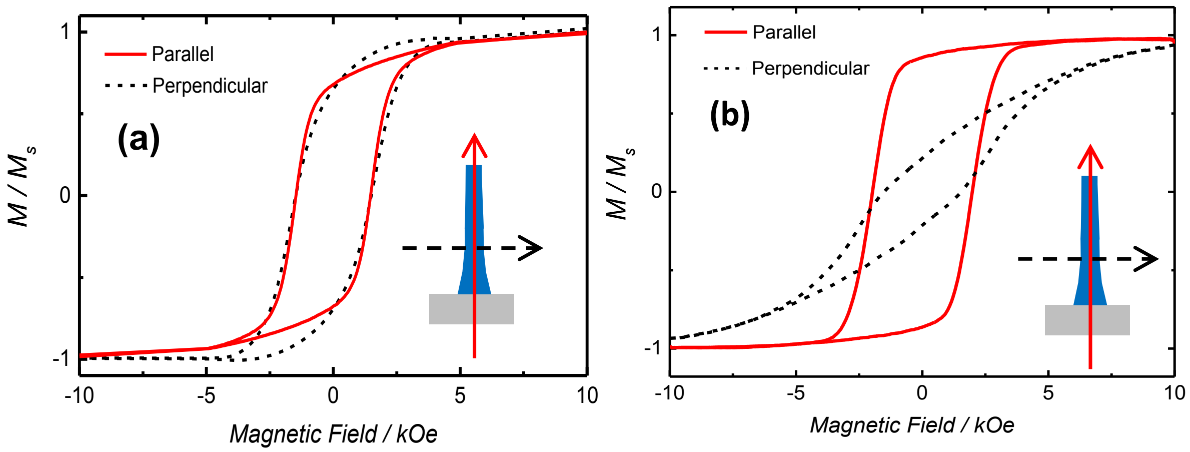

Figure 3-27: Normalized magnetization *M* to Saturation magnetization *Ms* as a function of the applied field *H* of magnetic cilia obtained with the VSM in the parallel and perpendicular direction of the cilia with (a) randomly aligned, and (b) vertically aligned NWs.

3.7 Structural Characterizations

3.7.1 Nanowires distribution in the nanocomposite

When moving toward device miniaturization, the processing of nanocomposites with dispersed NWs in a matrix becomes a challenge. The distribution of NWs must be homogeneous in the polymer and agglomerates must be avoided to maintain homogenous magnetic and mechanical material properties. Several factors influence the agglomeration but a prominent factor for the agglomeration of ferromagnetic NWs in nanocomposites is the attractive magnetic forces due to the high remanent magnetization. A demagnetization process is a typical solution for ferromagnetic materials before preparing the nanocomposite. However, this factor is difficult to eliminate for NWs since they cannot be demagnetized due to the high shape anisotropy. Another reason for agglomeration is the stiction of NWs due to the high surface area to volume ratio, [127] which can be minimized by using different approaches proposed previously for nanoparticles such as functionalizing the particles' surface with emulsifiers or the encapsulation with polymeric coatings [128, 129].

A series of steps was conducted during the fabrication process to reduce the agglomeration in the nanocomposite. Dispersing the NWs in SDS surfactant prior to mixing with PDMS results in reducing agglomeration. Vortexing and shaking the nanocomposite before curing as discussed earlier helps the reduction of agglomeration. An important feature of PDMS is the high viscosity that causes large friction for the NWs movement toward each other, and hence making them more separated and relatively difficult to agglomerate.

The distribution of NWs in the nanocomposite with 14% concentration were studied by horizontal cross section imaging with TEM. The nanocomposite samples were frozen with liquid nitrogen and then sliced into thin horizontal samples in order to use them for imaging. Figure 3-28(a) shows a cross section image of a nanocomposite with random NWs, while Figure 3-28(b) shows a nanocomposite with vertically aligned NWs. The results reveal that the prepared nanocomposites have relatively uniform distribution. Figure 3-28(c) shows a 3D reconstruction of TEM images of a nanocomposite with aligned NWs across 10 μm. It can be seen clearly that the NWs alignment together with a high degree of uniformity has been successfully achieved.

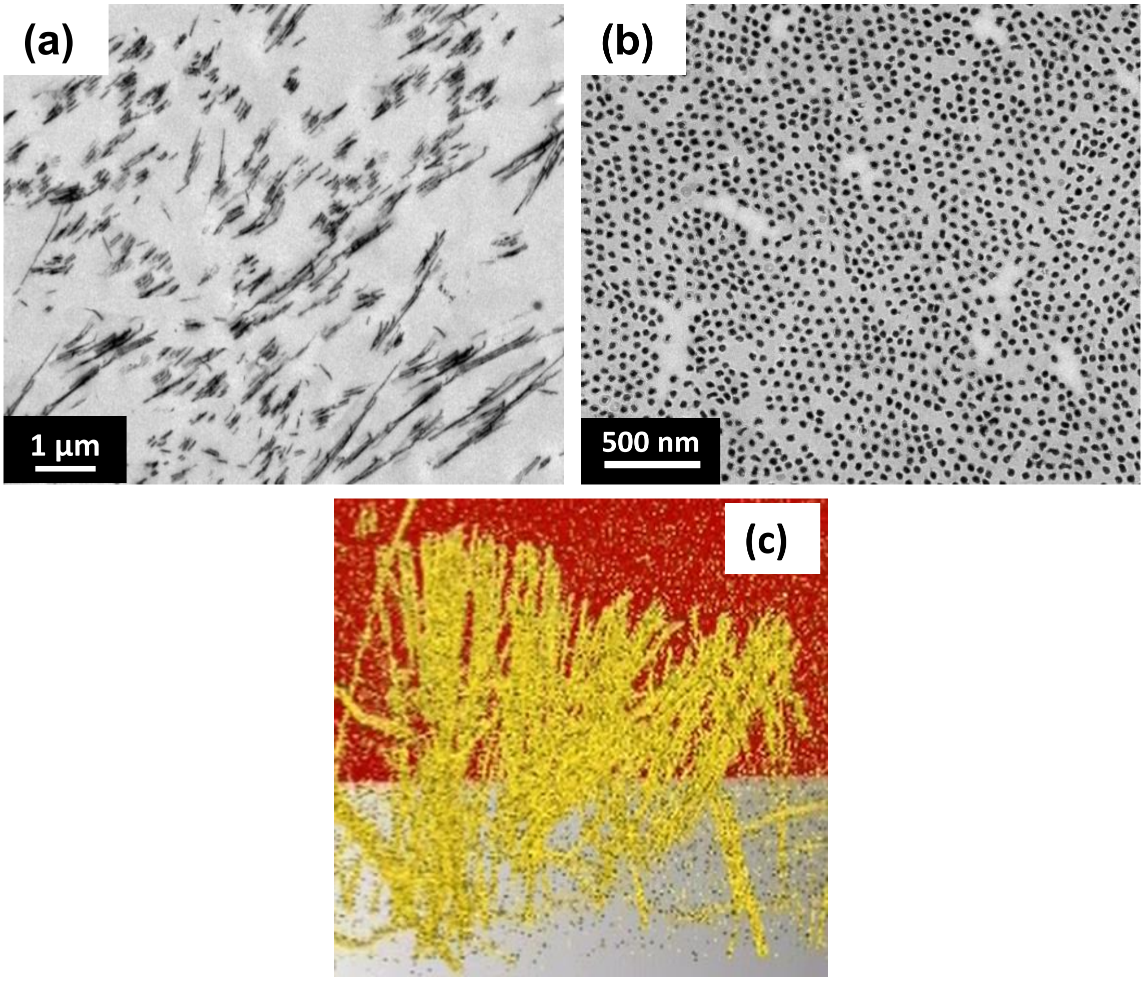

Figure 3-28: Cross section image of a NW-PDMS nanocomposite produced by transmission electron microscopy for randomly aligned NWs (a) and vertically aligned NWs (b) with 14% NWs to PDMS volume ratio. (c) 3D reconstruction of multiple TEM images across 10 µm thickness of a nanocomposite sample with aligned NWs.

3.7.2 Nanocomposite Young's Modulus Study

Since obtaining high elasticity of the nanocomposite cilia is crucial to increase the sensitivity of the sensor, a study is carried out to investigate the effect of adding NWs to PDMS on the elasticity. The modulus of elasticity of a material (also referred as Young's modulus (*E*) after the British scientist Thomas Young) is defined as the ratio between stress and strain as shown in equation 3-12 [130]. Stress is defined as force (*F*) per unit area (*A*), and typically tensile stress is used for this study, while strain is defined as the deformation of a material (the ratio of deformation (*Δl*) to the initial length (*l*)). The Young's modulus can be obtained mathematically as the slope of the stress-strain curve when the material is deformed elastically. Stiffer materials have higher elastic modulus than softer materials; hence, a low elastic modulus is desired for the cilia sensor.

$$E = \frac{stress}{strain} = \frac{F/A}{\Delta l/l} \qquad 3\text{-}12$$

PDMS has been previously reported to have Young’s modulus values ranging from less than 0.1 MPa to 3.8 MPa, depending on the amount of the cross-linker in the PDMS solution, or the curing temperature [22, 131, 132].

In this dissertation, the Young’s modulus of the nanocomposite cilia was obtained by measuring stress and strain experimentally. Pure PDMS cilia and nanocomposite cilia prepared under different conditions are fixed between a bottom holder plate and the moveable head of an INSTRON 5966 extensometer (tensile/compressive force testing system) as shown in Figure 3-29. The system can precisely determine the exerted force and the vertical displacement. The resolution depends on the sample dimensions and the utilized load cell. By using a 10 N load cell and three cilia that are 1 mm long and 200 μm in diameter, a tensile force resolution of 5 mN and vertical displacement of 16 μm can be measured. The extensometer was calibrated after mounting the cilia and then tensile forces are applied to the cilia until achieving a strain of 1.3 (130% stretching). The Young’s modulus was calculated as the ratio between stress and strain (slope) in the elastic (linear) region.

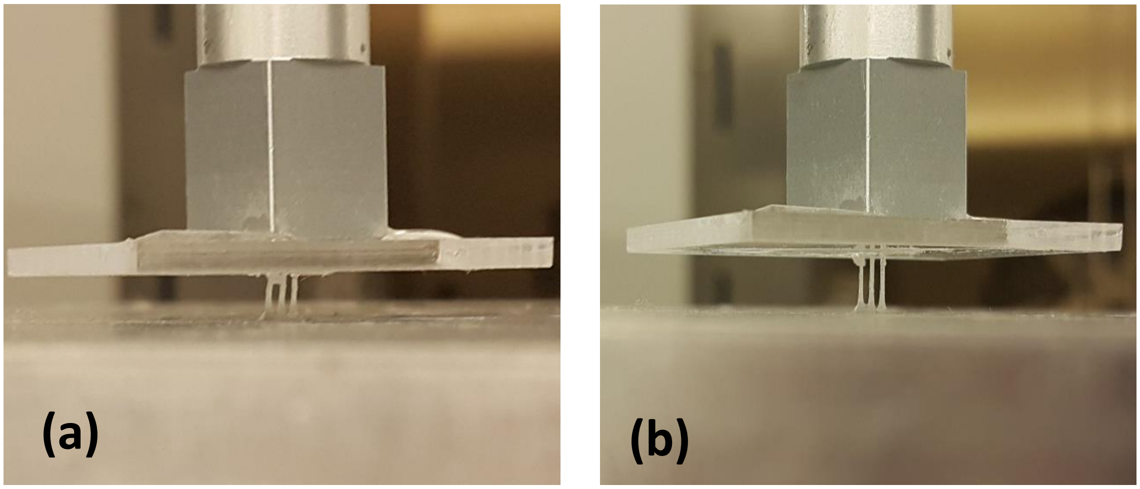

Figure 3-29: Test setup of the stress-strain experiment to study nanocomposite elasticity showing (a) cilia in their initial state and (b) after 100% stretch (strain=1).

The elasticity of nanocomposite cilia with 14% NWs to PDMS volume ratio was studied and compared to pure PDMS cilia. The cilia were prepared from 10:1 PDMS solution to cross-linker ratio and cured at 90 ^{o}C for one hour. As shown in Figure 3-30, nanocomposite cilia have an elastic linear region between 0-0.9 strain values resulting in a Young's modulus of 0.76 MPa. Beyond 0.9 strain, the nanocomposite is deformed and the stress-strain relation is not linear. Compared to pure PDMS cilia that has a Young's modulus of 0.71 MPa and a deformation of around 1.2 strain, it was observed that incorporating NWs in the nanocomposite cilia does not have a significant effect on the rigidity of the cilia, and the advantage of the high elasticity of the PDMS was maintained. Another experiment was conducted for nanocomposites prepared from 10:1 PDMS solution to cross-linker ratio and cured for one hour at different curing temperatures between 70 ^{o}C and 200 ^{o}C. The Young's modulus increases from 0.45 MPa to 1.06 MPa as the curing temperature is increased as illustrated in Table 3-4.

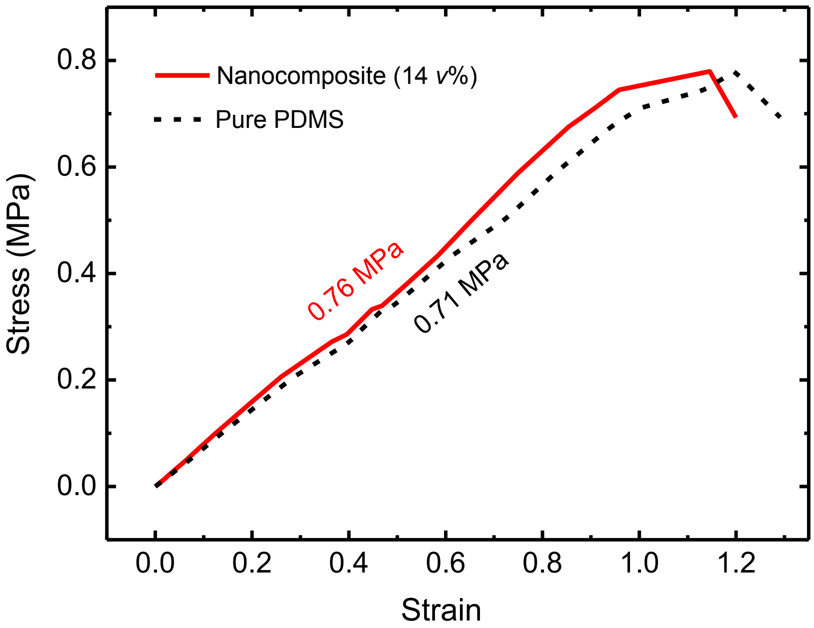

Figure 3-30: Experimental results for pure PDMS cilia, and nanocomposite cilia fabricated at 90 ^{o}C for 1 hour.

Curing Temperature (^{o}C)	Young's Modulus (MPa)
70	0.45
90	0.76
150	0.82
200	1.06

Table 3-4: Young's modulus comparison for nanocomposite cilia prepared from 10:1 PDMS to cross-linker ratio, and with 14% NWs volume ratio. Samples are cured for one hour at different temperatures.

3.8 Simulation of the Cilia's Stray Magnetic Field

The stray field of the permanent magnetic nanocomposite cilia was modeled by finite element simulations using the commercial software (COMSOL). A 3D cylindrical beam was designed in order to study the stray magnetic field component affecting the GMI sensor. The change in magnetic field affecting the GMI sensors upon the cilia deflection was quantified to understand the operation of the cilia sensor. The magnetic NWs were accounted for by assigning magnetization vectors to the cilia, which were calculated from the NWs' remanence magnetization obtained experimentally as described in section 3.2.3 and the amount of NWs in the cilia with considering the alignment direction of the NWs. Cilia with vertically aligned, and random Fe NWs were investigated. For simplicity, cilia bending was simulated by rotating the beam about the anchor point by the angle *θ,* which is related to the deflection *δ* by:

$$\delta = l \cdot \sin(\theta) \qquad \text{3-13}$$

The average value of the magnetic field *H* at the GMI sensor is:

$$H(\theta) = \frac{1}{n}\sum_{i=1}^{n}(H_x)_i \qquad \text{3-14}$$

where H_x is the component of the magnetic vector field along the GMI sensor's sensitive direction, *i* is the summation index and *n* is the number of magnetic vectors used in the averaging process. The average magnitude of the magnetic field H_{mag} is calculated as:

$$H_{mag}(\theta) = \frac{1}{n}\sum_{i=1}^{n}\left(\sqrt{H_x^{\,2}}\right)_i \qquad \text{3-15}$$

One case study was simulated to study the stray field variation upon cilia deflection for the flow sensor discussed in section 4.2. 500 µm long and 100 µm in diameter cilia with 14% NWs to PDMS volume ratio were designed. To represent the cilia sensor design, the stray field components affecting the magnetic sensor layer that has a width equivalent to the diameter of the cilia, and a length in the x-axis equivalent to twice the length of cilia was studied. The simulated cilia were placed in the middle of the GMI sensor layer to obtain the average change of magnetic field around the cilia. When the cilia are straight they result in an average magnetic vector field of 0 Oe due to the symmetry of the stray field. However, the magnitude of the magnetic field in this case is 3.2 Oe, which can be utilized as the bias field of the GMI sensor. As the cilia deflect, the stray field at the GMI sensor increases on one side of the cilia and decreases on the other side, causing the average magnetic field value to increase. When the cilia are fully deflected, the magnetic field reaches an average value of 1.3 Oe. This field value can be detected easily with the GMI sensor and lies within the linear and high sensitivity region (discussed in section 3.10.3).

3.9 Harsh Environment Applications

3.9.1 Corrosion Study

Polycrystalline Fe NWs were used as the nanocomposite fillers. The corrosion of bare polycrystalline Fe NWs was studied by oxidizing NWs dispersed on a TEM grid and annealed at 150 ^{o}C. The evolution of the oxide shell around the NWs with the oxidation process was observed using TEM. Figure 3-31a shows a TEM image that confirms that the fabricated NWs are polycrystalline Fe with grain size in the range of tens of nanometers. The SAED pattern, shown in the inset, identify the *bcc* phase of Fe. By oxidizing the NWs in the oven over time, it can be noticed that a decrease of the Fe core's diameter occurs with an increase in the oxide shell thickness. After 20 minutes annealing, a 7 nm Fe_3O_4 (magnetite) shell was formed with *fcc* phase around the Fe *bcc* phase as revealed by the SAED pattern (Figure 3-31b). The Fe_3O_4 shell was formed by oxygen diffusion between the grain boundaries of Fe NWs (which was enhanced by the annealing process). After 24 hours of oxidation, a fully polycrystalline Fe_3O_4 structure was obtained (Figure 3-31c). Although oxidation at room temperature does not occur as fast as the forced oxidation process in this experiment, it was noticed that full NWs oxidation can occur which is a critical problem that results in losing the high magnetization property of Fe, and forming multi-domains which lead to losing the stray field of the NWs. This will significantly degrade the sensor's performance.

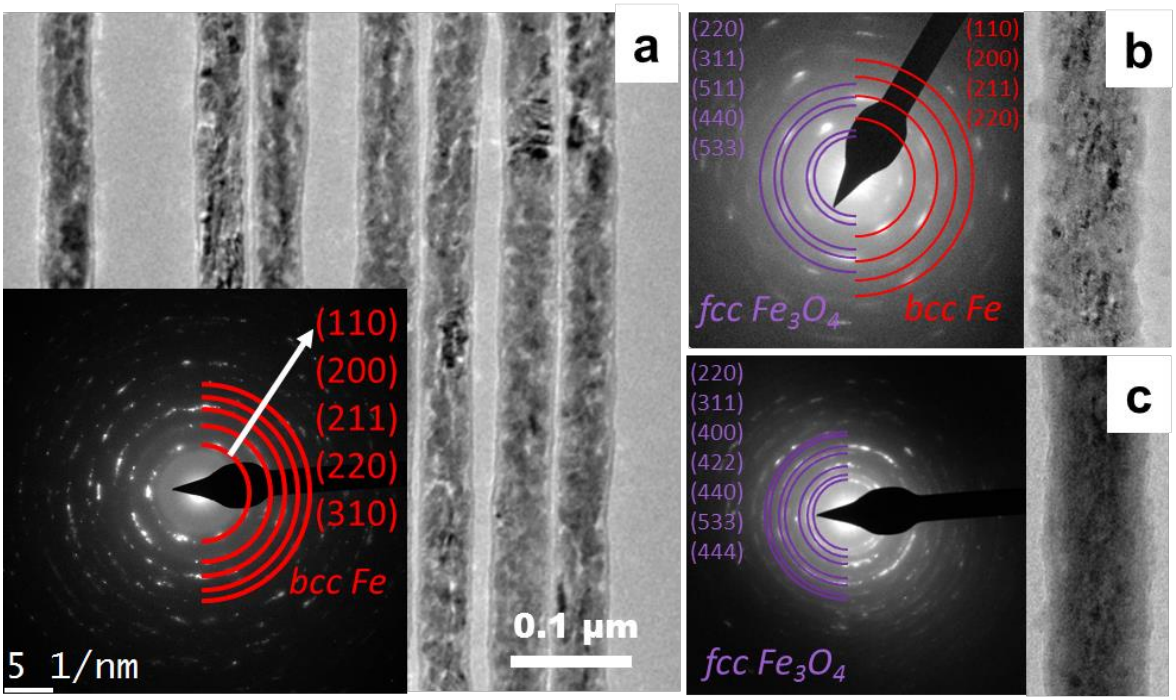

Figure 3-31: (a) Bright field transmission electron microscopy image and selected area diffraction pattern of polycrystalline Fe NWs. (b) Fe-Fe_3O_4 core-shell NWs after 20 minutes of annealing at 150 ^oC. (c) Fe_3O_4 NWs after 24 hours of annealing.

A previous study has discussed the fabrication of 40 nm in diameter single crystalline Fe NWs that are more difficult to oxidize [133]. This is due to the pronounced difference in crystallinity from the ones of polycrystalline NWs. Single crystals of *bcc* structure with a size in the micrometer range were obtained and the single crystal phase is confirmed by SAED. The results show that single crystal NWs oxidize much slower than polycrystalline NWs and even after 24 hours annealing only 10 nm magnetite shell was formed. The later was the maximum shell thickness could be obtained. After 72 hours of annealing time it remained unchanged. This is attributed to the absence of grain boundaries that are required for the oxygen diffusion oxidation process. The resistance to complete oxidization of the single crystal NWs is a great advantage for applications like the proposed sensor in this dissertation and also for applications that require high temperature operation, while maintaining the magnetic properties of NWs. However, a major drawback that prevented using single crystal NWs in this dissertation is the very small fabrication yield. The fabrication process of single crystal NWs fails frequently and it was difficult to produce longer NWs than 1 μm. The ability to fabricate polycrystalline NWs efficiently, and being convinced that PDMS can protect NWs in the nanocomposite from oxidation, polycrystalline NWs were selected in this dissertation. One of the main advantages of the proposed nanocomposite, was the protection of NWs from oxidation when exposed to a humid environment. Initially, an X-Ray Diffraction (XRD) experiment was carried out to investigate the possibility of forming magnetite shell around the polycrystalline Fe NWs during the fabrication of the nanocomposite. XRD is a well-known non-destructive crystallography technique to characterize the atomic structure of materials. In this work, Bruker D8 Discover high-resolution X-ray diffractometer system was utilized to determine the NWs material and the crystal structure using X-ray radiation with a wavelength of 1.5406 Å. XRD analysis in Figure 3-32 reveals that the NWs in the nanocomposite are polycrystalline Fe with a thin shell of magnetite (Fe_3O_4) around the NWs.

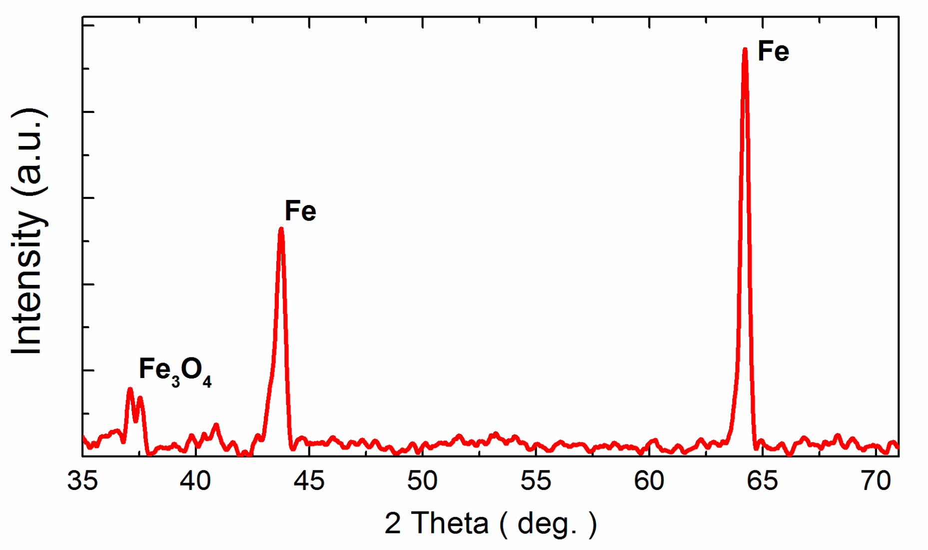

Figure 3-32: X-ray diffraction results for Fe NWs.

To study the level of protection for NWs in nanocomposites at room temperature, the remanent magnetizations of a nanocomposite sample exposed to air and another sample kept in water were measured over a period of 60 days (Figure 3-33). The remanence magnetization was measured regularly using VSM in the 60 days period. It was found that the magnetization slightly drops over time with a reducing rate. The sample exposed to air keeps 81% of the initial magnetization while the sample kept in water keeps 76% of the initial magnetization. NWs inside the nanocomposite oxidize due to the fact that PDMS is permeable to water molecules allowing minor interaction between Fe and oxygen. This explains the higher magnetization reduction rate for the sample kept in water. Figure 3-33 also shows the remanent magnetizations of fully oxidized iron NWs that were oxidized by placing them in an oven for 24 hours at 150 ^{o}C. These NWs oxidized forming magnetite as mentioned earlier. The magnetization of magnetite NWs was found to be 40% of that of Fe NWs. This value is higher than the

30% reported in literature [1], which is attributed to the initial thin oxide layer around the NWs at the beginning of the experiment. Comparing the oxidization rate of the nanocomposites to bare Fe NWs, the latter oxidize with a much higher rate. After 10 days, the remanent magnetization of the bare NWs in air drops to 85% of the initial magnetization compared to the 98% and 92.5% of nanocomposite exposed to air and water, respectively. It can be said that oxidation starts to saturate after several days because the formed Fe_3O_4 shell acts as a passivation layer that prevents further oxidation in the normal conditions (e.g. room temperature).

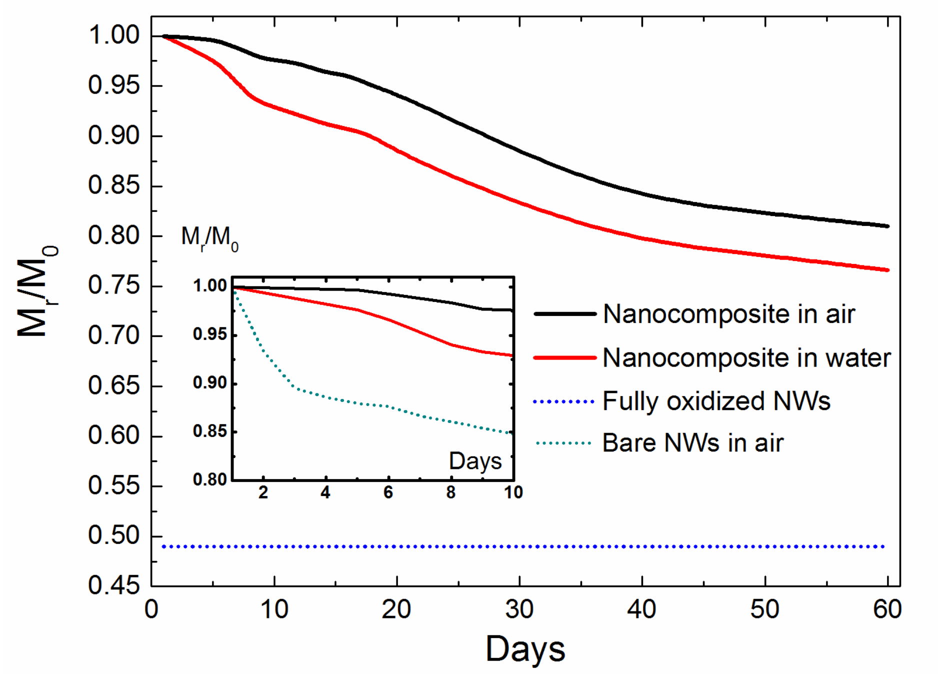

Figure 3-33: Remanence magnetization *Mr* to initial remanence magnetization M_0 of nanocomposite pillars kept in air and water and of fully oxidized Fe NWs. Inset: Comparison between nanocomposites and bare Fe NWs.

3.9.2 High Temperature Operation

As discussed in 3.2.2, NWs exhibit very promising magnetic properties, suggesting that they could be used as permanent magnets that can operate at high temperatures. Through their strong shape anisotropy, NWs keep exhibit a large temperature independent coercivity when operating below the Curie temperature, which is 770 °C for Fe [1, 134]. Hence, the high magnetization of Fe can be utilized while remaining below the Curie temperature. On the other hand, polycrystalline NWs have been shown to be prone to corrosion (section 3.9.1). In order to elucidate the thermal stability of the nanocomposite, where the NWs are protected by the polymer, we conducted a temperature dependent study of the magnetization. In order to test the thermal stability of the nanocomposite, the nanocomposite magnetic properties variation is tested with the increase in temperature. The hysteresis loops of a 1 mm long and 200 μm in diameter cilia are obtained at a temperature range between 27°C to 290°C using superconducting quantum interference device (SQUID) VSM (1500-100 Quantum design Inc.). The cilia are heated in a vacuum oven during the magnetization measurement, and the hysteresis loops are obtained for each temperature value. Within this temperature range, the permanent magnetic behavior of the nanocomposite is maintained, as shown in Figure 3-34, where only a slight magnetization reduction is observed as a result of Curie‘s law. The nanocomposite is then cooled down to 27 °C, and the magnetization loop is measured again revealing a reduction in the remanence magnetization Mr of 16% (compared to the initial remanence magnetization, Mr_0, at 27 °C) with an increase in coercivity compared to the initial state. The reduction in remanence can be caused by trapped water molecules in the PDMS that resulted in slightly oxidizing the NWs in the nanocomposite with the heat-assisted oxygen diffusion process, forming a thin shell of magnetite around the NWs. The magnetite shell reduces the diameter of the Fe core in the NWs, increasing its coercivity, due to the increased aspect ratio.

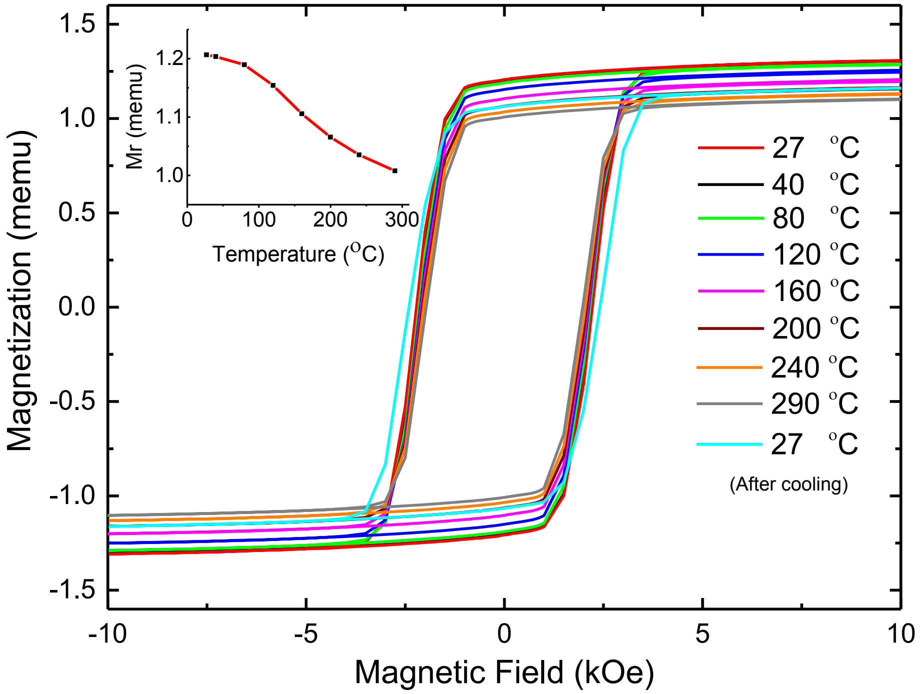

Figure 3-34: Magnetization loops of nanocomposite cilia at different temperatures from 27°C to 290°C. **Inset**: remanence magnetization reduction with the increase in temperature.

Looking at the mechanical stability of cured nanocomposites operated at high temperatures, it can be said that the nanocomposite is mechanically stable up to the curing temperature but undergoes a small reduction in elasticity, which slightly hardens the nanocomposite and increases the Young's modulus as discussed in 3.7.2. This can have direct effect on the sensitivity and operating range of the developed cilia sensor. Previous studies have shown that the mechanical properties are maintained at low heating temperatures. Operating at temperatures greater than 200 °C will reduce the mechanical strength due to the thermal decomposition of PDMS that starts at about 200 °C and peaks at around 310 °C [135].

3.10 Magnetic Sensor Selection

3.10.1 Introduction to Giant Magneto-impedance Sensors

A giant magneto-impedance (GMI) thin film magnetic field sensor is utilized which was chosen for its high sensitivity and potential for wireless operation [136-138]. GMI sensors are very sensitive magnetic field sensors that utilize the GMI effect. This effect is observed as a large variation in the real and imaginary parts of the complex impedance of the sensor under alternating current operation when exposed to an external magnetic field. This effect is mainly caused by the variation of the skin depth due to the strong dependence of the skin effect on the magnetic permeability. The skin depth δ_m can be expressed as:

$$\delta_m = \sqrt{\frac{2\rho_r}{\omega\mu}}, \qquad \text{3-16}$$

where ρ_r is the resistivity, ω is the angular frequency and μ is the permeability of the magnetic material. To enhance the sensitivity, a magnetic easy axis can be induced in the transverse direction of the GMI sensor, creating a magnetically sensitive axis in the longitudinal direction. When an external magnetic field is applied in the longitudinal direction, a change in the anisotropy through the domain wall movement and magnetization rotation is observed which consequently, changes the permeability. This change, in turn, causes the change of the skin depth, which in the end changes the impedance of the sensor. Besides their easy fabrication process, room temperature operation [139, 140], and the potential of wireless operation, GMI sensors have shown remarkable sensitivity to small magnetic fields down to pico-Tesla regime, which is at least one order of magnitude higher than typical GMR sensors [141-145].

Magnetic layers with high magnetic permeability, well defined magnetic anisotropy and small coercivity are the prerequisite conditions for obtaining a strong magnetoimpedance effect [136]. The geometry of GMI sensors has an important role in enhancing the performance. It has been shown previously that multi-layer structures composed of two soft and highly permeable ferromagnetic materials with a conductive layer (e.g.: Cu) have lower DC resistance, and can enhance the GMI effect. In multi-layered structures, a significant change in the impedance is observed due to the increase in the inductive reactance of the ferromagnetic layers, which is greater than the resistance of the conductive layer. The resistivity difference is an important parameter that allows achieving a high impedance ratio where the current gets concentrated inside the conductor generating a transverse magnetic flux B_t (Figure 3-35), which magnetizes the ferromagnetic films and a large skin effect is obtained.

Upon the application of an external magnetic field along the long direction (sensitive axis), the ferromagnetic films are magnetized along that direction resulting in an increase in the transverse permeability, which increases the impedance, until the external magnetic field reaches a saturation value equal to the anisotropy field of the ferromagnetic films. As the external magnetic field increases further, the permeability drops and the contribution of rotational magnetization dominates. The decreasing rate of the permeability reduces as magnetization rotation dominates the process.

Tri-layer GMI sensors that utilize Permalloy ($Ni_{80}Fe_{20}$) have been introduced and optimized previously [138, 146, 147]. Permalloy, in particular, was found to be favorable due to the low magnetoelastic coefficient providing good control of the magnetic anisotropy and increase the mechanical reliability if exposed to external stress.

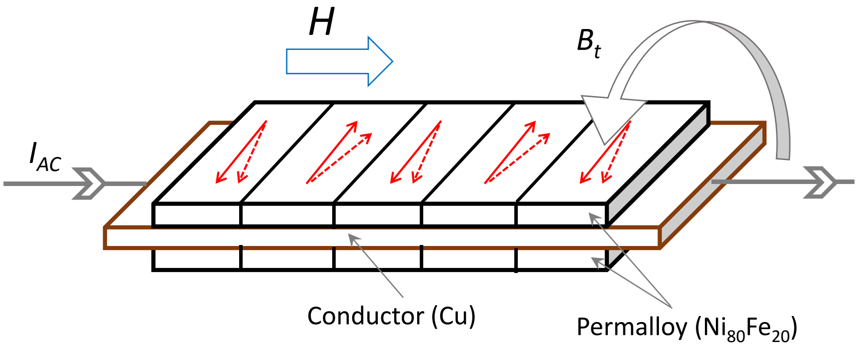

Figure 3-35: Illustration of the GMI sensor structure. The arrows in the sensor indicates the magnetization of individual magnetic domains. When applying an external magnetic field *H*, magnetization rotation occurs along the magnetic field direction.

3.10.2 Magnetic Sensor Fabrication

The GMI sensor is composed of $Ni_{80}Fe_{20}/Cu/Ni_{80}Fe_{20}$ and can be deposited onto a rigid glass substrate or Si substrates with 500 nm SiO_2, or on a flexible Kapton substrate. The tri-layer thin-film structure was patterned using standard lithography and lift-off process. AZ9260 photoresist was spun in 3 steps to ensure uniform dispersion: 200 rpm at 150 rpm/s for 3 seconds, 1500 rpm at 1000 rpm/s for 3 seconds, and then 2400 rpm at 1500 rpm/s for 60 seconds. The photoresist was then cured at 110 ˚C for 180 seconds. This process results in a 10 µm thick film. Patterning the GMI sensor design was done by exposing the photoresist with an exposure dose of 1500 mJ/cm^2 using a standard chrome-on-glass mask and contact aligner (EVG 6200). The exposed photoresist was then developed for 8 minutes using AZ726 developer. After washing the sample with DI water and drying it, the GMI sensor stack was deposited by electron-beam evaporation (Denton, Explorer 30) which is ideal for the lift-off process due to the low incident angle. Electron-beam evaporation uses a source material placed in a crucible and heated through a filament above its sublimation temperature and evaporated to deposit a film on the surface opposite to the evaporated atoms. Deposition with electron-beam evaporation with high energy results in higher density film with good adhesion to the substrate. The electron beam is focused on the source material using bending magnets, and the beam is swept across the source material to heat the material uniformly. The thicknesses of the $Ni_{80}Fe_{20}/Cu/Ni_{80}Fe_{20}$ were 100 nm/ 200 nm/100 nm, respectively. The deposition of the stack was conducted at room temperature using multiple crucibles in the chamber to allow deposition without breaking the vacuum. The chamber pressure was set at 9×10^{-6} Torr, and the deposition rates are found to be 2 Å/s for the Permalloy and 4 Å/s for Cu. The deposition was conducted using a customized substrate holder providing a 200 Oe directional magnetic field applied parallel to the surface of the sample and generated using a C-shaped permanent magnet mounted on the holder (Figure 3-36a). The sample can be aligned to control the direction of the applied field which is chosen to be along the short dimension of the patterned sample to induce the film transverse anisotropy, creating a magnetically sensitive axis in the longitudinal direction. The sample was then placed in Acetone for 20 minutes with gentle agitation to dissolve the photoresist with the magnetic stack on top, while keeping the patterned GMI sensor stack on the substrate.

To investigate the magnetic domain patterns of fabricated GMI sensors, the top magnetic layer was observed using magneto-optic Kerr effect microscope (evico Magnetics), a technique that describes the changes to light reflected from a magnetized surface. The magnetic domains in (Figure 3-36c) show the induced transverse anisotropy of a 200 μm wide GMI sensor.

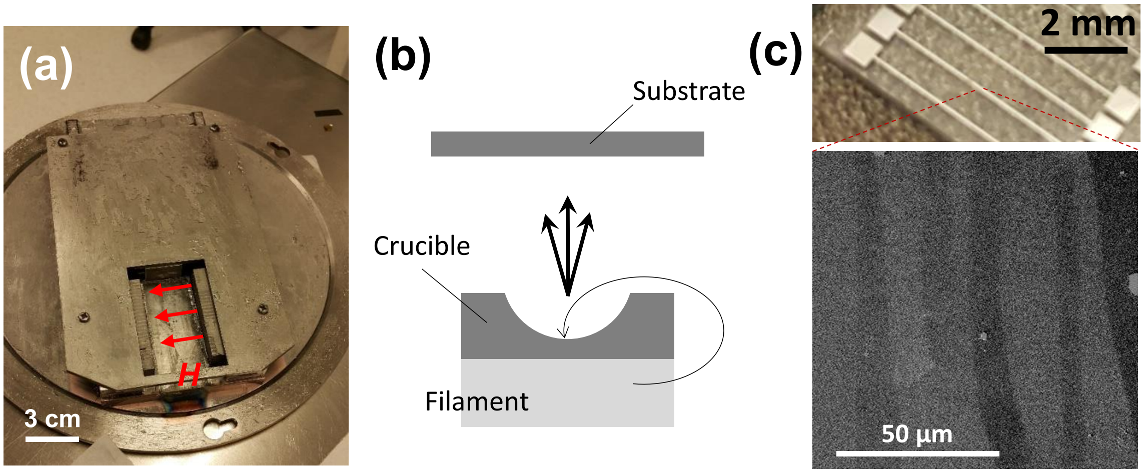

Figure 3-36: (a) Sample holder with a c-shaped permanent magnet is used to introduce the transverse anisotropy in the Permalloy film. The magnetic field direction (*H*) is shown. (b) Mechanism of electron-beam evaporation system used for the thin film deposition. (c) Domain pattern of the top magnetic layer of a 200 µm wide GMI sensor strip, showing transverse anisotropy.

3.10.3 Magnetic Sensor Characterization

The GMI sensors were characterized by measuring the impedance response at different frequencies upon the application of an external magnetic field to obtain the sensitivity, the characteristics of the response and the optimum operating range. The external magnetic field was applied using a Helmholtz coil powered with a DC power supply (Agilent E3646A) and the applied magnetic field value at the sensor position was measured using a magnetometer (FW Bell 6010). Magnetic field values from 0 Oe to 100 Oe with increments of 1 Oe are applied to the GMI sensor. Three techniques were used to obtain the complex impedance of the GMI sensor using: an impedance analyzer or a network analyzer.

The first technique to obtain the impedance of the GMI sensor was by using an impedance analyzer (Agilent E4991A) at currents ranging from 0.1 - 2 mA in amplitude, and a frequency range between 10 to 500 MHz. This method is straightforward and does not require circuitry, but it has several limitations such as the incapability to obtain the exact impedance of the GMI sensor only without the extra wiring. Connecting the sensor at a distance from the impedance analyzer is required to test the cilia sensor for the different applications.

The second method to obtain the impedance of the sensor utilizes a network analyzer (Agilent E5061B) to measure the complex reflection coefficient (S11). The sensor testing setup and the electrical model are shown in (Figure 3-37). A 20 mm×20 mm board was used to test the GMI sensor with two 50 Ω microstrip transmission lines that are 15 mm long and 1 mm wide are patterned on a Roger 4533 double-sided copper laminate substrate with a thickness of 1 mm. The top electrode is used for the microstrip lines and the bottom layer was used as a ground plane underneath. The GMI sensor was placed in between the microstrip lines and wire-bonded to the microstrip lines as shown in Figure 3-37. The sample board was terminated from one side by a 50 Ω load with an SMA connector. The other side of the board was connected to the network analyzer through an SMA port for the impedance measurement. The network analyzer was adjusted to have 0 dBm output power and a frequency sweep from 10 MHz to 1 GHz, and calibrated for open, short, and 50 Ω load at the end of the shielded SMA Cable. The reflection coefficients at the measurement plane Γ_{MP} (that includes all the components at the fixture), and at the sample plane Γ_{SP} were obtained. A computational model was used (3-17) to correlate Γ_{MP} with Γ_{SP} to consider the phase shift and the losses on the microstrip line as reported successfully in [147, 148].

$$\Gamma_{MP} = \Gamma_{SP} \exp(-2\gamma_p l_t) \qquad \text{3-17}$$

Where l_t is the length of the microstrip line, and $\gamma_p = \alpha + j\beta$ is the propagation constant that can be obtained by measuring the fixture in open configuration. The impedance Z can be determined by:

$$Z = Z_0 \frac{1+\Gamma_{SP}}{1-\Gamma_{SP}} - Z_L \tag{3-18}$$

Where Z_0 is the characteristics impedance, and Z_L is the 50 Ω termination load. By obtaining the complex impedance at the frequency spectrum, the GMI sensor can be precisely characterized.

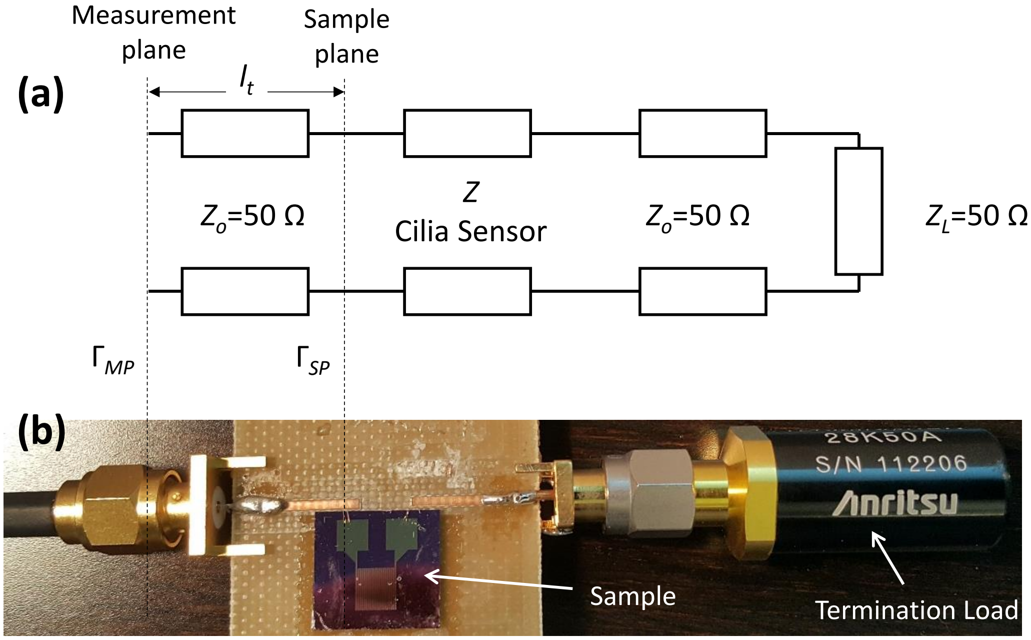

Figure 3-37: (a) Electrical model for the complex reflection coefficient (S11) measurement method. (b) Image of the sample board and the terminating load.

The third method for measuring the response of the GMI sensor was designed for real-time detection and dynamic experiments. The GMI sensor was designed in a voltage divider configuration with a 100 Ω high-frequency surface mount resistor (Anaren

250375-4Y100-2) as shown in the electrical model in Figure 3-38 and the output voltage V_{GMI} as shown in equation 3-19. An RF waveform generator (Agilent E8257D) was used to power the sensor with a sinusoidal signal of 50 mV amplitude and the required frequency. The sensor real-time impedance amplitude was measured using a real-time spectrum analyzer (Tek RSA 6100A).

$$V_{GMI} = \frac{V_{IN} Z_{GMI}}{R + Z_{GMI}} \tag{3-19}$$

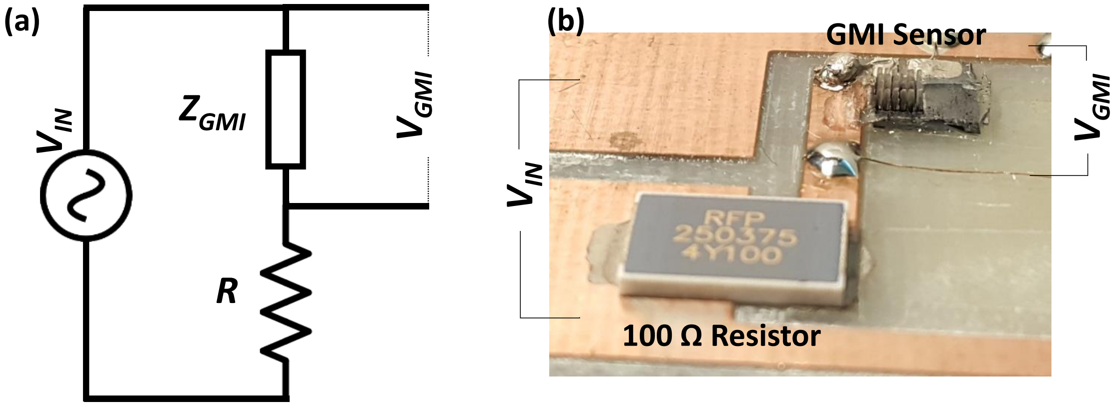

Figure 3-38: (a) Electrical model of the real-time measurement of the GMI sensor. (b) Image of the used circuit,

4 APPLICATIONS OF BIOINSPIRED NANOCOMPOSITE CILIA SENSORS

4.1 Cilia Tactile Sensor: Toward the Development of Artificial Skins

4.1.1 Introduction

The evolution in areas like robotics is demanding an increased perception of the environment such as touch, vibration, and flow sensing. Noticeable progress in the field of artificial skins lead to the development of different technologies that can mimic the complex sense of touch in humans for better interaction with the surrounding environment. These skins are also important for applications like wearable consumer electronics or health monitoring systems [42, 44, 45, 149-152], smart surgical tools [55], or to provide the sensitivity missing in prosthetics to enable people with artificial arms or legs to “feel” the world around them again [153]. Tactile sensors are the essential components for artificial skins. Different physical principles have been exploited for the development of highly sensitive and low power tactile sensors realized on flexible substrates allowing conformal coverage of electronic systems on non-planar surfaces, and hence enabling new functionalities [150, 154]. Several examples of different tactile sensing technologies have been discussed in section 2.4, showing the rapid development in this field. However, many challenges still exist in combining high resolution sensing with low power consumption while maintaining multi-functionality.

4.1.2 Sensor Design

Highly elastic and permanent magnetic nanocomposite cilia were integrated on a GMI sensor as a novel tactile sensing approach as described in section 3.1 (Figure 4-1). The

NWs-PDMS nanocomposite serves as the structural material for the cilia and is prepared by incorporating 6 µm long and 35 nm in diameter Fe NWs into PDMS. Fe NWs are chosen for their high magnetization at remanence and high coercivity, making them nano-permanent magnets, as described in section 3.2.2. The cilia are integrated on GMI sensors fabricated on silicon or Kapton substrates for rigid or flexible tactile sensors, respectively. The GMI sensor is patterned as mentioned in section 3.10.2 to a meander shape of a total area of 4 mm^2 composed of 2 mm long and 200 µm wide conductors with 200 µm spacing. Each GMI sensor represents one sensing element or sensing pixel. Sensing elements can be connected to form arrays, providing information about the distribution, direction or stability of the applied force.

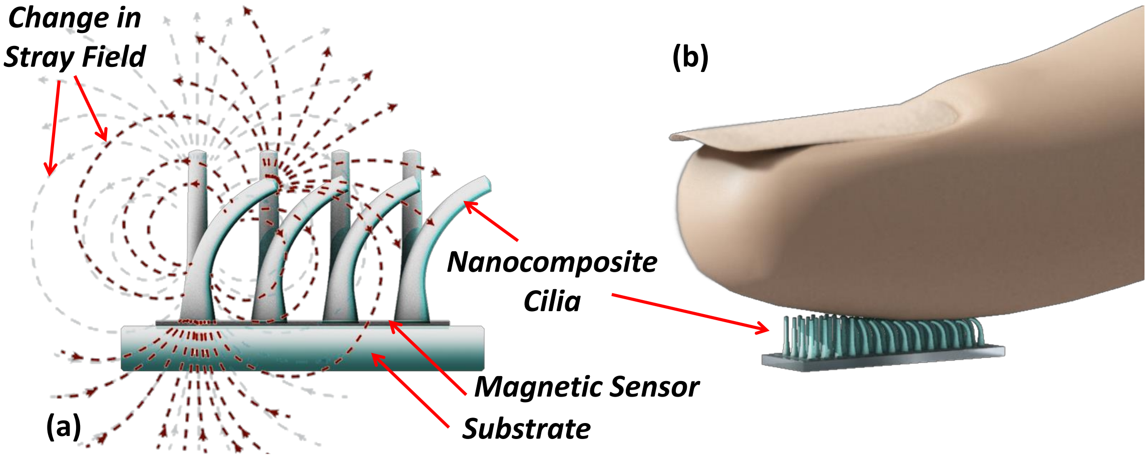

Figure 4-1: (a) Illustration of the tactile sensor working principle. In the standing position, the cilia’s stray magnetic field affects the magnetic sensor and biases it to an initial value. In the presence of an external force, the cilia bend and the stray field measured with the magnetic sensor changes, resulting in a change in the impedance. (b) Example of the cilia deflection mechanism when touched with a finger.

The nanocomposite has a maximum of 14% NWs/PDMS volume ratio as studied in section 3.7, which is chosen to provide the biasing field for the GMI sensor while not adversely affecting the polymerization of the PDMS or the elasticity of the cilia.

Nanocomposite cilia with diameters from 20 µm to 200 µm are fabricated using the master mold techniques mentioned in section 3.5. Cilia with diameters greater than 100 µm are fabricated using the PMMA master mold, while smaller cilia diameters are fabricated using the silicon mold. The nanocomposite cilia were cured with NWs aligned along the length direction.

4.1.3 Sensor Characterization, Experiments and Results

In order to characterize the GMI sensor as discussed in section 3.10.3, a magnetic field is applied using a Helmholtz coil, while the impedance is obtained from the complex reflection coefficient measured with a network analyzer (Agilent E5061B) at a frequency of 500 MHz. A highly sensitive region is observed between 2.5 Oe to 8 Oe with an impedance peak obtained at a field of 9 Oe corresponding to the anisotropy field of the $Ni_{80}Fe_{20}$ thin films (Figure 4-2). The stray field of the nanocomposite cilia provides a bias field of about 3.2 Oe at which the GMI sensor has a sensitivity of 1.2 Ω/Oe.

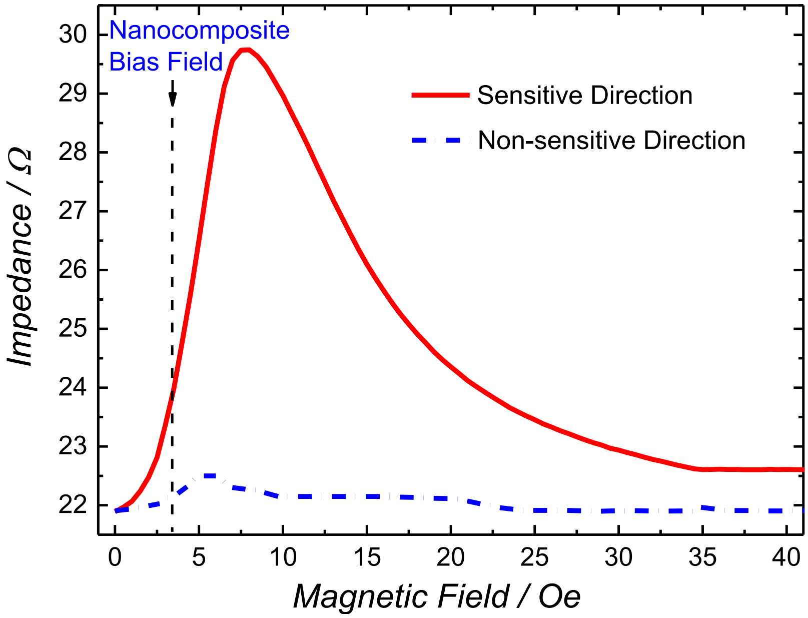

Figure 4-2: Impedance response of the GMI sensor to an external magnetic field applied at 500 MHz operating frequency.

The performance of the tactile sensor is investigated using different cilia geometries on 2×2 mm^2 magnetic sensors to obtain results in different pressure regimes with tailored values of sensitivity, resolution, and operating range. Figure 4-3 shows a tactile sensor with 1 mm long and 200 µm in diameter cilia arrays with 9 and 24 cilia.

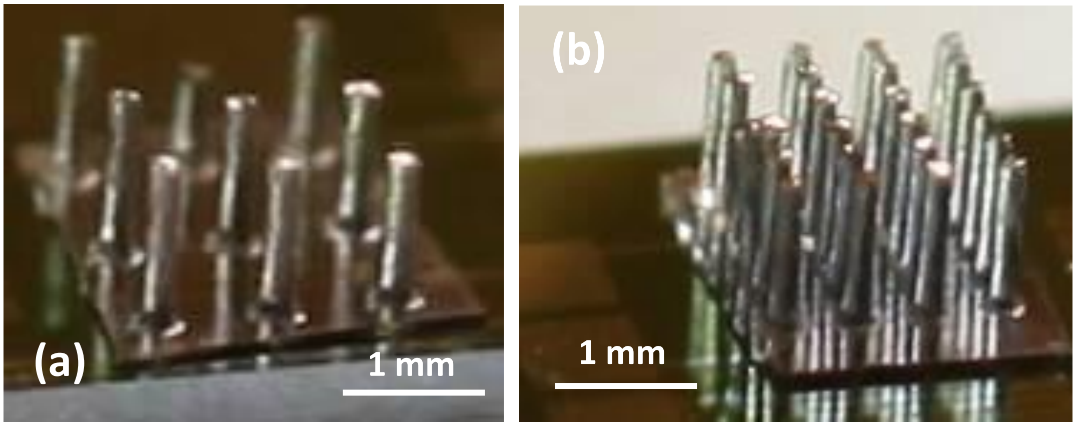

Figure 4-3: Arrays of (a) 9 and (b) 24 artificial cilia.

The sensor is characterized by applying vertical forces using a computer controlled extensometer tensile/compressive force testing system (INSTRON 5966) with 10 N load cell. The impedance response is obtained using a network analyzer similar to the GMI sensor characterization setup in section 3.10.3. The test setup is shown in Figure 4-4.

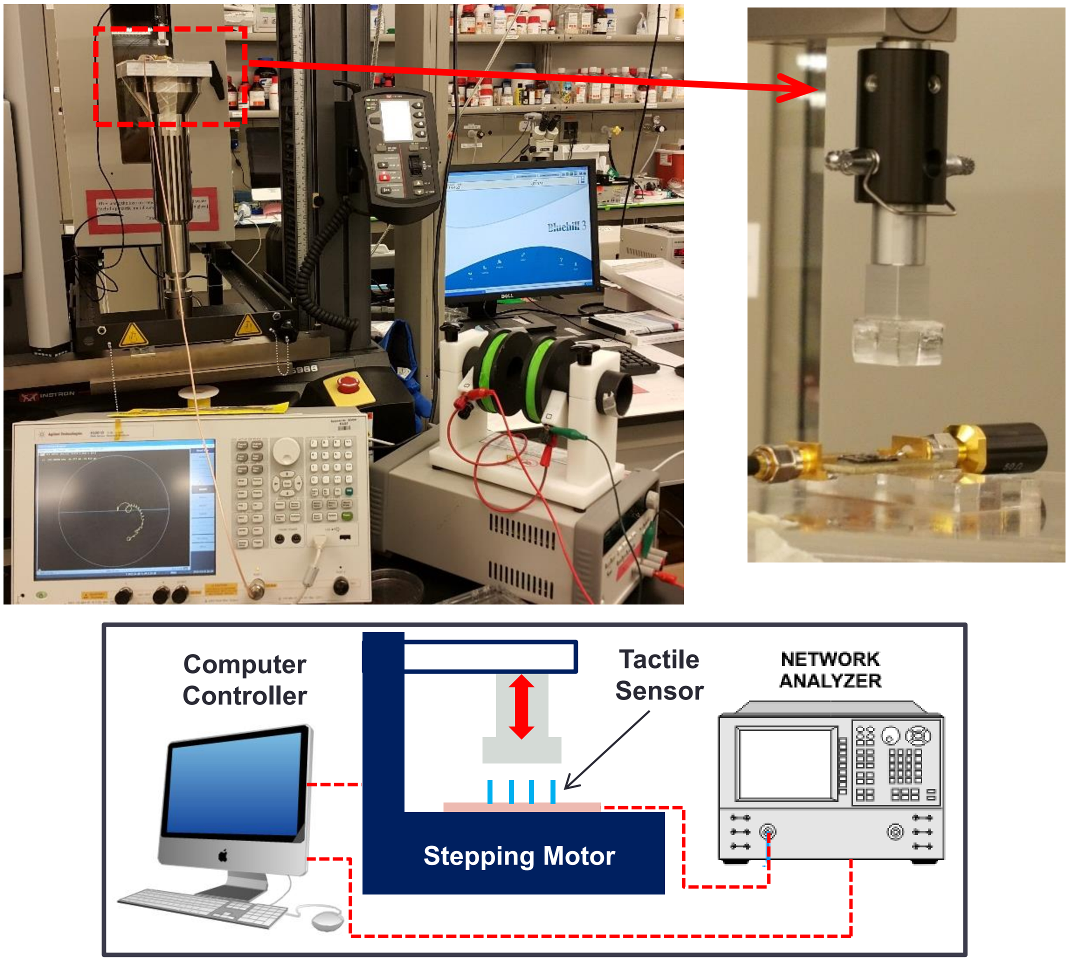

Figure 4-4: Tactile sensor test set-up.

As shown in Figure 4-5, the sensor with 9 cilia can detect vertical forces up to 200 mN (50 kPa) with a high resolution of 0.9 mN (0.23 kPa) and a sensitivity of 15 mΩ/mN (60 mΩ/kPa). Thereby, the sensor operates at an extremely low power consumption of 80 nW. The maximum impedance change of the sensor is about 0.8 Ω when fully deflecting the cilia. The 24 cilia arrangement tactile sensor shows a response in a larger range up to 680 mN (170 kPa) with a resolution of 3.5 mN (0.88 kPa) and a sensitivity of 4 mΩ/mN (16 mΩ/kPa). A higher saturation impedance change of 0.86 Ω is observed due to the presence of a larger volume of magnetic NWs affecting the GMI sensor.

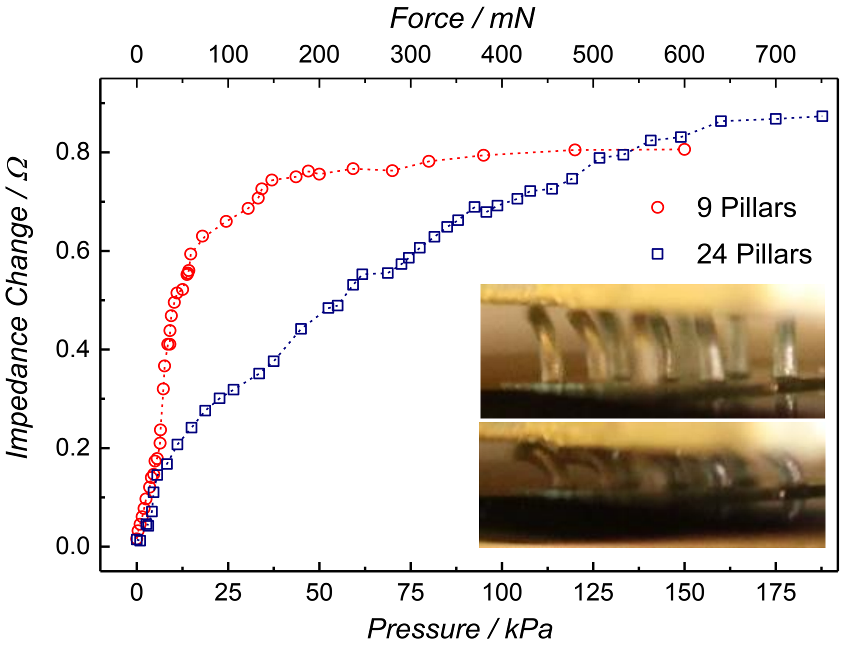

Figure 4-5: Tactile sensor impedance response for two cilia configurations: 9 and 24 cilia array. Inset: Deflection mechanism of cilia sensor with a vertical force.

The capability of the sensor to detect the texture of objects is verified by moving a PMMA object that contains 200 μm deep grooves with widths of 2 mm and 4 mm horizontally across the cilia sensors with a speed of 0.4 mm/s. The sensor is operated at 500 MHz and the signal is measured using a real-time spectrum analyzer (Tek RSA 6100A). As shown in Figure 4-6, the sensor signal closely follows the pattern of the textured object with 255 μV change of the voltage amplitude between the high and low features of the moving object.

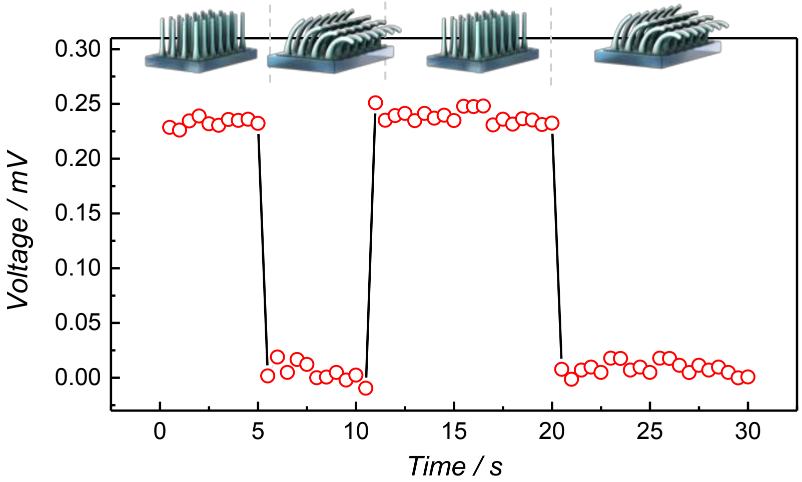

Figure 4-6: Dynamic response for texture measurement.

To achieve the human skin's capability to "feel" irritants (such as the effects of a fly landing) [44], sensors for a low-pressure regime are required. To this end, an array of 2500 smaller cilia each with 10 µm diameter and 50 µm length is fabricated and realized on the GMI sensor. The sensor is tested by applying vertical forces up to 3.5 mN (0.85 kPa) (Figure 4-7). A maximum impedance change of 0.4 Ω is observed with a sensitivity of 214 mΩ/mN (856 mΩ/kPa) and an ultra-high resolution of 0.065 mN (16 Pa).

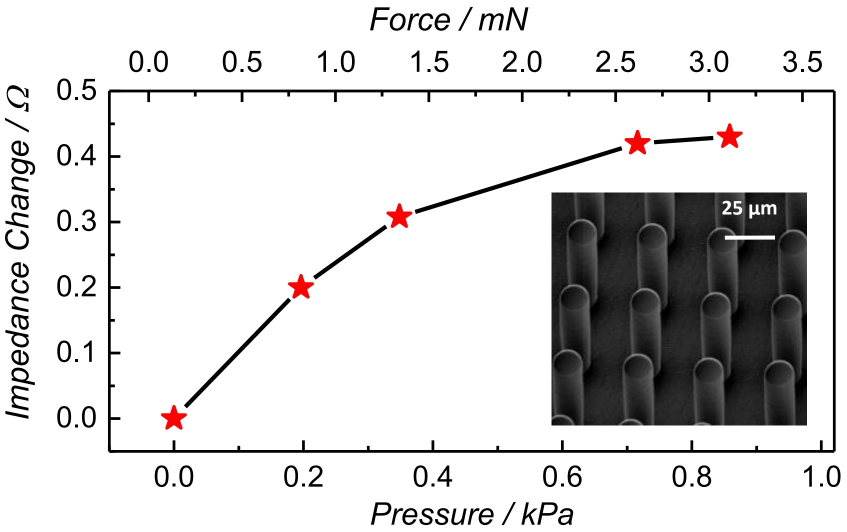

Figure 4-7: Force response of a sensor with 2500 cilia with 10 µm in diameter, 50 µm long, and 25 µm separation. **Inset**: SEM image of the fabricated cilia array.

The tactile nanocomposite cilia sensor concept can also be realized on flexible substrates. We used Kapton for this purpose and fabricated the 4 mm^2 meander shape GMI sensor and 24 nanocomposite cilia with 1 mm in length and 200 µm in diameter on top of it. GMI sensors maintain their high sensitivity when fabricated on Kapton and only show a shift of the peak value related to a change of the anisotropy field [147]. A real-time measurement similar to the textured object detection experiment is conducted using a flexible sensor placed directly above the artery of the wrist. With the cilia in contact with the skin, mechanical plethysmography is realized, enabling the detection of the heart rate [155]. As shown in Figure 4-8, a heart rate of 85 beats min^{-1} is found from the signal peaks of about 100 uV caused by the blood pressure waves.

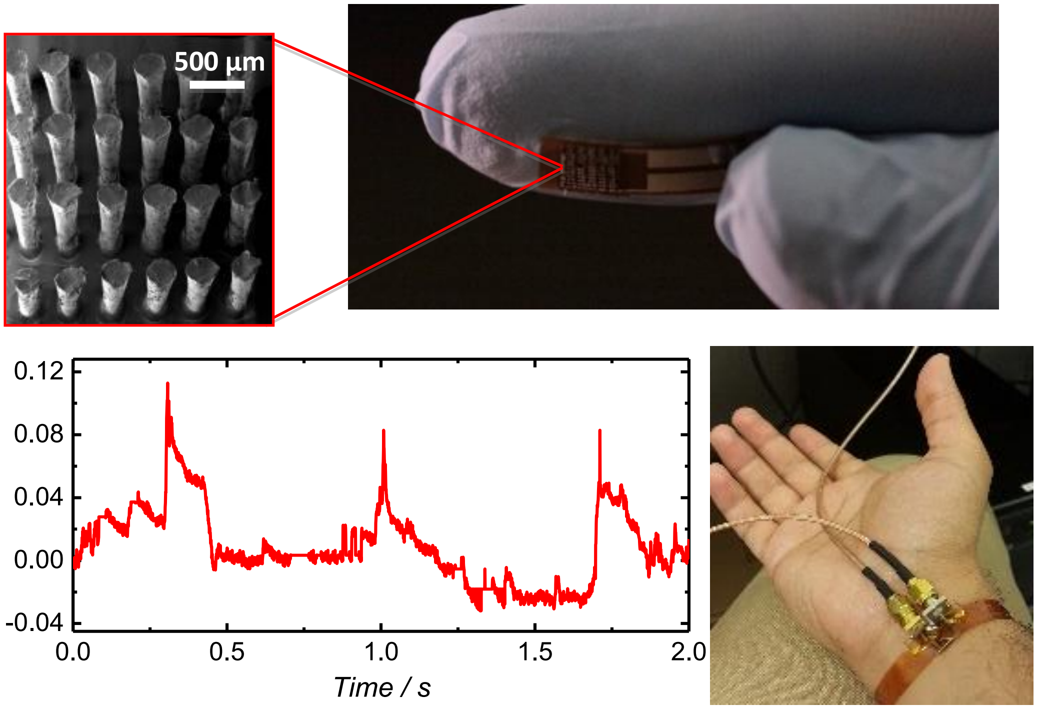

Figure 4-8: (a) A photograph of a flexible tactile sensor with an inset showing an SEM image of the cilia, and a photograph showing the flexible sensor attached to the skin above the artery of the wrist. (b) Measurement of the heart rate (85 beats min^{-1}) through the signal caused by the blood pressure waves, which cause bending of the cilia.

The versatility of our sensor concept enables operation not only in air but also in liquids without modifications. This is demonstrated in Figure 4-9a, which shows the response of a tactile sensor with 24 cilia tested in air and water. A distinct feature of the cilia tactile sensor is its ability to measure shear forces as arising from fluid flow. To this end, the sensors have been implemented in a microfluidic channel using 500 μm long cilia with different aspect ratios as discussed in section 4.2.5 [66]. In the case of water flow, sensors with 100 μm diameter cilia operate up to 7.8 mm/s (0-15 kPa) with a maximum sensitivity and resolution of 0.9 Ω/(mm/s) and 15 μm/s, respectively. Increasing the diameter of the cilia to 250 μm increases the operating range to 10 mm/s (0-20 kPa) with a maximum sensitivity and resolution of 0.17 Ω/(mm/s) and 79 μm/s, respectively (Figure 4-9b). It is worth noting that the sensor operates at extremely low power consumption of about 80 nW.

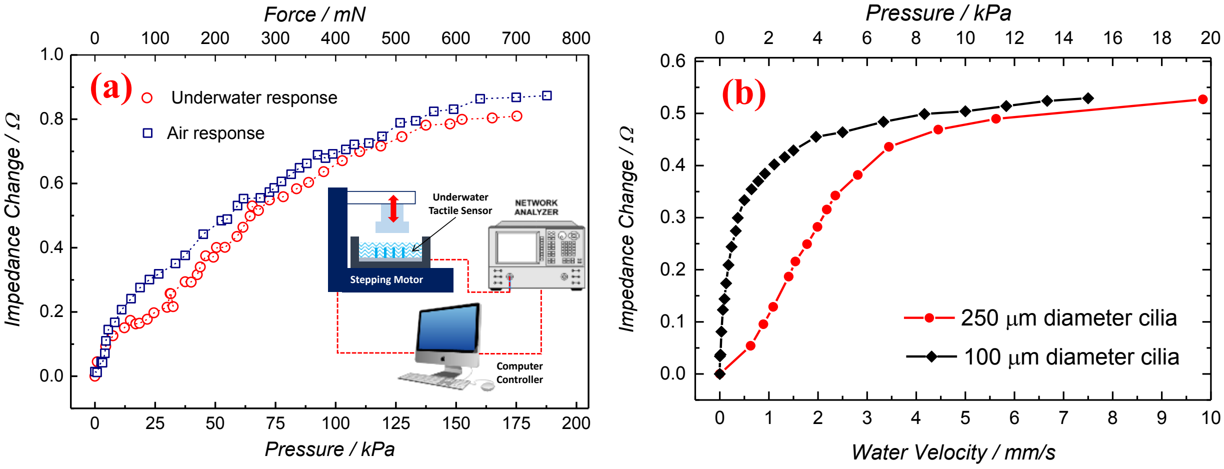

Figure 4-9: (a) Underwater performance of a tactile sensor with 1 mm long and 200 μm in diameter cilia. Inset: Test setup for underwater experiment. (b) Water flow sensor response of sensors with cilia that are 500 μm long and have a diameter of 100 μm and 250 μm.

4.2 Bioinspired Flow Sensor: Shear Force Detection

4.2.1 Introduction to Flow Sensors

The micro-scale, hair-like cilia structures exist in many creatures as mentioned earlier, including species that live in water. Taking fish as an example, the neuron stimulated cilia that extend from the organisms' cells, assist in performing a variety of functions such as preying or avoiding danger [31]. When the cilia are exposed to a change in the fluid flow, they bend and transmit a signal that is then translated into a specific function.

Recently, artificial cilia have been developed that could be used for various applications such as cell mechanics study [35, 41], microfluidic propulsion [36, 37], and flow sensing [31]. For the hair flow sensors, different techniques have been utilized to detect cilia bending, due to flow such as thermal, piezoresistive, piezoelectric and magnetic [31].

A piezoresistive hair flow sensor realized by Chen *et al.* consists of a 600 µm by 80 µm vertical SU-8 hair-like structure fabricated by photolithography and a silicon resistor. The sensor was able to detect constant air flow between 0 to 20 m/s with a resolution of 100 mm/s and water flow from 0 to 0.4 m/s with a resolution of 5 mm/s. The sensor was also able to detect alternating flow velocity amplitudes down to the order of 0.7 mm/s in water at a frequency of 50 Hz [156].

Flow sensors based on a vertical cilium and a strain gauge were developed by Liu *et al.* The study included two prototypes: silicon-based and polymer-based cilia. The silicon-based sensor was mounted on a glass plate and placed in a water tunnel with laminar flow. For water flows with velocities from 0 to 1 m/s, a sensitivity of 0.5 mm/s was reported. The response of the polymer-based sensor increases exponentially within the tested range, when applying air flow with velocities ranging from 0 to 30 m/s. Chang concluded that silicon-based flow sensors showed higher sensitivity, whereas polymer-based sensors were more robust [59]. Hein *et al.* proposed an inorganic nano-cilia sensor based on magnetic NWs that utilizes the stray magnetic field of cobalt NWs for a biomimetic sensing approach. The NWs are mounted on a giant-magneto-resistive sensor to detect their motion. The sensor has two possible applications: flow sensing and vibration sensing. Water flows were detected from 3.3 m/s to 40 m/s with a sensitivity of 0.55 μV/m/s and a signal to noise ratio of 44, and vibrations in the low earthquake-like frequency range of 1–5 Hz [65]. The stiffness of the bare magnetic NWs prevents the measurement of low flow velocities. Nanocilia made of metals like Co have high possibility of corrosion, limiting their use for applications in, e.g., microfluidic devices. Magnetic polymer cilia have also been realized using superparamagnetic nanoparticles embedded in thin polymer films for various applications (section 2.3). This approach requires the application of rather large magnetic fields. For instance, Khaderi *et al.* applied a rotational magnetic field of 115 mT in amplitude and Digabel *et al.* used 23×10^3 $T.m^{-1}$ magnetic field gradient to actuate the cilia. A favorable property of magnetic cilia is the absence of an electric contact and the possibility of remote detection or actuation [157].

Recently, there has been a great interest in developing sensors with low power consumption. However, reducing the power consumption usually leads to a reduction in the resolution. For example, a low power thermal flow sensor developed by Cubukcua *et al.* shows a resolution below 10 mm/s at 177 μW [158]. High-resolution thermal flow sensors have a power consumption of more than 1 mW [159]. In this regard, hair flow sensors are attractive options and have been shown to operate at a power consumption as low as 140 μW providing a resolution of 0.9 m/s [65].

4.2.2 Sensor Design

The high elasticity of the nanocomposite cilia [22], together with the good resistance to corrosion, enables the detection of extremely low flow velocities making the cilia concept appealing for flow sensing. The developed flow sensor is composed of eight nanocomposite cilia that are 500 μm long and 100 μm in diameter, with 18% NWs to PDMS volume ratio. The artificial cilia are fabricated on top of an 8 mm long and 400 μm wide GMI sensor strip that was fabricated as mention in section 3.10.2. Illustration of the flow sensor operation principle is shown in Figure 4-10. It uses the same mechanism mentioned in section 3.3.5 where the cilia are deflected from the fluid flow that provides the force to the cilia. At resting position, the stray field of the cilia affects the GMI sensor with an average magnetic field value $H(0)$ that biases the sensor and changes its initial impedance. In the presence of a fluid flow, the cilia bend in the flow direction. This bending results in a change of the stray field of the cilia with an average magnetic field value $H(\delta)$ affecting the GMI sensor, and hence changing its impedance.

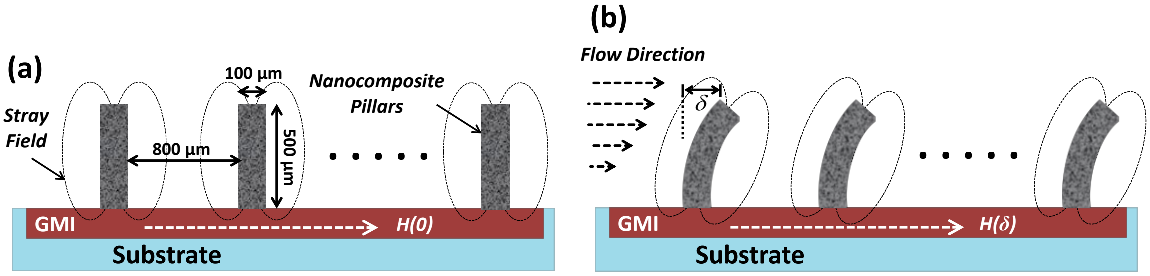

Figure 4-10: Illustration of the flow sensor operation principle. (a) A GMI sensor is used to detect the stray field of the magnetic nanocomposite cilia, which is, on average, $H(0)$ without fluid flow. (b) Fluid flow causes the cilia to bend (δ is the tip deflection), changing the average field to $H(\delta)$.

The flow signal is obtained as the impedance change ΔZ, which is the difference between the GMI sensor's impedance Z_δ, when a flow is applied and the cilia' tips are deflected by δ, and the initial impedance Z_0, when no flow is applied and $\delta = 0$. The impedance can be calculated from the average magnetic field value at the GMI sensor and the sensitivity of the GMI sensor S_{GMI}, which is assumed to be constant about the operation point. The sensitivity S of the flow sensor is the impedance change over the average flow velocity $v_{avg}(\delta)$:

$$S = \frac{\Delta Z}{v_{avg}(\delta)} = \frac{Z_\delta - Z_0}{v_{avg}(\delta)} = \frac{S_{GMI}\left[H(\delta) - H(0)\right]}{v_{avg}(\delta)} \qquad 4\text{-}1$$

Using S together with the maximum impedance fluctuation Z_f (noise), the resolution is:

$$R = Z_f / S. \qquad 4\text{-}2$$

The velocity inside the fluidic channel for a laminar flow is not constant but changes across the cross section area of the channel. The velocity is highest along the center of the channel and it is reducing toward the channel walls. The average flow velocity v_{avg} is estimated to be one half of the maximum flow velocity [160].

Using the displacement-force relationship of an elastic cylindrical beam as discussed in section 3.4, the value of δ can be expressed for a force F along the length of the cilia as [161]:

$$\delta = \frac{64}{3} F \frac{l^3}{\pi E D^4} = \frac{64}{3}\left(\frac{1}{2}\rho v_{avg}(\delta)^2 C_D A(\delta)\right)\frac{l^3}{\pi E D^4} \qquad \text{4-3}$$

where l, E, and D are the length, the Young's modulus and the diameter of the cilia, respectively. The force is proportional to the fluid density ρ, drag coefficient C_D and the area of the cilia that is facing the flow $A(\delta)$, which is a function of δ, since the effective area is reducing as the cilia bend. C_D is computed by [162]:

$$C_D = 0.8 + \frac{13.6}{Re} = 0.8 + \left(\frac{13.6\mu_d}{\rho v_{avg}(\delta) D_h}\right) \qquad \text{4-4}$$

where Re is the Reynolds number, D_h is the hydraulic diameter and μ_d is the fluid dynamic viscosity.

The flow sensor is tested inside a fluidic channel, which is 1 mm high, 10 mm wide and 15 mm long and has an inlet and an outlet. The channel is fabricated with the laser cutter using three layers of PMMA substrates bonded by applying chloroform at the bonding joints and pressing the substrates by hand. The channel is then bonded to the sensor's substrate using instant room temperature curing adhesive. The channel provides a small value of Re to avoid turbulence and achieve laminar flow. The fabricated nanocomposite cilia on the GMI sensor is shown in (Figure 4-11).

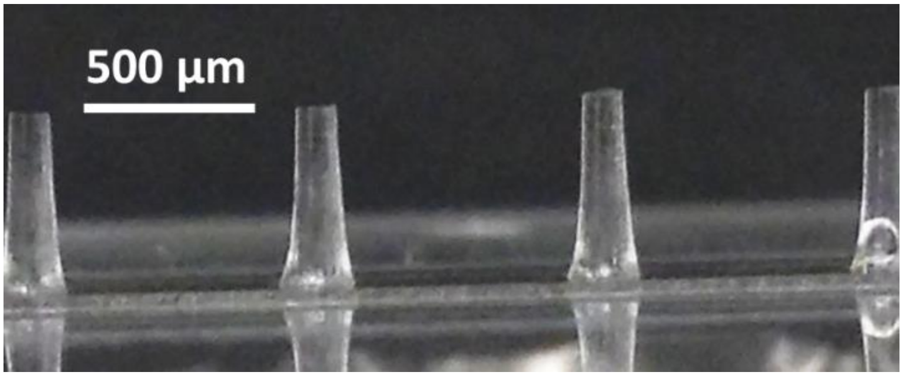

Figure 4-11: Optical image of the fabricated nanocomposite cilia with 500 µm in length and 100 µm in diameter.

4.2.3 Sensors Characterization

Prior to testing the magnetic hair flow sensor, the GMI sensor is characterized in order to obtain the sensitivity S_{GMI}. Using a Helmholtz coil, a magnetic field from 0 Oe to 100 Oe with increments of 1 Oe is applied to the GMI sensor, and the impedance is obtained with an impedance analyzer (Agilent E4991A) at a current of 2 mA in amplitude and a frequency from 10 to 500 MHz (Figure 4-12a). The GMI sensor response shows a peak at a field of 11 Oe corresponding to the anisotropy field of the $Ni_{80}Fe_{20}$ thin film. The response of the GMI sensor at 500 MHz and for fields applied in the longitudinal and transverse direction is shown in Figure 4-12b. As can be seen, the GMI sensor is magnetically sensitive in the longitudinal direction while no significant impedance change is observed in the transverse direction. The GMI ratio, which is the maximum impedance change obtained with respect to the impedance at saturation field, is 20% and 1.3% in the longitudinal and transverse direction, respectively. This anisotropic magnetic property of the GMI sensor provides a good selectivity in terms of the direction of the magnetic signal that is being measured. The value of S_{GMI} is estimated through a linear fit of the GMI sensor's response between 0 Oe and 11 Oe, as shown in Figure 4-12b, which includes the operating range, within which the magnetic fields are varying with the deflection. S_{GMI} increases with increasing frequency (Figure 4-12c), therefore, 500 MHz is selected as the operating frequency, where S_{GMI} is 0.67 Ω/Oe.

The flow sensor is tested by applying air and water volumetric flow rates using a syringe pump through a channel inlet in both sensitive and non-sensitive directions of the GMI sensor. The experimental setup is shown in Figure 4-13. The average flow velocity is calculated by dividing the applied volumetric flow rate by the channel cross-section area of 10 mm^2. The impedance magnitude of the GMI sensor is measured with the impedance analyzer at a current of 2 mA in amplitude and 500 MHz in frequency. A set of 10 data points at every flow velocity value is recorded over a period of 30 seconds. The values for Z_δ and Z_f are obtained from the average value and the maximum deviation from the average value, respectively. The current dependence of the flow sensor is tested for current amplitudes between 0.1–10 mA, which are the limits of the impedance analyzer.

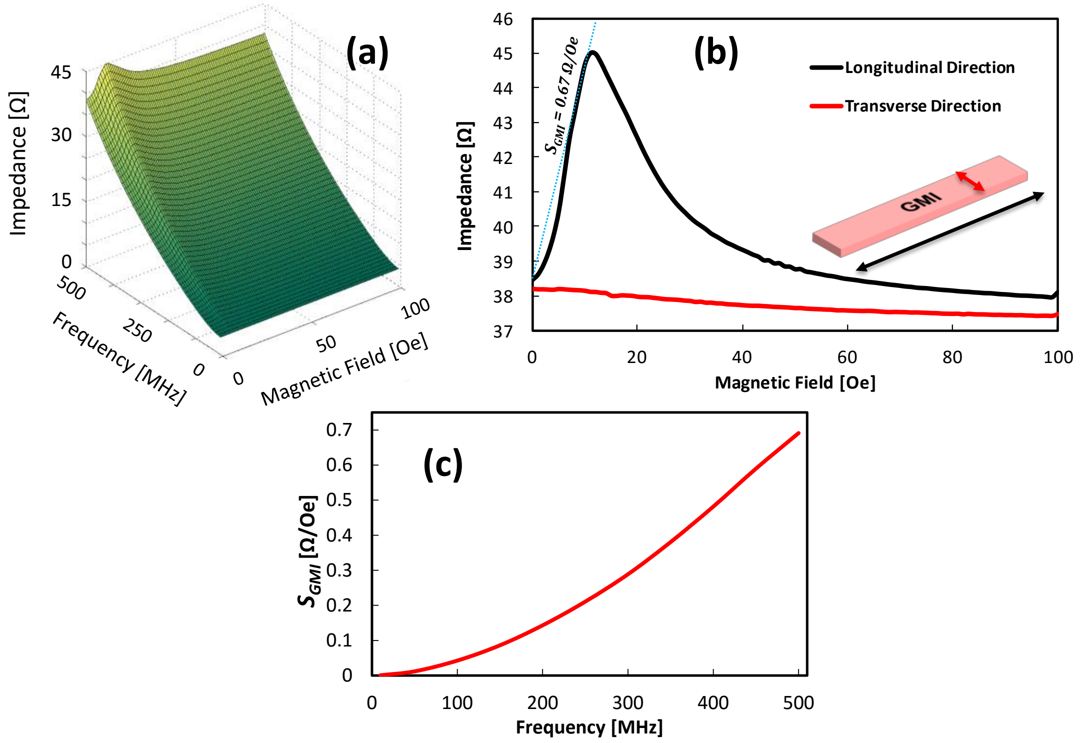

Figure 4-12: (a) Impedance characterization of the GMI sensor as a function of the frequency and the magnetic field applied in the longitudinal direction. (b) Impedance response of the GMI sensor with external magnetic fields applied in the sensitive (longitudinal) and non-sensitive (transverse) directions at 500 MHz. The GMI sensor sensitivity S_{GMI} was determined by a linear fit. (c) S_{GMI} along the sensitive direction as a function of the frequency.

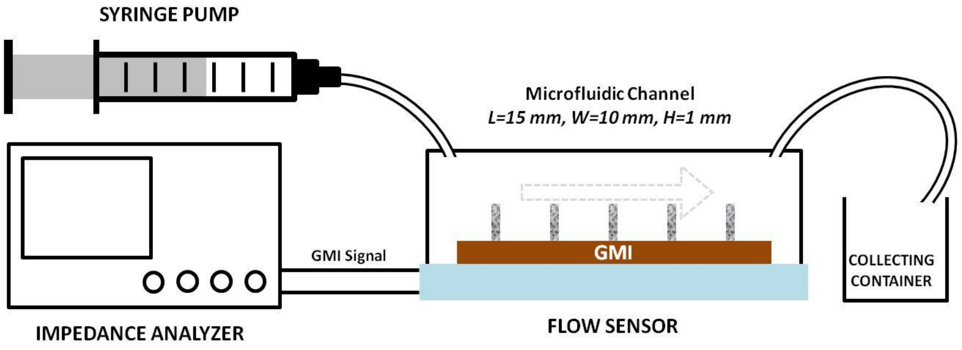

Figure 4-13: Flow sensor experimental setup.

4.2.4 Computational Model

The response of the flow sensor is computed from Eq. 4-1 and 4-3 using a remanence magnetization of 2.1 memu and $S_{GMI} = 0.67\ \Omega/\mathrm{Oe}$. The eight cilia are modeled by finite element simulations as 3D cylindrical beams as discussed in section 3.8. The magnetic fields affecting the GMI sensor are studied upon the deflection of the nanocomposite cilia. The magnetic NWs are accounted for by assigning flux density vectors to the cilia, which are calculated from the NWs' remanence value and the amount of NWs in the cilia. Fluid flow is simulated by rotating the cilia about the anchor point by the angle *θ,* which is related to the deflection by:

$$\delta = l.\sin(\theta). \tag{4-5}$$

This changes the effective area of the cilia that is facing the flow to:

$$A(\theta) = \frac{\pi D}{2} l.\cos(\theta). \tag{4-6}$$

The average value of the magnetic field at the GMI sensor is:

$$H(\theta) = \frac{1}{n}\sum_{i=1}^{n}(H_x)_i, \tag{4-7}$$

where H_x is the component of the magnetic vector field along the GMI sensor's sensitive direction, i is the summation index and n is the number of magnetic vectors used in the averaging process. The average magnitude of the magnetic field is calculated as:

$$H_{mag}(\theta) = \frac{1}{n}\sum_{i=1}^{n}.\left(\sqrt{H_x{}^2}\right)_i. \tag{4-8}$$

When the cilia are straight, an average magnetic vector field of 0 Oe is obtained, due to the symmetry of the stray field. However, the magnitude of the magnetic field in this case is 3.2 Oe, which can be considered as the bias field of the GMI sensor. As the cilia deflect, the stray field at the GMI sensor increases on one side of the cilia and decreases on the other side, causing the average magnetic field value to increase. When the cilia are fully deflected, the magnetic field reaches an average value of 1.3 Oe.

$v_{avg}(\delta)$ is calculated by combining Eq. 4-44-3, where $A(\delta)$ can be derived from Equations 4-5 and 4-6 as:

$$A(\delta) = \frac{\pi D}{2}\left(\frac{\delta}{\sin(\theta)}\right).\cos(\theta) = \frac{\pi D\delta}{2\tan(\theta)}\,. \qquad 4\text{-}9$$

The flow sensor's impedance change can now be calculated from Eq. 4-1 by relating $H(\delta)$ to the corresponding $H(\theta)$ and using S_{GMI} from the experiment.

4.2.5 Experiments and Results

The results of the flow experiments are shown in (Figure 4-14a) for air and (Figure 4-14b) for water, respectively. The sensor is sensitive to average air flow velocities from 0 to 190 mm/s with maximum values of S = 24 mΩ/(mm/s) and R = 0.56 mm/s. In case of water, the sensor operates in the range from 0 to 7.8 mm/s with maximum values of S = 0.9 Ω/(mm/s) and R = 15 μm/s. The range of flow rates is lower for water than for air, due to the higher density of water, causing larger forces to be exerted on the cilia. In both cases the response is increasing in a relatively linear manner (±5%) between 0 and 0.6 mm/s for water flow and between 0 and 18 mm/s for air flow, with the slopes representing the maximum sensitivity. Another linear region (±3%) is observed for water flow between 1.9 and 7.8 mm/s with S = 13.5 mΩ/(mm/s), and between 40 and 190 mm/s with S = 0.7 mΩ/(mm/s) for air. Completely bending the cilia results in saturating the impedance change at 0.53 Ω and 0.54 Ω for air and water flows, respectively.

The orientation of the fluidic channel with respect to the GMI sensor's alignment is changed, in order to test the flow sensor along the non-sensitive direction. A smaller response of about 10% compared to the sensitive direction is obtained with the saturation values of 0.059 Ω for air and 0.061 Ω for water.

Figure 4-14 also shows the theoretical response of the flow, which is in close agreement with the experimental results. A slightly higher saturation value of 5.7 Ω is obtained from the theoretical model. This is most likely due to the actual magnetization of the cilia being lower than expected, indicating a lower NW concentration than expected. Theoretical impedance values at the knee region, which corresponds to around 70 degrees cilia deflection, are higher than the experimental values, due to the assumption of rotation of straight cilia rather than their bending and neglecting the fact that the actual flow velocity inside the channel is reducing toward the channel walls.

The performance of the flow sensor can be modified easily by changing the mechanical parameters of the cilia. Changing the diameter of the cilia, for example, leads to a different operating range, resolution and sensitivity (Figure 4-15). To demonstrate this point, a flow sensor is fabricated with 500 μm long and 250 μm in diameter nanocomposite cilia that have the same Fe NWs volume as the 100 μm cilia. The modified sensor operates in the range from 0 to 12 mm/s with maximum values of S = 0.17 Ω/(mm/s) and R = 79 μm/s.

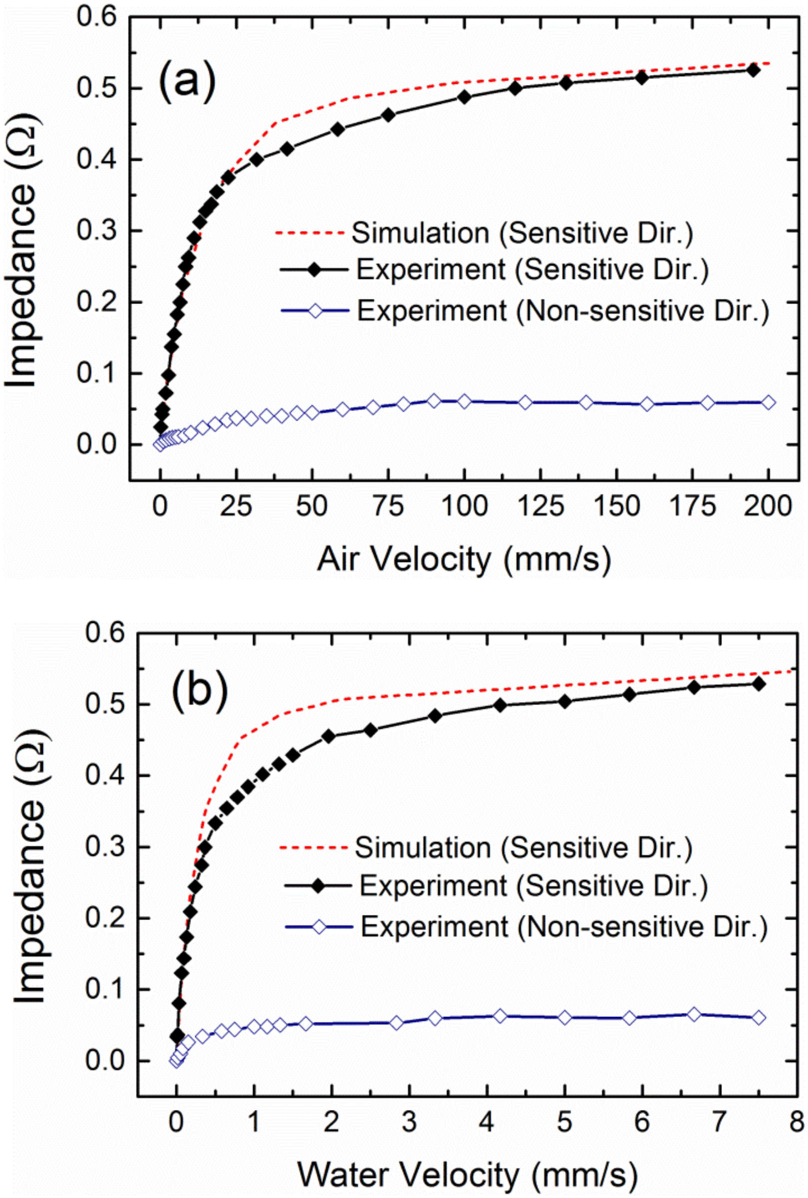

Figure 4-14: Experimental and simulated impedance change of the flow sensor at different flow velocities along the GMI sensor's sensitive direction and non-sensitive direction for (a) air flow and (b) water flow.

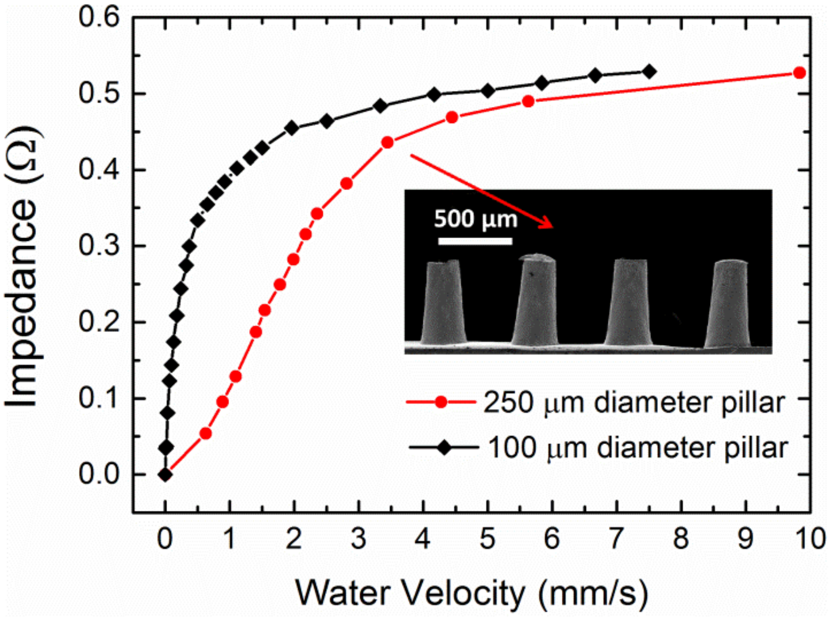

Figure 4-15: Experimental impedance change of flow sensors with cilia of 100 µm and 250 µm in diameter and 500 µm in length at different flow velocities along the GMI sensor's sensitive direction for water flow. The fabricated cilia with 250 µm in diameter are shown in the inset.

The average power consumption of the flow sensor, when operated at 2 mA current amplitude, is 31.6 µW. The power consumption can be further reduced by operating the sensor at lower current amplitudes. The current dependence of the flow sensor is shown in Figure 4-16. As can be seen, there is almost no influence of the current on the measured impedance value with slightly higher values obtained at low current amplitudes. The impedance of the GMI sensor at 2 mA driving current has fluctuations of Z_f = 0.0135 Ω, while Z_f = 0.0292 Ω and Z_f = 0.0096 Ω at 0.1 mA and 10 mA, respectively. This indicates that the signal stability can be enhanced by increasing the driving current, and hence increasing the resolution at the expense of power consumption. The operation at 10 mA leads to a slightly improved resolution of 10 µm/s at a power consumption of 790 µW. When operated at 0.1 mA, the power consumption can be reduced to as little as 80 nW, with the resolution still being 32 µm/s.

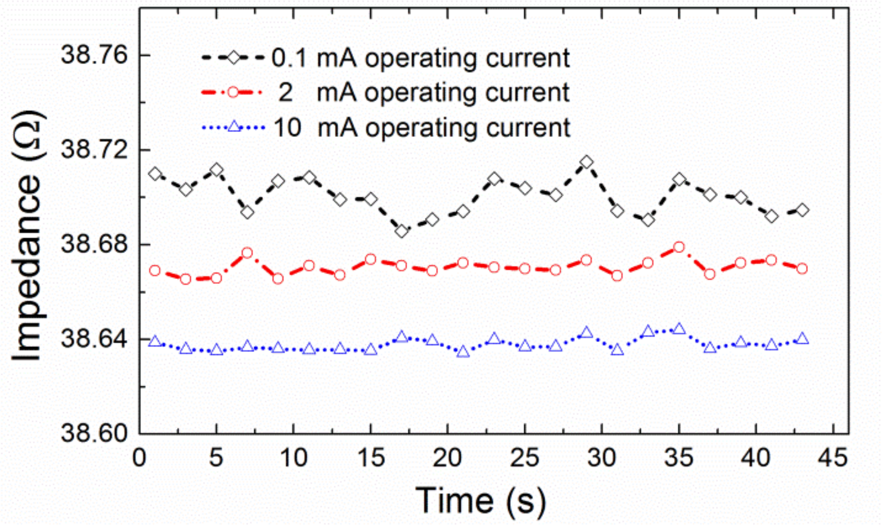

Figure 4-16: Flow sensor impedance fluctuation over time for different current amplitudes.

5 CONCLUSION & FUTURE PERSPECTIVES

5.1 Conclusion

Natural cilia were mimicked by fabricating a novel permanent magnetic and highly elastic nanocomposite cilia consisting of PDMS polymer with embedded Fe NWs, which generate a stray field. The cilia were integrated on a GMI thin film sensor to detect the change of the cilia' stray fields, resulting from bending them upon the application of an external force. The permanent magnetic property of the NWs eliminated the need for an external magnetic field source for both magnetizing the nanocomposite and biasing the GMI sensor. GMI sensors are used because of their high sensitivity and simple fabrication, and it is worth to note that they could be implemented as wireless devices which could be utilized to realize passive and remote sensors [138, 163]. Employing the reported concept, highly sensitive, power efficient and multifunctional tactile and flow sensors were realized which can operate in air and liquid. The nanocomposite cilia demonstrated unique features including biocompatibility, good corrosion resistance, and the ability to operate in harsh conditions. The proposed concept has wide range of flexibility to achieve: a sensor with extremely high sensitivity within an ultra-low-pressure regime (<500 Pa) for microfluidics or biological detection, a sensor with high degree of sensitivity in the low-pressure regime (<10 kPa) for electronic skins and health monitoring systems, or a sensor with wide range of operation up to 300 kPa for industrial applications.

The tactile sensors were realized on flexible and rigid substrates. Various dynamic studies were conducted with the tactile sensor demonstrating the detection of moving objects and textured surfaces with extremely low power consumption of 80 nW. Different cilia configurations were designed, confirming the possibility to easily control the sensors' performance with the cilia's arrangements or dimensions. A specific feature of the cilia tactile sensor is its ability to measure flow, which is unique in the realm of tactile sensors.

The developed nanocomposite cilia flow sensor can be used for both water and air flow measurement applications and has an operating range in case of air flow between 0 and 190 mm/s with a sensitivity up to 24 mΩ/(mm/s) and a resolution of 0.56 mm/s, and in case of water flow the operating range is between 0 and 7.8 mm/s with a sensitivity up to 0.9 Ω/(mm/s) and a resolution of 15 µm/s. The achieved resolution is high compared to previously reported flow sensors [31, 59, 65, 156, 158], with a very low power consumption of 31.6 µW compared to reported thermal flow sensors with 177 µW [158] or hair flow sensors with 140 µW [65]. The power consumption can even be reduced to 80 nW, with only a small decrease of the resolution of water flow to 32 µm/s. A magnetic NWs-based flow sensor was proposed by Hein *et al.* that offer the advantage of extremely small dimensions but suffers from the possibility of corrosion, and the high stiffness that prevents detection of low flow velocities. The developed flow sensor in this dissertation has a good corrosion resistance, is highly elastic, and uses a simple and cost-effective fabrication method compared with a conventional soft lithography process that demands templates prepared in specialized facilities with expensive consumables. The eight cilia design was arranged in a manner allowing full deflection of each cilium without touching each other. This design provides an average signal over a length of 8 mm and can be readily adjusted to meet other requirements. This has been demonstrated by modifying the cilia' diameter from 100 µm to 250 µm, which increased the flow velocity range at the cost of sensitivity and resolution. The performance of the proposed hair flow sensor could be further improved by optimizing the sensitivity of the GMI sensor or increasing the NWs concentration in the nanocomposite.

In general, the mold-based microfabrication process and magnetic operation principle enable a high degree of integration, which together with the extremely low power consumption make the artificial cilia sensor an attractive solution for many applications.

5.2 Future Perspectives

The developed nanocomposite cilia sensor concept showed great potential for a wide range of applications, opening the door for new projects in the future. Further optimization of the nanocomposite fabrication process is required to obtain full control over the NWs concentration and ensure uniform dispersion of the NWs throughout the nanocomposite cilia. Currently, the process utilized to make the nanocomposite cannot guarantee a precise NWs concentration in the nanocomposite. The dispersion issue can be improved by investigating techniques like better nanocomposite sonication, or by coating the NWs with Polyethylene glycol (PEG) prior to mixing with PDMS. Another issue is having no NWs in parts of the cilia, which is mainly due to the magnetic field source utilized to align the NWs. One important enhancement is, therefore, the utilization of a highly uniform magnetic field over a wide range to align the NWs efficiently (e.g. Helmholtz Coil). An observed issue is the easy corrosion of polycrystalline Fe NWs. The investigation of different NW materials can be conducted in the future to obtain better permanent nano-magnets that offer a large stray field and do not corrode as fast as polycrystalline Fe. A candidate material is single crystal Fe NWs as discussed in section 3.9.1.

Future work can also include mapping the stray field of the nanocomposite cilia and conducting an in-depth study on the stray field behavior of nanocomposites with different NWs concentrations and different alignment directions. This study can allow optimizing the performance of the cilia sensor.

One key challenge was the poor adhesion of the nanocomposite cilia to silicon or Kapton, which was solved by spinning and curing a thin film of PDMS on the substrate prior to the fabrication of the cilia. Alternative solutions can be investigated such as chemical or physical surface treatments to improve the adhesion. Different substrate materials could also be utilized (e.g. PDMS) to allow obtaining a robust cilia sensor.

GMI sensors were used due to their great advantages such as high sensitivity, simple fabrication, robustness and the possibility to integrate the sensor with RF transducers for wireless operation, which could be useful for specific applications. The high-frequency operation of the GMI sensor does not allow easy utilization of sensor arrays, and complex circuitry is required. The cilia sensor design can be modified by replacing the GMI sensor with other magnetic sensors to allow the realization of a sensor array that operates at DC or low-frequency currents, which require much simpler circuitry. Magnetic field sensors like contemporary magnetic tunnel junctions or giant magneto-resistive sensors might offer advantages over the GMI sensor.

To put the developed nanocomposite cilia sensors in the context of practical applications, an investigation on their performance when equipping a robotic arm or a prosthetic glove under extreme conditions will be interesting. This will validate the suitability of the sensor for wearable applications in general. A step toward this goal has been conducted by investigating the tactile sensor for specific applications like Braille characters reading. The tactile sensor is currently also being studied on tweezers and catheters for the potential of developing smart surgical tools. Other applications are envisioned like the development of smart and disposable artificial skins for underwater and marine applications. Designing a full system with the required circuitry can allow bringing the cilia sensor concept to the market.

REFERENCES

[1] J. M. D. Coey, *Magnetism and Magnetic Materials* vol. 1. UK: Cambridge University Press, 2009.

[2] C. Goodyear, "Method for Fabrication of objects that are more or less hard, flexible or elastic, rubber and gutta percha in combination with other substances," *Dinglers Polytechnisches Journal* vol. 139, pp. 376-390, 1856.

[3] D. Godovsky, "Device Applications of Polymer-Nanocomposites," *Advances in Polymer Science,* vol. 153, p. 163, 2000.

[4] C. Yamahata, C. Lotto, E. Al-Assaf, and M. A. M. Gijs, "A PMMA valveless micropump using electromagnetic actuation

" *Microfluid Nanofluid,* vol. 1, p. 197, 2005.

[5] E. Diller, S. Miyashita, and M. Sitti, "Remotely addressable magnetic composite micropumps," *RSC Advances,* vol. 2, p. 3850, 2012.

[6] J. Thevenot, H. Oliveira, O. Sandre, and S. Lecommandoux, "Magnetic responsive polymer composite materials," *Chem. Soc. Rev.,* vol. 42, p. 7099, 2013.

[7] Y. Yamanishi, S. Sakuma, Y. Kihara, and F. Arai, "Fabrication and application of 3-D magnetically driven microtools," *Journal of Microelectromechanical Systems,* vol. 19, p. 350, 2010.

[8] B. A. Evans, A. R. Shields, R. L. Carroll, S. Washburn, M. R. Falvo, and R. Superfine, "Magnetically Actuated Nanorod Arrays as Biomimetic Cilia," *Nano Letters,* vol. 7, p. 1428, 2007.

[9] M. Alnassar, A. Alfadhel, Y. Ivanov, and J. J Kosel, "Magnetoelectric polymer nanocomposite for flexible electronics," *Journal of Applied Physics* vol. 117 p. 17D711, 2015.

[10] J. Yakhmi, "Molecule-based magnets," *Bulletin of Materials Science,* vol. 32, p. 217, 2009.

[11] F. Carosio, A. Fina, and M. Coisson, "Polypropylene-based ferromagnetic composites," *Polymer Bulletin,* vol. 65, p. 681, 2010.

[12] M. Suter, O. Ergeneman, J. Zürcher, C. Moitzi, S. Pané, T. Rudin*, et al.*, "A photopatternable superparamagnetic nanocomposite: Material characterization and fabrication of microstructures," *Sensors and Actuators B: Chemical,* vol. 156, pp. 433-443, 2011.

[13] B. Frka-Petesic, J. Fresnais, J. F. Berret, V. Dupuis, R. Perzynski, and O. Sandre, "Stabilization and controlled association of superparamagnetic nanoparticles using block copolymers," *J. Magn. Magn. Mater.,* vol. 321, pp. 667–670, 2009.

[14] K. P. Yuet, D. K. Hwang, R. Haghgooie, and P. S. Doyle, "Multifunctional Superparamagnetic Janus Particles," *Langmuir* vol. 6, pp. 4281-4287, 2010

[15] Q. Zhou, W. D. Ristenpart, and P. Stroeve, "Magnetically induced decrease in droplet contact angle on nanostructured surfaces," *Langmuir* vol. 19, pp. 747–751, 2011.

[16] Q. A. Pankhurst, J. Connolly, S. K. Jones, and J.-. Dobson, "Applications of magnetic nanoparticles in biomedicine," *J. Phys. D: Appl. Phys.,* vol. 36, pp. R167-R181, 2003.

[17] I. Koh and L. Josephson, "Magnetic Nanoparticle Sensors," *Sensors and Actuators B: Chemical,* vol. 9, pp. 8130-8145, 2009.

[18] F. Li and J. Kosel, "A magnetic method to concentrate and trap biological targets," *IEEE Transactions on Magnetics,* vol. 48, pp. 2854-2856, 2012.

[19] F. Li, I. Giouroudi, and J. Kosel, "A biodetection method using magnetic particles and micro traps," *Journal of Applied Physics* vol. 111, p. 07B328, 2012.

[20] X. He, W. Zhong, C.-T. Au, and Y. Du, "Size dependence of the magnetic properties of Ni nanoparticles prepared by thermal decomposition method," *Nanoscale Research Letters,* vol. 8, p. 446, 2013.

[21] E. F. Kneller and F. E. Luborsky, "Particle Size Dependence of Coercivity and Remanence of Single Domain Particles," *Journal of Applied Physics,* vol. 34, p. 656, 1963.

[22] K. Keshoju and L. Sun, "Mechanical characterization of magnetic nanowire–polydimethylsiloxane composites," *Journal of Applied Physics,* vol. 105, p. 023515, 2009.

[23] M. Teich, "Purkyne and Valentin on ciliary motion: an early investigation in morphological physiology," *Brit. J. Hist. Sci.,* vol. 5, pp. 168–177, 1970.

[24] B. Lewin, *Cells*: Jones & Bartlett Learning, 2010.

[25] Y. Enuka, I. H. O. Edelheit, H. Vaknine, and A. Hanukoglu, "Epithelial sodium channels (ENaC) are uniformly distributed on motile cilia in the oviduct and the respiratory airways," *Histochem Cell Biol.,* vol. 137, pp. 339–353, 2012.

[26] M. B. Gardiner, "The Importance of Being Cilia," *HHMI Bulletin (Howard Hughes Medical Institute),* vol. 18, 2005.

[27] U. Wolfrum and A. Schmitt, "Rhodopsin transport in the membrane of the connecting cilium of mammalian photoreceptor cells," *Cell motility and the cytoskeleton,* vol. 46, pp. 95-107, 2000.

[28] M. Burrows and G. Sutton, "Interacting Gears Synchronize Propulsive Leg Movements in a Jumping Insect," *Science* vol. 341, pp. 1254-1256, 2013.

[29] G. J. M. Krijnen, M. Dijkstra, J. J. v. Baar, S. S. Shankar, W. J. Kuipers, Rik J H de Boer*, et al.*, "MEMS based hair flow-sensors as model systems for acoustic perception studies," *Nanotechnology,* vol. 17, p. S84, 2006.

[30] J. Casas, T. Steinmann, and G. Krijnen, "Why do insects have such a high density of flow-sensing hairs? Insights from the hydromechanics of biomimetic MEMS sensors," *Journal of the Royal Society Interface,* vol. 7, p. 1487, 2010.

[31] J. Tao and X. Yu, "Hair flow sensors: from bio-inspiration to bio-mimicking—a review," *Smart Materials and Structures,* vol. 21, p. 113001, 2012.

[32] J. S. Mellor and J. S. Hyams, "Metachronism of cilia of the digestive epithelium of cirriformia tentaculata," *Micron,* vol. 9, pp. 91–94, 1969.

[33] M. M. Lagarde, M. Drexl, V. A. Lukashkina, A. N. Lukashkin, and I. J. Russell, "Outer hair cell somatic, not hair bundle, motility is the basis of the cochlear amplifier," *Nat. Neurosci.,* vol. 7, pp. 746-748, 2008.

[34] N. J. Sniadecki, A. Anguelouch, M. T. Yang, C. M. Lamb, Z. Liu, S. B. Kirschner*, et al.*, "Magnetic microposts as an approach to apply forces to living cells," *PNAS,* vol. 104, p. 14553, 2007.

[35] A. Ghanbari, V. Nock, S. Johari, R. Blaikie, X. Chen, and W. Wang, "A micropillar-based on-chip system for continuous force measurement of C. elegans," *Journal of Micromechanics and Microengineering,* vol. 22, p. 095009, 2012.

[36] S. N. Khaderi, C. B.Craus, J. Hussong, N. Schorr, J. Belardi, J. Westerweel*, et al.*, "Magnetically-actuated artificial cilia for microfluidic propulsion," *Lab Chip,* vol. 11, p. 2002, 2011.

[37] F. Fahrni, M. J. Prins, and L. IJzendoorn, "Micro-fluidic actuation using magnetic artificial cilia," *Lab on a chip,* vol. 9, p. 3413, 2009.

[38] K. Najafi, "Biomimetic Hair Sensors: Utilizing the Third Dimension

" in *IEEE Sensors*, Taipei, Taiwan, 2012.

[39] P. Schroeder, J. Schotter, A. Shoshi, M. Eggeling, O. Bethge, A. Hütten*, et al.*, "Artificial cilia of magnetically tagged polymer nanowires for biomimetic mechanosensing," *Bioinspiration & Biomimetics,* vol. 6, p. 46007, 2011.

[40] P. B. Dirk-Michael Drotlef, Aránzazu del Campo, "Magnetically Actuated Patterns for Bioinspired Reversible Adhesion (Dry and Wet) " *Adv. Mater. ,* vol. 26, pp. 775–779, 2014.

[41] A. A. Nathan J. Sniadecki, Michael T. Yang, Corinne M. Lamb, Zhijun Liu, Stuart B. Kirschner, Yaohua Liu, Daniel H. Reich, and Christopher S. Chen "Magnetic microposts as an approach to apply forces to living cells," *PNAS,* vol. 104 pp. 14553–14558, 2007.

[42] K. Takei, T. Takahashi, J. C. Ho, H. Ko, A. G. Gillies, P. W. Leu*, et al.*, "Nanowire active matrix circuitry for low-voltage macro-scale artificial skin," *Nature Materials,* vol. 9, pp. 821–826, 2010.

[43] C. Pang, G.-Y. Lee, T.-i. Kim, S. M. Kim, H. N. Kim, S.-H. Ahn*, et al.*, "A flexible and highly sensitive strain-gauge sensor using reversible interlocking of nanofibres," *Nature Mater. ,* vol. 11, pp. 795-801, 2012.

[44] S. C. B. Mannsfeld, B. C.-K. Tee, R. M. Stoltenberg, C. V. H.-H. Chen, S. Barman, B. V. O. Muir*, et al.*, "Highly sensitive flexible pressure sensors with microstructured rubber dielectric layers," *Nature Mater.,* vol. 9, pp. 859–864, 2010.

[45] G. Schwartz, B. C.-K. Tee, J. Mei, A. L. Appleton, D. H. Kim, H. Wang*, et al.*, "Flexible polymer transistors with high pressure sensitivity for application in electronic skin and health monitoring," *Nature Comm. ,* vol. 4, p. 1859, 2013.

[46] S. Mohsin, I. Tiwana, and N. Lovell, "A review of tactile sensing technologies with applications in biomedical engineering," *Sens. Actuators A,* vol. 179, p. 17, 2012.

[47] B. C.-K. Tee and e. al., "An electrically and mechanically self-healing composite with pressure- and flexion-sensitive properties for electronic skin applications," *Nature Nanotechnology,* vol. 7, p. 825, 2012.

[48] H. K. Kim, S. Lee, and K. S. Yun, "Capacitive tactile sensor array for touch screen application," *Sensors and Actuators A: Physical,* vol. 165, p. 2, 2011.

[49] D. J. Lipomi and et al., "Skin-like pressure and strain sensors based on transparent elastic films of carbon nanotubes," *Nature Nanotechnology,* vol. 6, p. 788, 2011.

[50] M. Zirkl and e. al., "An All-Printed Ferroelectric Active Matrix Sensor Network Based on Only Five Functional Materials Forming a Touchless Control Interface," *Advanced Materials,* vol. 23, p. 2069, 2011.

[51] A. D. Mazzeo and e. al., "Paper-Based Capacitive Touch Pads," *Advanced Materials,* vol. 24, p. 2850, 2012.

[52] J. Wu, X. Wen, and Z. L. Wang, "Taxel-Addressable Matrix of Vertical-Nanowire Piezotronic Transistors for Active and Adaptive Tactile Imaging," *Science,* vol. 340, p. 952, 2013.

[53] C. Pang, J. H. Koo, A. Nguyen, J. M. Caves, M. Kim, A. Chortos*, et al.*, "Highly Skin-Conformal Microhairy Sensor for Pulse Signal Amplification," *Adv. Mater. ,* vol. 27, pp. 634-640, 2015.

[54] D.-H. Kim, N. Lu, R. Ma, Y.-S. Kim, R.-H. Kim, S. Wang*, et al.*, "Epidermal Electronics," *Science* vol. 333, pp. 838-843, 2011.

[55] D.-H. Kim, N. Lu, R. Ghaffari, Y.-S. Kim, S. P. Lee, L. Xu*, et al.*, "Materials for Multifunctional Balloon Catheters With Capabilities in Cardiac Electrophysiological Mapping and Ablation Therapy," *Nature Materials,* vol. 10, pp. 316-323, 2011.

[56] S. Gong, W. Schwalb, Y. Wang, Y. Chen, Y. Tang, J. Si*, et al.*, "A wearable and highly sensitive pressure sensor with ultrathin gold nanowires," *Nature Comm. ,* vol. 5, pp. 1-8, 2014.

[57] B. Zhu, Z. Niu, H. Wang, W. R. Leow, H. Wang, Y. Li*, et al.*, "Microstructured graphene arrays for highly sensitive flexible tactile sensors," *Small,* vol. 10, pp. 3625-3631, 2014.

[58] O. Yilmazoglu, A. Popp, D. Pavlidis, J. Schneider, D. Garth, F. Schüttler*, et al.*, "Vertically aligned multiwalled carbon nanotubes for pressure, tactile and vibration sensing," *Nanotechnology,* vol. 23, p. 085501, 2012.

[59] C. Liu, "Micromachined biomimetic artificial haircell sensors," *Bioinspiration and Biomimetic,* vol. 2, pp. S162-S169, 2007.

[60] T. Sharma, S. S. Je, B. Gill, and J. X. Zhang, "Patterning piezoelectric thin film PVDF-TrFE based pressure sensor for catheter application.," *Sens. Actuator A Phys.,* vol. 177, pp. 87–92, 2012.

[61] J. Dargahi, M. Parameswaran, and S. Payandeh, "A micromachined piezoelectric tactile sensor for an endoscopic grasper-theory, fabrication and experiments," *J. Microelectromech. Syst.,* vol. 9, pp. 329–335, 2000.

[62] H. B. Muhammad, C. M. Oddo, L. Beccai, C. Recchiuto, C. J. Anthony, M. J. Adams*, et al.*, "Development of a bioinspired MEMS based capacitive tactile sensor for a robotic finger," *Sens. Actuator A Phys.,* vol. 165, pp. 221–229, 2011.

[63] B. M. Cowie, D. J. Webb, B. Tam, P. Slack, and P. N. Brett, "Fiber Bragg grating sensors for distributive tactile sensing.," *Measur. Sci. Technol.,* vol. 18, pp. 138–146, 2007.

[64] S. M. De Rossi, T. Lenzi, N. Vitiello, M. Donati, A. Persichetti, F. Giovacchini*, et al.*, "Development of An In-Shoe Pressure-Sensitive Device for Gait Analysis," presented at the 35th Annual International Conference of the IEEE in Engineering in Medicine and Biology Society (EMBC), Boston, MA, USA, 2011.

[65] M. Hein, M. Maqableh, M. Delahunt, M. Tondra, A. Flatau, C. Shield*, et al.*, "Fabrication of bio inspired inorganic nanocilia sensors," *IEEE Trans. on Magnetics,* vol. 49, p. 191, 2013.

[66] A. Alfadhel, B. Li, O. Yassine, A. Zaher, and J. Kosel, "Magnetic Nanocomposite for Biomimetic Flow Sensing," *Lab Chip,* vol. 14, p. 4362, 2014.

[67] A. Alfadhel and J. Kosel, "Magnetic Nanocomposite Cilia Tactile Sensor," *Advanced Materials,* vol. 27, pp. 7888–7892, 2015.

[68] A. Mata, A. J. Fleischman, and S. Roy, "Characterization of Polydimethylsiloxane (PDMS) Properties for Biomedical Micro/Nanosystems," *Biomedical Microdevices,* vol. 7, p. 281, 2005.

[69] J. Moscowitz, "Actuation of Magnetic Particles in Polymer Nanoposts and their SelfAssembly to Three-Dimensional Microstructures," *PennScience,* vol. 4, 2005.

[70] D. J. Campbell, K. J. Beckman, C. E. Calderon, P. W. Doolan, R. H. Moore, A. B. Ellis*, et al.*, "Replication and Compression of Bulk Surface Structures with Polydimethylsiloxane Elastomer," *J. Chem. Educ.,* vol. 76, 1999.

[71] S. J. Clarson and J. A. Semlyen, *Siloxane Polymers*. Englewood Cliffs, NJ: Prentice-Hall, 1993

[72] ABCR, "Research Chemicals and Metals Catalogue Karlsruhe," ed. Germany, 1994

[73] D. W. Krevelen and P. J. Hoftyzer, *Properties of Polymers*. Amsterdam: Elsevier, 1976

[74] L. I. Mendelsohn, F. E. Luborsky, and T. O. Paine, "Permanent magnet properties of elongated single domain iron particles," *Journal of Applied Physics,* vol. 26, p. 1274, 1955.

[75] R. B. Falk, "A current review of Lodex permanent magnet technology," *Journal of Applied Physics,* vol. 37, p. 1108, 1966.

[76] D. J. Craik and R. Lane, "Magnetization reversal mechanisms in assemblies of elongated single-domain particles," *British Journal of Applied Physics,* vol. 18, p. 1269, 1967.

[77] Y. P. Ivanov, M. Vázquez, and O. Chubykalo-Fesenko, "Magnetic reversal modes in cylindrical nanowires," *Journal of Physics D: Applied Physics,* vol. 46, p. 485001, 2013.

[78] L. Sun and t. al., "Tuning the properties of magnetic nanowires," *IBM Journal of Research and Development,* vol. 49, pp. 79-102, 2005.

[79] J. A. Osborn, "Demagnetizing factors of the general ellipsoid," *Phys. Rev.,* vol. 67, pp. 351–357, 1945.

[80] R. Skomski and J. M. D. Coey, *Permanent magnetism*. Bristol, U.K.: Institute of Physics, 1999.

[81] E. V. Vidal and e. al., "A detailed study of magnetization reversal in individual Ni nanowires," *Applied Physics Letters,* vol. 106, p. 032403, 2015.

[82] M. Vázquez and e. al., "Magnetic behaviour of densely packed hexagonal arrays of Ni nanowires: Influence of geometric characteristics," *Journal of Magnetism and Magnetic Materials,* vol. 292, pp. 174-181, 2005.

[83] D. J. Sellmyer, M. Zheng, and R. Skomski, "Magnetism of Fe, Co and Ni nanowires in self-assembled arrays," *J. Phys.: Condens. Matter,* vol. 13 pp. R433–R460, 2001.

[84] M. Song, W. Song, H. Bi, J. Wang, W. Wu, J. Sun*, et al.*, "Cytotoxicity and cellular uptake of iron nanowires," *Biomaterials,* vol. 7, pp. 1509-1517, 2010.

[85] O. Gutfleisch, "Controlling the properties of high energy density permanent magnetic materials by different processing routes," *Journal of Physics D,* vol. 33, p. 157, 2000.

[86] M. Moskovits, 1993.

[87] L. Menon, M. Zheng, H. Zeng, S. Bandyopadhyay, and D. J. J. Sellmyer, "Size dependence of the magnetic properties of electrochemically self-assembled Fe quantum dots," *Journal of Electronic Materials,* vol. 29, pp. 510-515, 2000

[88] G. T. A. Huysmans and J. C. Lodder, "Magnetization curling in perpendicular iron particle arrays (alumite media)," *J. Appl. Phys. ,* vol. 64, p. 2016, 1988.

[89] H.-W. Liou, H.-M. Lin, Y.-K. Hwu, W.-C. Chen, W.-J. Liou, L.-C. Lai*, et al.*, "Synthesis and Characterization of Novel Hybrid Poly(methyl methacrylate)/Iron Nanowires for Potential Hyperthemia Therapy," *J. of Biomater. and Nanobiotech.,* vol. 1, pp. 50-60, 2010.

[90] Y. Henry, K. Ounadjela, L. Piraux, S. Dubois, J.-M. George, and J.-L. Duvail, "Magnetic anisotropy and domain patterns in electrodeposited cobalt nanowires," *European Physical Journal B,* vol. 20 pp. 35–54, 2001.

[91] R. Ferre and K. Ounadjela, "Magnetization processes in nickel and cobalt electrodeposited nanowires," *Physical Review B,* vol. 56, pp. 14066-14075, 1997.

[92] M. Hehn, K. Ounadjela, J. Bucher, F. Rousseaux, D. Decanini, B. Bartenlian*, et al.*, *Science* vol. 272 p. 1782, 1995

[93] S. Y. Chou, M. S. Wei, P. R. Krauss, and P. B. Fischer, "Study of Nanoscale Magnetic Structures Fabricated Using Electron-Beam Lithography and Quantum Magnetic Disk," *J. Vac. Sci. and Technol.,* vol. 6, p. 3695 1994.

[94] H. Masuda and K. Fukuda, "Ordered Metal Nanohole Arrays Made by a Two-Step Replication of Honeycomb Structures of Anodic Alumina," *Science,* vol. 5216, pp. 1466-1468, 1995.

[95] A. Sugawara, D. Streblechenko, M. McCartney, and M. R. Scheinfein, "Magnetic Coupling in Self-Organized Narrow-Spaced Fe Nanowire Arrays," *IEEE Trans. Magn. ,* vol. 34 pp. 1081-1083, 1998.

[96] J. P. O'Sullivan and G. C. Wood, "The Morphology and Mechanism of Formation of Porous Anodic Films on Aluminum," *Proceeding Royal Society London A,* vol. 317, p. 511, 1970.

[97] K. Nielsch and B. J. H. Stadler, "Template-based Synthesis and Characterization of High-density Ferromagnetic Nanowire Arrays," in *Handbook of Magnetism and Advanced Magnetic Materials*, ed: John Wiley & Sons, Ltd, 2007.

[98] K. Nielsch and e. al., "Uniform Nickel Deposition into Ordered Alumina Pores by Pulsed Electrodeposition," *Advanced Materials,* vol. 8, pp. 582-586, 2000.

[99] V. Vega, T. Böhnert, S. Martens, M. Waleczek, J. Montero-Moreno, D. Görlitz*, et al.*, "Tuning the magnetic anisotropy of Co–Ni nanowires: comparison between single nanowires and nanowire arrays in hard-anodic aluminum oxide membranes," *Nanotechnology,* vol. 46, p. 465709, 2012.

[100] M. Paunovic and M. Schlesinger, *Fundamentals of Electrochemical Deposition*: Wiley, 2006.

[101] Y. P. Ivanov, A. Alfadhel, M. Alnassar, J. E. Perez, M. Vazquez, A. Chuvilin*, et al.*, "Tunable magnetic nanowires for biomedical and harsh environment applications," *Scientific Reports,* vol. 6, p. 24189, 04/13/online 2016.

[102] R. G. Ehl and A. J. Ihde, "Faraday's electrochemical laws and the determination of equivalent weights. Journal of Chemical Education," vol. 31, p. 226, 1954.

[103] F. C. Strong, "Faraday's laws in one equation," *Journal of Chemical Education,* vol. 38, p. 98, 1961.

[104] Y. Liu, D. J. Sellmyer, and D. Shindo, *Handbook of Advanced Magnetic Materials: Vol 1. Nanostructural Effects. Vol 2. Characterization and Simulation. Vol 3. Fabrication and Processing. Vol 4. Properties and Applications*: Springer, 2008.

[105] Y. P. Ivanov, M. Vázquez, and O. Chubykalo-Fesenko, "Magnetic reversal modes in cylindrical nanowires. ," *J. Phys. D Appl. Phys.,* vol. 46, p. 485001 2013.

[106] J. A. Barreto and e. al., "Nanomaterials: applications in cancer imaging and therapy," *Adv. Mater.,* vol. 23, pp. H18-40 2011.

[107] M. Estrader and e. al., "Robust antiferromagnetic coupling in hard-soft bi-magnetic core/shell nanoparticles," *Nature Commun.,* vol. 4, p. 2960 2013.

[108] A. P. Chen and e. al., "Magnetic properties of uncultivated magnetotactic bacteria and their contribution to a stratified estuary iron cycle," *Nature Commun.,* vol. 5, p. 4797 2014.

[109] Y. T. Chong and e. al., "Multilayered Core/Shell Nanowires Displaying Two Distinct Magnetic Switching Events," *Adv. Mater.,* vol. 22, pp. 2435-2439, 2010.

[110] S. Timoshenko, *History of strength of materials*. New York: McGraw-Hill 1953.

[111] Y. Michael, S. Nathan, and C. Chen, "Geometric Considerations of Micro- to Nanoscale Elastomeric Post Arrays to Study Cellular Traction Forces," *Adv. Mater.,* vol. 19, p. 3119, 2007.

[112] J. M. Gere and B. J. Goodno, *Mechanics of Materials* vol. 1: CL Engineering, 2012.

[113] B. H. Weigl, R. Bardell, T. Schulte, F. Battrell, and J. Hayenga, "Towards non- and minimally instrumented, microfluidics-based diagnostic devices," *Biomedical Microdevices,* vol. 3 pp. 267–274, 2001.

[114] X. Gong, X. Yi, K. Xiao, S. Li, R. Kodzius, J. Qin*, et al.*, "Wax-bonding 3D microfluidic chips," *Lab on a Chip,* vol. 10 pp. 2622–2627, 2010.

[115] W. Wang, S. Zhao, and T. Pan, "Lab-on-a-print: from a single polymer film to three dimensional integrated microfluidics," *Lab on a Chip,* vol. 9, pp. 1133–1137, 2009.

[116] D. A. Bruzewicz, M. Reches, and G. M. Whitesides, "Low-cost printing of PDMS barriers to define microchannels in paper," *Analytical Chemistry,* vol. 80, pp. 3387–3392, 2008.

[117] H. Klank, J. P. Kutter, and O. Geschke, "Co2-laser micromachining and back-end processing for rapid production of pmma-based microfluidic systems," *Lab Chip,* vol. 2, pp. 242-246, 2002.

[118] D. Yuan and S. Das, "Experimental and theoretical analysis of direct-write laser micromachining of polymethyl methacrylate by Co2 laser ablation," *Journal of Applied Physics,* vol. 101, p. 024901, 2007.

[119] H. Becker and C. Gartner, "Polymer microfabrication methods for microfluidic analytical applications," *ELECTROPHORESIS,* vol. 21, pp. 12-26, 2000.

[120] C.-W. Tsao and D. DeVoe, "Bonding of thermoplastic polymer microfluidics," *Microfluidic s and Nanouidics,* vol. 6, pp. 1-16, 2009.

[121] D. Snakenborg, H. Klank, and J. P. Kutter, "Microstructure fabrication with a co 2 laser system," *Journal of Micromechanics and Microengineering,* vol. 14, p. 182, 2004.

[122] J.-Y. Cheng, C.-W. Wei, K.-H. Hsu, and T.-H. Young, "Direct-write laser micromachining and universal surface modi_cation of pmma for device development," *Sensors and Actuators B: Chemical,* vol. 99, pp. 186-196, 2004.

[123] F. Larmer and A. Schilp.

[124] D. C. Duffy, J. C. McDonald, O. J. A. Schueller, and G. M. Whitesides, "Rapid Prototyping of Microfluidic Systems in Poly(Dimethylsiloxane)," *Analyt. Chem.,* vol. 70, pp. 4974–4984, 1998.

[125] M. K. Chaudhury and G. M. Whitesides, "Direct Measurement of Interfacial Interactions Between Semispherical Lenses and Flat Sheets of Poly (Dimethylsiloxane) and Their Chemical Derivatives," *Langmuir,* vol. 7, pp. 1013–1025, 1991.

[126] S. Foner, "Versatile and Sensitive Vibrating-Sample Magnetometer," *Rev. Sci. Instrum. ,* vol. 7, pp. 548–557, 1959.

[127] D. Wang, L. Chang, Q. Wang, J. Cao, B. Farmer, and G. G. Dai, "Surface chemistry and electrical properties of germanium nanowires," *J. AM. CHEM. SOC.,* vol. 126, p. 11602, 2004.

[128] Q. Zhang, H. Zhang, G. Xie, and J. Zhang, "Effect of surface treatment of magnetic particles on the preparation of magnetic polymer microspheres by miniemul- sion

polymerization," *Journal of Magnetism and Magnetic Materials,* vol. 311, p. 140, 2007.

[129] A. Lu, E. Salabas, and F. Schuth, "Magnetic nanoparticles: synthesis, protection, functionalization, and application," *Angewandte Chemie-International* p. 1222, 2007.

[130] C. Hartsuijker and J. W. Welleman, *Engineering Mechanics* vol. 2: Springer, 2001.

[131] Z. Wang, A. A. Volinsky, and N. D. Gallant, "Crosslinking effect on polydimethylsiloxane elastic modulus measured by custom-built compression instrument," *J. Appl. Polym. Sci.,* vol. 131, 2014.

[132] M. Mayer, R. Rabindranath, J. Börner, E. Hörner, A. Bentz, J. Salgado*, et al.*, "Ultra-Soft PDMS-Based Magnetoactive Elastomers as Dynamic Cell Culture Substrata," *PLoS ONE,* vol. 8, 2013.

[133] Y. P. Ivanov, A. Alfadhel, M. Alnassar, J. Perez, M. Vázquez, A. Chuvilin*, et al.*, "Tunable Magnetic Nanowires for Biomedical and Harsh Environment Applications," *Scientific Reports,* vol. 6, p. 24189, 2016.

[134] T. Maurer and e. al., "Magnetic nanowires as permanent magnet materials," *Applied Physics Letters,* vol. 91, p. 172501, 2007.

[135] M. Liu, J. Sun, and Q. Chen, "Influences of heating temperature on mechanical properties of polydimethylsiloxane," *Sensors and Actuators A: Physical,* vol. 151, pp. 42-45, 2009

[136] M. Phan and H. Peng, "Giant magnetoimpedance materials: Fundamentals and applications," *Progress in Materials Science,* vol. 53, p. 323, 2008.

[137] L. V. Panina and K. Mohri, "Magneto-impedance in multilayer films," *Sensors Actuators A,* vol. 81, p. 71, 2000.

[138] B. Li, P. Salem, I. Giouroudi, and J. Kosel, "Integration of Thin Film Giant Magneto Impedance Sensor and Surface Acoustic Wave Transponder," *Journal of Applied Physics,* vol. 111, p. 07E514, 2012.

[139] B. Dufay, S. Saez, C. Dolabdjian, A. Yelon, and D. Menard, "Development of a high sensitivity Giant Magneto-Impedance magnetometer: comparison with a commercial Flux-Gate," *IEEE Trans. Magn. ,* vol. 49 pp. 85-88, 2013

[140] M. Malátek and L. Kraus, "Off-diagonal GMI sensor with stress-annealed amorphous ribbon," *Sens. Actuators A: Physical,* vol. 164 pp. 41-45, 2010

[141] M. Vázquez, H. Chiriac, A. Zhukov, L. Panina, and T. Uchiyama, *Phys. Status Solidi Appl. Mater. Sci.,* vol. 208, p. 493, 2011.

[142] F. L. A. Machado and S. M. Rezende, "A theoretical model for the giant magnetoimpedance in ribbons of amorphous soft-ferromagnetic alloys," *J. Appl. Phys.,* vol. 79 pp. 6558-6560, 1996

[143] L. A. Tuan, N. T. Huy, and P. T. Huy, "Giant magnetoimpedance in layered composite micro-wires for high-sensitivity magnetic sensor applications," *J. Phys.: Conf. Ser.,* vol. 187 p. 012044, 2009

[144] A. Chaturvedi, N. Laurita, A. Leary, M. H. Phan, M. E. McHenry, and H. Srikanth, "Giant magnetoimpedance and field sensitivity in amorphous and nanocrystalline (Co1− xFex) 89Zr7B4 (x= 0, 0.025, 0.05, 0.1) ribbons," *Journal of Applied Physics,* vol. 109, p. 07B508, 2011.

[145] K. Mohri, T. Uchiyama, L. P. Shen, C. M. Cai, L. V. Panina, Y. Honkura*, et al.*, "Amorphous wire and CMOS IC based sensitive micromagnetic sensors utilizing magnetoimpedance (MI) and stress-impedance (SI) effects," *IEEE Trans. Magn.,* vol. 38, pp. 3063-3068, 2002.

[146] E. Fernandez, G. V. Kurlyandskaya, A. Garcia-Arribas, and A. V. Svalov, "Nanostructured giant magneto-impedance multilayers deposited onto flexible substrates for low pressure sensing," *Nanoscale Res Lett* vol. 7, p. 230, 2012.

[147] B. Li, M. N. Kavaldzhiev, and J. Kosel, "Flexible magnetoimpedance sensor," *Journal of Magnetism and Magnetic Materials,* vol. 378, pp. 499-505, 2015.

[148] D. d. Cos, A. García-Arribas, and J. M. Barandiarán, "Analysis of magnetoimpedance measurements at high frequency using a microstrip transmission line," *Sensors and Actuators A: Physical* vol. 115, pp. 368-375, 2004.

[149] Y.-L. Park, B. Chen, and R. J. Wood, "Design and fabrication of soft artificial skin using embedded microchannels and liquid conductors," *IEEE Sensors Journal,* vol. 12, pp. 2711–2718, 2012.

[150] T. Someya, Y. Kato, T. Sekitani, S. Iba, Y. Noguchi, Y. Murase*, et al.*, "Conformable, flexible, large-area networks of pressure and thermal sensors with organic transistor active matrixes," *PNAS* vol. 35, pp. 12321-12325, 2005.

[151] W.-H. Yeo, Y.-S. Kim, J. Lee, A. Ameen, L. Shi, M. Li*, et al.*, "Multifunctional epidermal electronics printed directly onto the skin," *Adv. Mater.,* vol. 25, pp. 2773-2778, 2013.

[152] M. Ying, A. P. Bonifas, N. Lu, Y. Su, R. Li, H. Cheng*, et al.*, "Silicon Nanomembranes for Fingertip Electronics," *Nanotechnology* vol. 23 p. 344004, 2012.

[153] J. Kim, M. Lee, H. J. Shim, R. Ghaffari, H. R. C. D. Son, Y. H. Jung*, et al.*, "Stretchable silicon nanoribbon electronics for skin prosthesis," *Nature Comm. ,* vol. 5, p. 5747, 2014.

[154] T. Takahashi, K. Takei, A. G. Gillies, R. S. Fearing, and A. Javey, "Carbon Nanotube Active-Matrix Backplanes for Conformal Electronics and Sensors," *Nano Letters,* vol. 11, pp. 5408–5413, 2011.

[155] E. Kaniusas, H. Pfützner, L. Mehnen, J. Kosel, J. C. Téllez-Blanco, G. Varoneckas*, et al.*, "Method for continuous nondisturbing monitoring of blood pressure by magnetoelastic skin curvature sensor and ECG," *IEEE Sensors Journal,* vol. 6, pp. 819-828, 2006.

[156] N. Chen, C. Tucker, J. Engel, C. Yang, S. Pandya, and C. Liu, "Design and characterization of artificial haircell sensor for flow sensing with ultrahigh velocity and angular sensitivity," *J. Microelectromech. Syst.,* vol. 16, pp. 999–1014, 2007.

[157] S. Traxler, J. Kosel, H. Pfützner, E. Kaniusas, L. Mehnen, and I. Giouroudi, "Contactless flow detection with magnetostrictive bilayers," *Sensors and Actuators A: Physical,* vol. 2, p. 142, 2008.

[158] A. Cubukcu, E. Zernickela, U. Buerklina, and G. Urbana, "A 2D thermal flow sensor with sub-mW power consumption," *Sensors and Actuators A: Physical,* vol. 163, pp. 449-456, 2010.

[159] J. Kuo, L. Yu, and E. Meng, "Micromachined Thermal Flow Sensors—A Review," *Micromachines,* vol. 3, p. 550, 2012.

[160] Y. Cengel and J. Cimbala, *Fluid Mechanics: Fundamentals and Applications*, 2 ed. vol. 1: McGraw-Hill, 2010.

[161] M. Yang, N. Sniadecki, and C. Chen, "Geometric Considerations of Micro- to Nanoscale Elastomeric Post Arrays to Study Cellular Traction Forces," *Adv. Mater.,* vol. 19, p. 3119, 2007

[162] Y. Çengel and J. Cimbala, *Fluid mechanics : fundamentals and applications*, 1 ed. USA: McGraw-Hill, 2006.

[163] B. Li, A. Morsy, and J. Kosel, "Optimization of autonomous magnetic field sensor consisting of giant magnetoimpedance sensor and surface acoustic wave transducer," *IEEE Trans. Mag.,* vol. 11, pp. 4324-4327, 2012.

APPENDICES

LIST OF PUBLICATIONS

Patents:

[1] **A. Alfadhel**, B. Li, J. Kosel: “Magnetic Nanocomposite Sensor”. U.S. Patent Application, Appl. No. PCT/IB2015/058274, Publication No. WO 2016/067197 A1.

[2] Enrique Vilanova Vidal, **A. Alfadhel**, Yurii Ivanov, J. Kosel: “System and Method for Nanowire Fabrication”. U.S. Patent Application, Appl. No. 62056114.

Peer-reviewed journal papers:

[1] **A. Alfadhel**, M. A. Khan, S. Cardoso, D. Leitao, and J. Kosel, “A Magnetoresistive Tactile Sensor for Harsh Environment Applications,” *Sensors,* vol. 16, Issue 650, pp. 1-13, 2016.

[2] **A. Alfadhel**, M. A. Khan, S. Cardoso, and J. Kosel, “Magnetic Tactile Sensor for Braille Reading,” *IEEE Sensors,* 2016.

[3] Y. P. Ivanov*, **A. Alfadhel***, M. Alnassar, J. Perez, M. Vázquez, A. Chuvilin, J. Kosel, “Tunable Magnetic Nanowires for Biomedical and Harsh Environment Applications,” *Scientific Reports*, vol. 6, pp. 24189, 2016. DOI: 10.1038/srep24189. (** Equal contribution*)

[4] M.F Contreras, A. Zaher, J.E. Perez, **A. Alfadhel**, L.A.S. de Oliveira, K.R. Pirota, T. Ravasi, J. Kosel, “Magnetic Nanowires and Hyperthermia: the Influence of Geometry on and Material on Heat Production Efficiency,” *<in preparation>*

[5] O. Yassine, A. Zaher, E. Li, **A. Alfadhel**, J. Perez, M. Kavaldzhiev, M. Contreras, S. Thoroddsen, N. Khashab and J. Kosel, "Highly Efficient PNIPAM-Nanowire Composites for Drug Delivery,” *Scientific Reports*, 2016. *<Accepted>*

[6] O. Yassine, E. Li, **A. Alfadhel**, M. Kavaldzhiev, A. Zaher, S. Thoroddsen and J. Kosel, " Magnetically Triggered Monodispersed Nanocomposite Fabricated by Microfluidic Approach for Drug Delivery," *International Journal of Polymer Science*, vol. 2016, 2016.

[7] **A. Alfadhel**, and J. Kosel, “Magnetic Nanocomposite Cilia Tactile Sensor,” *Advanced Materials*, vol. 27, Issue 47, pp. 7888–7892, December 16, 2015. DOI: 10.1002/adma.201504015

Paper highlighted in:

Nature: Iron skin senses the softest touch, *Nature* 526, 612, (29 October 2015) DOI:10.1038/526612d

New Scientist: https://www.newscientist.com/article/2075303-im-capturing-spider-sense-in-nanowires-to-make-artificial-skin

Kennislink: http://www.kennislink.nl/publicaties/voelen-met-ijzerdraadjes

KAUST Discovery: https://discovery.kaust.edu.sa/en/article/167/sensors-for-a-light-touch

[8] M. Y. Alnassar, **A. Alfadhel**, Yu. P. Ivanov and J. Kosel, “Magnetoelectric Polymer Nanocomposite for Flexible Electronics,” *Journal of Applied Physics,* vol. 117, pp. 17D711, 2015.

[9] **A. Alfadhel**, B. Li, O. Yassine, A. Zaher and J. Kosel, “Magnetic Nanocomposite for Biomimetic Flow Sensing,” *Lab Chip*, vol. 14, pp. 4362, August 2014.

[10] **A. Alfadhel**, A. A. Arevalo Carreno, I. G. Foulds, and J. Kosel, “Three-axis Magnetic Field Induction Sensor Realized on Buckled Cantilever Plate*,” IEEE Transactions on Magnetics,* vol*. 49, pp. 4144, July 2013.*

[11] **A. Alfadhel**, Y. Gianchandani, J. Kosel, “Microfabrication of magnetostrictive beams based on NiFe film doped with B and Mo for integrated sensor systems,” *Journal of Applied Physics*, vol. 111, pp. 07E515, April 2012.

Conference proceedings:

[1] **A. Alfadhel**, M. A. Khan, S. Cardoso, and J. Kosel, “A Single Magnetic Nanocomposite Cilia Force Sensor,” *2015 IEEE Sensors Applications Symposium*, Catania, Italy, 20-22 April, 2016. DOI: 10.1109/SAS.2016.7479828

[2] M. A. Khan, **A. Alfadhel**, M. Bakolka, and J. Kosel, “Fabrication and Characterization of Magnetic Composite Membrane Pressure Sensor,” *2015 IEEE Sensors Applications Symposium*, Catania, Italy, 20-22 April, 2016. DOI: 10.1109/SAS.2016.7479871

[3] **A. Alfadhel**, and J. Kosel, “Biomimetic Magnetic Nanocomposite for Smart Skins,” *IEEE Sensors,* Busan, Korea, 1-4 November 2015.
DOI: 10.1109/ICSENS.2015.7370646

[4] **A. Alfadhel**, and J. Kosel, "Magnetic Micropillar Sensors for Force Sensing," *Sensors Applications Symposium (SAS),* pp. 1 - 4, 2015.
DOI: 10.1109/SAS.2015.7133654 *(Best Paper Award)*

Paper highlighted in:

Saudi Gazette: "KAUST researchers offer 'touch' to the world", 15 April 2015
MIT Technology Review: technologyreview.me/en/biomedicine/making-artificial-skin-that-can-sense-the-touch
Molecular Biology Society: http://molecularbiologynews.org/Saudi-Researcher-Invents-New--Touch--Device
KAUST Main Webpage: http://www.kaust.edu.sa/latest-stories/ahmed-alfadhel-ieee-symposium-award.html

[5] **A. Alfadhel**, B. Li, and J. Kosel, "Magnetic Polymer Nanocomposites for Sensing Applications," *IEEE Sensors,* pp. 2066 - 2069, 2014.
DOI: 10.1109/ICSENS.2014.6985442

Conference presentations:

[1] **A. Alfadhel**, and J. Kosel, "Magnetic Nanocomposite Smart Skin," *34th Annual Microelectronic Engineering Conference at Rochester Institute of Technology*, Rochester, NY-USA, 9-10 May 2016. *<Invited talk>*

[2] **A. Alfadhel**, M. A. Khan, S. Cardoso, and J. Kosel, "A Single Magnetic Nanocomposite Cilia Force Sensor," *2015 IEEE Sensors Applications Symposium*, Catania, Italy, 20-22 April, 2016. *< Oral presentation >*

[3] M. A. Khan, **A. Alfadhel**, M. Bakolka, and J. Kosel, "Fabrication and Characterization of Magnetic Composite Membrane Pressure Sensor," *2015 IEEE Sensors Applications Symposium*, Catania, Italy, 20-22 April, 2016. *< Oral presentation >*

[4] M. A. Khan, **A. Alfadhel**, and J. Kosel, "Magnetic Nanocomposite Cilia Energy Harvester," *2016 joint MMM/ INTERMAG conference*, San Diego, California, USA, 11-15 January, 2016. *<Oral presentation>*

[5] M.F. Contreras, A. Zaher, J.E. Pérez, **A. Alfadhel**, L.A.S. de Oliveira, K.R. Pirota, T. Ravasi, J. Kosel, "Specific Absorption Rate Magnetic Nanowires: How Geometry and Material Affect Heat Production Efficiency", *ASME 2015 4th Global Congress on Nano Engineering for Medicine and Biology*. *<Oral presentation>*

[6] **A. Alfadhel**, and J. Kosel, “Magnetic Nanocomposite Cilia Sensors,” *Materials Research Society (MRS) Fall Meeting,* Boston, USA, 29 November- 4 December 2015. *<Poster>*

[7] **A. Alfadhel**, and J. Kosel, “Biomimetic Magnetic Nanocomposite for Smart Skins,” *IEEE Sensors,* Busan, Korea, 1-4 November 2015. *<Oral presentation>*

[8] **A. Alfadhel** and J. Kosel, “Bioinspired Magnetic Nanocomposite Sensors,” *Energy, Materials and Nanotechnology Conference on (EMN)*, at San Sebastian, Spain, 1-4 September 2015. *<Invited talk>*

[9] **A. Alfadhel**, and J. Kosel, “Bioinspired Nanocomposite Tactile Sensor,” *International Conference on Magnetism (ICM 2015),* Barcelona, Spain, 5-10 July 2015. *<Oral presentation>*

[10] Yu. P. Ivanov, **A. Alfadhel**, M. Y. Alnassar and J. Kosel, “Magnetic Properties of Core-shell Fe-Fe_3O_4 Nanowires,” *IEEE International Magnetics Conference (INTERMAG)*, Beijing, China, 11-15 May 2015. *<Oral presentation>*

[11] **A. Alfadhel**, and J. Kosel, “Magnetic Micropillar Sensors for Force Sensing,” *2015 IEEE Sensors Applications Symposium,* Zadar, Croatia, 12-15 April 2015. *<Oral presentation>*

[12] **A. Alfadhel**, Yu. P. Ivanov, M. Y. Alnassar and J. Kosel, “Magnetic Core-shell Iron-Iron Oxide Nanowires,” *59th Annual Conference on Magnetism and Magnetic Materials (MMM 2014),* Honolulu, Hawaii, USA, 3-7 November 2014. *<Oral presentation>*

[13] **A. Alfadhel**, B. Li, and J. Kosel, “Magnetic Polymer Nanocomposites for Sensing Applications,” *IEEE Sensors,* Valencia, Spain, 2-5 November 2014. *<Poster>*

[14] M. Y. Alnassar, **A. Alfadhel**, Yu. P. Ivanov, and J. Kosel, “Magnetoelectric Polymer Nanocomposite for Flexible Electronics,” *59th Annual Conference on Magnetism and Magnetic Materials (MMM 2014),* Honolulu, Hawaii, USA, 3-7 November 2014. *<Poster>*

[15] **A. Alfadhel** and J. Kosel, “Magnetic Polymer Composites for Smart Sensing Applications,” *Energy, Materials and Nanotechnology Conference on (EMN)*, at Chengdu, China, 22-25 September 2014. *<Invited talk>*

[16] **A. Alfadhel** and J. Kosel, “Magnetic Polymer Micropillars for Smart Sensing Applications,” *IEEE International Magnetics Conference (INTERMAG)*, Dresden, Germany, 4-8 May 2014. *<Oral presentation>*

[17] **A. Alfadhel**, R. Hetaimish, B. Li and J. Kosel, “Bioinspired Hair Flow Sensor Fabricated by the Incorporation of Iron Nanowires into PDMS Micropillars,” *58th Annual Conference on Magnetism and Magnetic Materials (MMM 2013),* Denver, Colorado, USA, 4-8 November 2013. *<Oral presentation>*

[18] O. Yassine , A. Zaher, E. Li, **A. Alfadhel**, S. Thoroddsen and J. Kosel, “Magnetically Controlled Droplets of Thermosensitive Microgel as Advanced Agent Carriers,” *58th Annual Conference on Magnetism and Magnetic Materials (MMM 2013),* Denver, Colorado, USA, 4-8 November 2013. *<Oral presentation>*

[19] **A. Alfadhel**, A. Zaher, O. Yassine and J. Kosel, “Iron Nanowires Incorporated into A PDMS Membrane,” *Joint European Magnetic Symposia (JEMS 2013)*, Rhodes, Greece, 25-30 August 2013. *<Oral presentation>*

[20] **A. Alfadhel**, A. Zaher, O. Yassine, R. Sougrat and J. Kosel, “Incorporation of Iron Nanowires into A PDMS Membrane,” *Advances in Microfluidics and Nanofluidics conference*, University of Notre Dame, Indiana, USA, 24-26 May 2013. *<Poster>*

[21] O. Yassine , A. Zaher, E. Li, **A. Alfadhel**, S. Thoroddsen and J. Kosel ,“Magnetically Controlled Droplets of Thermosensitive Microgel as Advanced Agent Carriers,” *Advances in Microfluidics and Nanofluidics conference*, University of Notre Dame, Indiana, USA, 24-26 May 2013. *<Oral presentation>*

[22] **A. Alfadhel**, A. A. Arevalo Carreno, I. G. Foulds, and J. Kosel, “Three-axis Magnetic Field Induction Sensor Realized on Buckled Cantilever Plate*,” 12th joint MMM/ INTERMAG conference*, Chicago, Illinois, USA, 14-18 January, 2013. *<Oral presentation>*

[23] **A. Alfadhel**, B. Li, J. Kosel, “A tri-layer Stress Impedance Sensor Using Amorphous Magnetostrictive Thin Film,” *19th International Conference on Magnetism (ICM 2012),* Busan, Korea, 8-13 July, 2012. *<Poster>*

[24] **A. Alfadhel**, C. Liang, Y. Gianchandani, J. Kosel, “Microfabrication of Magnetostrictive Sensor Beams Based on NiFe Film Doped with B and Mo for Biomedical Applications,” *56th Annual Conference on Magnetism and Magnetic Materials (MMM 2011),* Scottsdale, AZ, USA, Oct. 30 - Nov. 3, 2011. *<Poster>*

[25] J. Kosel, C. Liang, **A. Alfadhel**, "Development of Magnetostrictive Microsensors for Microfluidic Systems", *5th International Workshop on Amorphous and Nanostructured Materials*, Iasi, Romania, 5-7 September, 2011. *<Invited talk>*

KAUST Events:

[1] **A. Alfadhel** and M. Ghoneim, “Tips on Scientific Writing,” *Graduate Affairs Special Event*, 13 October, 2015.

[2] **A. Alfadhel**, J. Kosel, “Magnetic Polymer Nanocomposites for Sensing Applications,” *KAUST-NSF Conference on Electronic Materials, Devices and Systems for Sustainable Future,* February 2015. *<Poster>*

[3] **A. Alfadhel**, J. Kosel, “Turning to Nature for Inspiration: Towards High Resolution and Low Power Flow Sensor,” *Electrical engineering graduate seminar*, April 2014. *<Presentation>*

[4] **A. Alfadhel**, B. Li, J. Kosel, “Turning to Nature for Inspiration: Towards High Resolution and Low Power Flow Sensor,” *Global Collaborative Research Symposium*, March 2014. *<Poster>*

[5] **A. Alfadhel**, B. Li, J. Kosel, “Magnetic Polymer Micropillars Realized on Giant Magneto-impedance Element for Biomimetic Flow Sensing,” *KAUST-NSF Conference on Electronic Materials, Devices and Systems for Sustainable Future,* February 2014. *<Poster>*

[6] **A. Alfadhel**, A. A. Arevalo Carreno, I. G. Foulds, and J. Kosel, “Three-axis Magnetic Field Induction Sensor Realized on Buckled Cantilever Plate*,”* International Advisory Council meeting (IAC), April 2013. *<Poster>*

[7] **A. Alfadhel**, A. A. Arevalo Carreno, I. G. Foulds, and J. Kosel, “Three-axis Magnetic Field Induction Sensor Realized on Buckled Cantilever Plate*,”* WEP poster competition, January 2013. *<Poster>*

[8] **A. Alfadhel**, Y. Gianchandani, J. Kosel, “Microfabrication of Magnetostrictive Beams for Integrated Sensor Systems,” *EE Days*, February 2012. *<Poster>*

[9] **A. Alfadhel**, J. Kosel, "Design and Microfabrication of MEMS Device for Biomedical Applications," *KAUST 1st Graduate Research Symposium*, January 2011. *<Poster>*